HIGH RESOLUTION ACETIC ACID SURVEY AND WATER VAPOR RADIOMETER

BY

YU-SHAO SHIAO

B.A., National Chiao Tung University, 1996
M.S., National Taiwan University, 2001

DISSERTATION

Submitted in partial fulfillment of the requirements
for the degree of Doctor of Philosophy in Astronomy
in the Graduate College of the
University of Illinois at Urbana-Champaign, 2008

Urbana, Illinois

Doctoral Committee:

Assistant Professor Leslie Looney, Chair
Professor Lewis Snyder
Assistant Professor Benjamin McCall
Doctor Douglas Friedel
Associate Professor Edmund Sutton

Abstract

Planets, comets, stars, galaxies and the interstellar medium (ISM) emit complex but distinct molecular spectra. These spectra reveal the chemical composition and physical conditions in the objects. For example, many biologically important molecules, such as acetic acid, formic acid, vinyl cyanide and ethyl cyanide, have been detected in hot molecular cores in the ISM. A diversity of molecules creates complicated and yet interesting astrochemistry in hot cores. However, the formation mechanisms of large molecules are still unclear. Hence large molecule observations are essential to understand hot core chemistry. Among these molecules, acetic acid is one of the most important large species in hot cores. It is a possible precursor of glycine, the simplest amino acid. It only has been detected in high-mass hot cores without oxygen/nitrogen chemical differentiation, which is key to hot core chemical models. Using the Combined Array for Research in Millimeter-wave Astronomy (CARMA), we have conducted an acetic acid survey in hot cores. In our survey, we have discovered a new acetic acid hot core, G19.61-0.23, which shows no chemical differentiation as the other acetic acid hot cores. Therefore, we suggest that both large oxygen and nitrogen-bearing species play important roles in acetic acid formation.

Ground-based interferometric observations are severely affected by atmospheric conditions. Phase correction is a technique to obtain high quality data and achieve great scientific goals. For our acetic acid survey, a better phase correction technique can not only detect weaker transitions of large molecules, but also increase the map resolution of hot cores. Water vapor radiometers (WVRs) are designed to improve the technique by observing tropospheric water vapor along the lines of sight of interferometers. We have numerically demonstrated the importance of phase correction for interferometric observations and examined the water vapor phase correction technique. Furthermore, we have built two WVR prototypes with new calibration, thermal regulation and backend systems. The WVR prototypes had been tested in a laboratory, on a roof and at the CARMA site to verify their performance. We conclude the WVR thermal stability and dynamic range are critical while the enormous and rapid fluctuations of the sky background emission overwhelm the WVR dynamic range and degrade the WVR sensitivity.

Table of Contents

List of Tables

List of Figures

Chapter 1

Background

Many molecules in the interstellar medium (ISM) are detected and identified by their rotational transition spectra. Spectral observations are essential astronomical measurements because they can reveal the physical conditions of interstellar molecules and their surroundings. To investigate the ISM by observing molecules, it is important to understand rotational spectroscopy.

Simple molecules and atoms can generate complex and large molecules in the ISM via chemical reactions. Especially, hot molecular cores, possibly at the early stage of star formation with high temperatures (T $>$ 100 K) and densities (n $>$ 10^6 cm^{-3}), are the most molecule abundant regions. Hot temperatures and abundant atoms in star forming regions forge environments in which many molecules can form and survive. A huge inventory of molecules with various hot core physical conditions creates complicated and interesting chemistry, which is still not fully understood to astronomers and chemists. Therefore, large molecule observations, such as acetic acid surveys, are critical for hot core researchers to establish hot core chemical models.

1.1 Introduction

When a molecule suddenly changes from one energy level to another, it may absorb or emit photons as electromagnetic waves. Such molecular energy changes are called molecular transitions. Molecular transitions mainly include rotational, vibrational and electronic transitions corresponding to the types of motions. Moreover, molecules can change their two or more types of motion energies simultaneously, for example, vibration and rotation energies. Then they produce vibration-rotation transitions. Approximately, vibrational and electronic transitions are in the infrared and optical while pure rotational transitions are in the radio frequency region.

The radio frequency region happens to be one of the observable windows from the ground. The atmosphere opacity is strongly frequency dependent due to the chemical composition of the atmosphere. Only several optically thin windows are available to ground-based telescopes (Rohlfs & Wilson 2006). The radio

window is located at 10 MHz to 300 GHz, from centimeter to submillimeter wavelengths. Many rotational transitions of interstellar molecules are detected through this window. Therefore, radio rotational transitions play a critical role in molecular detection in space.

The first interstellar molecules were discovered with optical absorption lines (Swings & Rosenfeld 1937; McKellar 1940, 1941; Adams 1941). These detections triggered searches for interstellar molecules. Two decades later, Weinreb et al. (1963) detected OH absorption lines for the first time at radio frequencies. It was long believed that diatomics were the only molecules that could survive in the ISM (Snyder 2006); however, polyatomics indeed exist as well. The first detected polyatomics are NH_3 (Cheung et al. 1968), H_2O (Cheung et al. 1969) and H_2CO (Snyder et al. 1969) using rotational transitions. H_2CO is the first organic molecule, which suggests organic chemistry in the ISM. Snyder et al. (1976) also detected the interstellar molecular ion, HCO^+, with the first ion rotational spectrum. To date, 147 molecules have been discovered in space (Lovas & Snyder 2008) and most of them are identified with rotational transitions.

With the observations of interstellar molecules, researchers can study the chemical and physical conditions of molecular clouds. Molecular clouds in the ISM can be dense or diffuse, and hot or cold. A diversity of interstellar clouds driven by various astronomical events provides different environments for molecules to be formed and destroyed. By detecting interstellar molecules, we can explore molecular clouds to investigate their dynamics and evolutions. As a result, molecules are powerful probes for astronomical study. Abundant diatomics, such as ^{12}CO and ^{13}CO, have been used to deeply determine the structures of astronomical objects while large molecules are observed to better understand hot core chemistry.

Numerous molecules were detected in hot molecular cores, like Sgr B2 (e.g. Friedel et al. 2004) and Orion KL (e.g. Friedel et al. 2005). Moreover, many large molecules are organic molecules, such as acetic acid, formic acid, methyl formate and ethyl cyanide. The detections raise questions about their formations and relationships to the surroundings. Their existence may lead to the formation of more complex and biological species, like glycine, which is the simplest amino acid.

While some hot cores contain oxygen and nitrogen-rich chemistry, others only have oxygen-rich chemistry. This O/N chemical differentiation has been studied for many years (Blake et al. 1987; Rodgers & Charnley 2001). Many chemical models suggest that the O/N chemical differentiation reflects the ages of hot cores. However, without direct measurements of the hot core ages, the uncertainty is still high. Before we can fully understand hot core chemical evolution, we need more molecular observations to verify hot core chemical models.

In the following sections, we review rotational spectroscopy and hot core chemistry. Most of this review follows Kroto (1992), Sakurai & Tuan (1994), Widom (2002) and Herbst (1999).

1.2 Separation of Rotational Spectroscopy

Purely rotational energy levels of molecules are generally separated from vibrational and electronic energy levels (Kroto 1992). Purely rotational transition energies are much less than the others. While rotational transitions are at radio wavelengths, vibrational and electronic transitions are mainly at infrared and optical wavelengths.

The electrostatic forces dominate the motions of electrons and nuclei in a molecule. Electrons trapped in the central force field of nuclei are approximately simple harmonic oscillators with energy $E_e = \hbar\omega_e$, where ω_e is the electronic oscillating frequency. The vibrational energy of diatomic nuclei can be also considered as harmonic oscillators as $E_v = \hbar\omega_v$, where ω_v is the nuclear vibration frequency. The harmonic angular velocity is $\omega = \sqrt{k/m}$, where k is the force constant and m is the mass. The force constants for electrons and atoms are approximately the same since they have similar electrostatic force strengths. Comparing with these two energies, we obtain

$$\frac{E_v}{E_e} \sim \frac{\omega_n}{\omega_e} \sim (\frac{m_e}{m_n})^{1/2} = \kappa^2, \tag{1.1}$$

where m_n and m_e are the nuclear and electronic masses, and κ^4 is the mass ratio of an electron to a nucleus, $\kappa \sim 0.1$. The rotational energy of atoms $E_r = \hbar^2/2m_n r_{nn}^2 \sim 10^{-23}$ erg and E_v is $\hbar\omega_n \sim 10^{-21}$ erg, where r_{nn} is the distance from one nucleus to the other. Thus, $E_r \sim \kappa^2 E_v$. While the rotational energy E_r is 100 times smaller than the vibrational energy E_v, the vibrational energy E_v is 100 times smaller than the electronic energy E_e. In the ground states of vibrational and electronic energy, the rotational transitions can be approximately separated from other motion transitions.

1.3 Radiative Process and Rotating Molecules

To produce rotational transitions, a rotating molecule needs an electric dipole moment to emit or absorb photons. The electric dipole moment is critical in such a rotational radiative process. Here we demonstrate the relationship between the electric dipole moment and the transition rate, which is directly related to spectral line intensity (Kroto 1992).

First, we review the definition of the electric dipole moment. The potential energy of a system in an electric field E_i is written as

$$U = U^0 + (\frac{\partial U}{\partial E_i})^0 E_i + \frac{1}{2}(\frac{\partial^2 U}{\partial E_i \partial E_j})^0 E_i E_j + \cdots \tag{1.2}$$

where i and j are used for the summation convention and then we take the derivative of U as

$$dU = -\mu dE_i, \tag{1.3}$$

and

$$\mu = \mu^0 + \alpha_{ij}^0 E_j + O(E_i E_j \ldots), \tag{1.4}$$

where $O(E_i E_j \ldots)$ stands for the high order terms, μ is the electric dipole moment, μ^0 is the permanent dipole moment, and $\alpha_{ij}^0 = -(\partial^2 U/\partial E_i \partial E_j)^0$ is the electric susceptibility. The electric dipole moment μ consists of μ^0 and the higher order terms.

To derive the transition rate, the radiative process of a rotating molecule can be considered as a time-dependent potential system with the Hamiltonian

$$H = H_0 + V, \tag{1.5}$$

where H_0 is the time-independent Hamiltonian, and V is time-dependent potential. Thus, the Schrödinger equation is

$$i\hbar \frac{\partial \Psi}{\partial t} = (H_0 + V)\Psi, \tag{1.6}$$

where Ψ is the eigenfunction of the system, which can be written as

$$\Psi = \sum_m a_m(t)\psi_m, \tag{1.7}$$

where $\psi_m = |m\rangle e^{-(i/\hbar)E_m t} = |m, t\rangle$ is the eigenfunction of H_0, and $a_m(t)$ is the time dependent coefficient of ψ_m. We can plug Equation 1.7 into Equation 1.6 and get

$$i\hbar \sum_m \dot{a}_m(t)|m, t\rangle = V \sum_m a_m(t)|m, t\rangle. \tag{1.8}$$

Then, we multiply it by $\langle n|$ on both sides to obtain

$$i\hbar \sum_m \dot{a}_m(t)\langle n|m, t\rangle = \langle n|V \sum_m a_m(t)|m, t\rangle. \tag{1.9}$$

However $\langle n|m\rangle = \delta_{nm}$, so

$$i\hbar \dot{a}_n(t)e^{-(i/\hbar)E_n t} = V_{nm} \sum_m a_m(t)e^{-(i/\hbar)E_m t}, \tag{1.10}$$

and then

$$i\hbar\dot{a}_n(t) = V_{nm}\sum_m a_m(t)e^{-(i/\hbar)(E_m-E_n)t}, \tag{1.11}$$

where $V_{nm} = \langle n|V|m\rangle$. If we only consider the permanent dipole moment, μ^0, from Equation 1.4,

$$V^0_{nm} = -\frac{1}{2}E^0_i\mu^0_i. \tag{1.12}$$

Equation 1.11 is a set of coupling differential equations, which can be solved analytically with initial conditions. If we only consider emission from state m to n in a two state system, the initial conditions are simply that $a_m(0) = 1$ and $a_n(0) = 0$. $a_n(t)$ can be easily obtained by integrating $\dot{a}_n(t')$ from $t' = 0$ to $t' = t$. So we obtain

$$|a_n(t)|^2 = a^\dagger_n(t)a_n(t) = \hbar^2|V^0_{nm}|^2 t\delta(E_m - E_n), \tag{1.13}$$

where $t\delta(E_m - E_n)$ is the integration of $e^{-(i/\hbar)(E_m-E_n)t}$. The detailed calculation can be found in Sakurai & Tuan (1994, p. 316).

The absorption rate R_{mn} is defined as

$$R_{mn} = \frac{d}{dt}|a_n(t)|^2 = B_{mn}\rho, \tag{1.14}$$

where B_{mn} is the Einstein B coefficient of the stimulated absorption from state n to m, and ρ is energy density, which is $1/4\pi\vec{E}^2$. Therefore, combining Equation 1.12, 1.14 and 1.13, we get

$$B_{mn} = \frac{2\pi}{3\hbar^2}|\langle n|\mu|m\rangle|^2, \tag{1.15}$$

or in short as

$$B_{mn} = \frac{2\pi}{3\hbar^2}|\langle\mu\rangle|^2. \tag{1.16}$$

The Einstein B coefficient of the stimulated emission can be obtained by

$$\frac{B_{mn}}{B_{nm}} = \frac{g_n}{g_m}, \tag{1.17}$$

where g_m and g_n are the degeneracy weighting. Then the Einstein A coefficient A_{nm} of spontaneous emission can be obtained by

$$\frac{A_{nm}}{B_{nm}} = \frac{2h\nu^2}{c^2}, \tag{1.18}$$

where ν is the line frequency and c is the speed of light, so that

$$A_{nm} = \frac{64\pi^4\nu^3}{3hc^3}\frac{g_m\langle\mu\rangle^2}{g_n}. \tag{1.19}$$

In the case of diatomics, the Einstein A coefficient is approximately

$$A_{nm} = \frac{64\pi^4\nu^3}{3hc^3}\frac{J\mu_0^2}{2J+1}. \tag{1.20}$$

From Equation 1.16, we know the importance of the electric dipole moment to A_{nm} in the radiative process. Without the electric dipole moment, the potential energy can not effectively be coupled to rotating molecules to change their rotational energies. However, molecules lacking permanent electric dipole moments may still be detectable with the high order terms of the electric dipole moments.

1.4 Energy of Rotating Molecules

Rotational transitions can be caused by the sudden interactions between molecular rotational motions and photons. Photons can be emitted or absorbed as electromagnetic waves by the change of molecular rotational energy. The emitted or absorbed photons in these processes are detected as spectra. The understanding of the rotational transitions can be aided by quantum mechanics with a semi-classical approach (Sakurai & Tuan 1994).

The semi-classical approach treats such quantum mechanics problems as quantized energy levels in a classical mechanics picture, or Newtonian viewpoint. The dynamics of molecular rotation are described by the classical Hamiltonian and transferred to a quantum mechanical Hamiltonian by replacing angular moment operators. Such an approach provides a convenient way to illustrate and calculate the energy levels of rotating molecules (Kroto 1992).

Given a rigid molecule, the kinetic energy of rotational motion, T_r can be written as

$$T_r = \frac{1}{2}I_{ij}\omega_i\omega_j, \tag{1.21}$$

where i and j are used for the summation convention, ω_i and ω_j are angular velocities, and I_{ij} is the moment of inertia tensor. The angular momentum is

$$J_i = \frac{\partial T_r}{\partial \omega_i} = I_{ij}\omega_j. \tag{1.22}$$

Therefore, the Hamiltonian can be written as

$$H_r = \frac{1}{2} I_{ij}^{-1} J_i J_j. \tag{1.23}$$

The three diagonal elements of I are the principal moments of inertia, which is denoted as I_A, I_B and I_C. If I can be diagonalized, the kinetic energy of rotation

$$T_r = \frac{1}{2}(I_A \omega_A^2 + I_B \omega_B^2 + I_C \omega_C^2) \tag{1.24}$$

and then the Hamiltonian becomes

$$H_r = A J_A^2 + B J_B^2 + C J_C^2, \tag{1.25}$$

where A, B and C are rotational constants, $J_A = \partial T_r / \partial \omega_A$, $J_B = \partial T_r / \partial \omega_B$ and $J_C = \partial T_r / \partial \omega_C$, and $A = 1/2I_A$, $B = 1/2I_B$ and $C = 1/2I_C$. Now we may quantize the Hamiltonian to a quantum mechanical form. The quantum mechanical Hamiltonian of rotating molecules depends on the symmetry of molecules.

1.4.1 Classification of Rotating Molecules

While electric dipole moments play a critical role in spectral line intensity, the principal moments of inertia of molecules decide spectral line frequency. It is convenient to classify rotating molecules based on their principal moments of inertia as spherical tops, linear molecules, symmetric tops and asymmetric tops (Kroto 1992).

Spherical Tops

Spherical tops are the simplest molecular rotors. Three principal moments of inertia are exactly equal, $I_C = I_B = I_A$. The quantum mechanical Hamiltonian is

$$H_r = B\mathbf{J}^2, \tag{1.26}$$

where $\mathbf{J}$ is the angular momentum operator and $B = \hbar^2 / I_B = A = C$ is the rotational constant. The energies of rotational levels are

$$E(J) = BJ(J+1) \tag{1.27}$$

with $(2J+1)^2$ fold degeneracy, where $J = 0, 1, 2, 3 \ldots$ is the total angular moment quantum number. The first $2J+1$ fold degeneracy occurs in $K = -J, -J+1, \ldots, 0, 1, \ldots, J-1, J$ corresponding to the orientation

with the figure axis of the molecule. The figure axis is the axis of molecular symmetry. The second $2J+1$ fold degeneracy occurs in M to the orientation in free space. The degeneracy in M cannot be detected in free space without a magnetic field so we may ignore this degeneracy. K is a quantum number as the projection of $\mathbf{J}$ on the figure axis in a molecule-fixed frame while M is a quantum number as the projection of $\mathbf{J}$ on the z-axis in a space or laboratory frame. Nevertheless, J, K and M generate complete basis states $|J\ K\ M\rangle$ for the quantized H_r matrix.

A rigid spherical molecule cannot have rotational transitions due to its lack of a permanent dipole moment. If a spherical molecule is semi-rigid, when rotating, it may have higher order term asymmetry induced by centrifugal distortion to form a temporary non-zero electric dipole moment and have rotational spectra.

Linear Molecules

Linear molecules have two identical principal moments of inertia, which are much larger than the third one, $I_C = I_B \gg I_A$. The Hamiltonian is

$$H_r = B(J_B^2 + J_C^2) = B\mathbf{J}^2, \tag{1.28}$$

where the rotational constants B is equal to C, and A is negligible. The energies of the rotational levels are

$$E(J) = BJ(J+1) \tag{1.29}$$

with no degeneracy in K as $K = 0$. When considering the influence of centrifugal distortion, $E(J)$ becomes

$$E(J) = BJ(J+1) - DJ^2(J+1)^2, \tag{1.30}$$

where D is the centrifugal distortion constant. The selection rules of rotational transitions for linear molecules are $\Delta J = \pm 1$, and the transition energy is

$$\nu = E(J+1) - E(J) = 2B(J+1) - 4D(J+1)^3. \tag{1.31}$$

If the second term is negligible, it is of interest that the observed frequency are simply proportional to $J+1$. CO is a well-known linear molecule, which is the second most abundant molecule in the ISM. The most abundant molecule, H_2, is a linear molecule. It lacks a permanent dipole moment; however, it can be detected through its quadrupole moment transitions with the selection rules, $\Delta J = \pm 2$, which are much weaker (Shull & Beckwith 1982).

Symmetric Tops

Symmetric tops $I_C = I_B \neq I_A$, unlike linear molecules, have considerable I_A. If $I_C = I_B > I_A$, the molecule is a prolate symmetric top, like a football; If $I_C > I_B = I_A$, it is an oblate symmetric top, like a pancake. I_C is always chosen as the largest principal moment of inertia when we set the figure axis for the molecule. The Hamiltonian is

$$H_r = AJ_A^2 + B(J_B^2 + J_C^2), \tag{1.32}$$

for prolate tops or

$$H_r = CJ_C^2 + B(J_B^2 + J_A^2). \tag{1.33}$$

for oblate tops. The energies of the rotational levels are

$$E(J, K) = BJ(J + 1) + (A - B)K^2, \tag{1.34}$$

for prolate tops or

$$E(J, K) = BJ(J + 1) + (C - B)K^2, \tag{1.35}$$

for oblate tops. The energies have no degeneracy in K when $K = 0$ but two fold degeneracy when $K \neq 0$. The selection rules are $\Delta J = 0, \pm 1$ and $\Delta K = 0$. With centrifugal distortion, a series of K values give a distinct transition pattern (Townes & Schawlow 1955). NH_3 (ammonia) is an example of a symmetric top in the ISM.

Asymmetric Tops

Asymmetric tops have three different rotational constants, $I_C \neq I_B \neq I_A$. A single K on the figure axis is no longer sufficient to properly describe the degeneracy. **J** can project on the two axes with different values, K_a and K_c, which are pseudo-quantum numbers. The electric dipole moments on the three axes are comparable to each other. Thus, transitions can be a-type, b-type and c-type groups. The selection rules are in terms of K_a and K_c.

Most molecules are asymmetric tops. Analytically solving the H_r for asymmetric tops is difficult in most cases. However, some asymmetric tops can be treated as near-symmetric tops. For a very low J values, one can use the Wang basis functions (see Kroto 1992) to transform the matrix of H_r into an analytic form and approximately solve the equations.

1.4.2 Internal Rotors

As the centrifugal force can stretch linear molecules, many large molecules, like acetone (CH_3COCH_3), methanol (CH_3OH), acetic acid (CH_3COOH) and methyl formate ($HCOOCH_3$) are flexible. They have one or two internal rotors, CH_3. Internal rotors can be rigid or free depending on the energy barriers. The barriers of CH_3 in these molecules are considerably low, which can have torsion-rotation transitions splitting into A and E symmetry states.

The internal rotation motion, torsion, can be described as an extra term in the Hamiltonian. The new Hamiltonian includes rotational and torsional terms. It can be approximately solved by two main approaches, Principal Axis Method (PAM) and Internal Axis Method (IAM) (Lin & Swalen 1959). The difference between the two methods is the reference configuration of molecules. The choice is based on which resulting Hamiltonian is more convenient to be solved. In some cases, one method is more suitable than the other.

1.4.3 Rotational Partition Function

A rotational partition function describes the distribution of rotational energy levels of a rotating molecule in term of the rotational temperature T_r. If the quantum number J is sufficient for the complete set of eigenstates, the partition function is

$$Q_r(T_r) = e^{-<J|H_r|J>/kT_r} = \sum_J g_J e^{-E_r(J)/kT_r}, \tag{1.36}$$

which in the case of a linear molecule is

$$Q_r(T_r) = \sum_J (2J+1) e^{-BJ(J+1)/kT_r}, \tag{1.37}$$

where k is Boltzmann's constant, g_J is the weighting, E_r is rotational energy levels, and B is the rotational constant. If $T_r \gg B/k$, where B/k is the characteristic rotational temperature, the rotational partition function becomes

$$Q_r(T_r) \sim \frac{kT_r}{B\sigma}, \tag{1.38}$$

where σ is the symmetry number. $\sigma = 1$, when the molecule is heteronuclear diatomic; $\sigma = 2$, when it is mononuclear diatomic (Widom 2002). For asymmetric tops, the partition function in a high temperature limit is

$$Q_r(T_r) \sim \frac{\sqrt{\pi}}{\sigma} \frac{(kT_r)^{3/2}}{\sqrt{ABC}}, \tag{1.39}$$

where A and C are the rotational constants.

If a system is involved with chemical reactions, the partition function should include chemical potential and become a grand canonical partition function. However, rotational energy is generally not high enough to overcome chemical barriers. Therefore, we just need to deal with the canonical rotation partition function.

1.5 Hot Core Chemistry

When molecular clouds collapse as hot molecular cores to form protostars, the density and temperature gradually increase. Chemical reactions in the hot molecular cores can actively occur. As a result, such hot molecular cores contain the most molecular species in the ISM (Lovas & Snyder 2008). With the observations of molecular spectra and maps, we learn about the physical and chemical conditions of hot cores. Hot core researchers constantly improve their chemical models including chemical reaction networks and physical parameters in terms of time and space. The chemical models can be time dependent and describe the chemical evolution of hot cores. However, to date, it still remains a challenge to comprehensively develop accurate models for hot core chemistry (Snyder 2006). The number of molecular species is enormous and the physical conditions of hot cores vary.

1.5.1 Chemical Reactions

Chemical reactions describe how atoms and molecules can generate other species. They are the building blocks of chemical models to simulate steady state chemical conditions or time dependent chemical evolution (see Herbst 1999, p.355). For example, if a chemical reaction produces C and D from A and B as

$$A + B \rightarrow C + D, \tag{1.40}$$

A and B are precursors and C and D are products. The reaction rate can be written as

$$d[A]/dt = d[B]/dt = -k_1[A][B], \tag{1.41}$$

where $[A]$ and $[B]$ are the concentrations of A and B, and k_1 is the rate coefficient (see Herbst 1999, p.343). The reaction rate from A and B to C and D depends on the concentrations of A, B and k_1. If the reaction can occur in the opposite direction from C and D to A and B simultaneously, the reaction rate depends on A, B, C, D, the forward reaction coefficient and reverse reaction coefficient. The rate coefficient depends on the barrier of the chemical reaction E_b, temperature T and a slightly temperature-dependent parameter

$\alpha(T)$ as

$$k_1 = \alpha(T)e^{-E_b/kT}, \tag{1.42}$$

where k is the Boltzmann constant (Herbst 1999). A, B, C and D can be photons, electrons, atoms or molecules in gas phase or dissolved in solid or liquid. The processes of molecules forming mantles on and evaporating from grain surfaces can be described by a reaction equation similar to chemical reactions. For example, the desorption rate of molecules to grain surfaces is similar to the rate coefficient,

$$k_s = \nu e^{-E_s/kT}, \tag{1.43}$$

where ν is a vibrational frequency of the molecules and E_s is the desorption energy.

As new species are discovered in hot cores, more and more chemical reactions are included in hot core chemical models. Moreover, to match the models with observations, the reaction rates of chemical reactions are constantly updated by theoretical calculations and laboratory experiments.

1.5.2 Chemical Models

With a diversity of molecules and chemical reactions, hot cores are like ecosystems. The pathways of chemical reactions to large molecules are like food chains. The abundances of large molecules significantly depend on the species and abundances of simple molecules. Thus, large molecules may be more sensitive to hot core physical and chemical conditions. Without proper precursors, temperature and even dust, some large molecules can not be formed efficiently and survive. In an ocean, we see fish with fins; on land, we see animals with feet. Various environments may create the chemical differentiations of molecular populations.

Gas phase and grain surface chemistry are both suggested to be critical in large molecule formation (Hasegawa, Herbst, & Leung 1992; Garrod & Herbst 2006; Garrod, Weaver, & Herbst 2008). The abundance enhancement of large molecules by such grain surface reactions is confirmed by the large molecule observations (e.g. Miao & Snyder 1997; Mehringer et al. 1997). Gas phase reactions have been somewhat understood while grain surface reactions mostly remain unclear. Gas phase molecules can be attached to the surfaces of dust grains to form icy mantles, where some large molecules can be efficiently formed. Molecular precursors need to move around in the mantles to react with other atoms or molecules. The time scales of the reactions can be estimated only approximately (Hasegawa, Herbst, & Leung 1992).

O/N chemical differentiation in hot cores, such as Orion KL and W3(OH) have been studied by Blake et al. (1995) and Rodgers & Charnley (2001). Large N-bearing species are not as abundant as large O-bearing species in these regions. Many suggestions have been proposed. One is that O/N chemical differentiation is

a phase of hot core chemical evolution (Blake et al. 1995; Rodgers & Charnley 2001). Most large N-bearing species will be produced at the later stage of hot cores. Another is that methanol (CH_3OH) and ammonia (NH_3) are suggested to be key precursors on grain mantles when hot core temperature increases (Rodgers & Charnley 2001). As a hot core evolves, the timing of ammonia injecting from grain mantles affects O-rich chemistry. However, since the hot core physical conditions vary and these chemical models are sensitive to physical parameters, confirming chemical models may only depend on extensive hot core observations.

1.5.3 Chemical Evolution in Star Forming Regions

Hot cores are the early stage of high-mass star forming regions. Star forming regions that generate heat and shocks into their surroundings provide sufficient energy for chemical reactions. To date, while low-mass star formation is somewhat understood (e.g. Shu 1977; Li & Shu 1996), high-mass star formation still remains uncertain. As stars form, the circumstellar chemical conditions respond to the physical evolution. Hot core chemistry can reflect the chemical evolution of high-mass star formation, which may lead to some clues about the physical evolution of high-mass stars.

Basically at the earliest stage of low-temperature molecular clouds, prior to star formation, low density simple molecules in the gas phase dominate the clouds. When the cold clouds are collapsing, their densities and temperature increase as molecules are deposited on the surface of dust grains as icy mantles. Dust grains provide warm reaction beds when ultraviolet photons hit the surfaces. Many large molecules are formed and some original gas phase molecules may deplete in the vicinity of dust regions at this stage. Once stars are born as protostars, more radiation overwhelms the surrounding dust and evaporates some molecules back into the gas phase (e.g. Garrod & Herbst 2006). These regions may reach 100 K temperature and 10^6 cm^{-3} density, and they are called hot molecular cores (HMCs) or hot cores. When the star forming regions further evolve, chemical compounds are gradually diffused and destroyed by solar winds and ultraviolet photons. Therefore, molecule observations are important to understand star formation.

Molecular line detection is one of the best ways to probe these star forming regions. Strong but not saturated spectral lines can present the dynamics of the clouds while strong and saturated spectral lines can show the cloud structures. Large molecule observations can reveal chemical composition and perhaps hot core ages by determining chemical differentiation.

1.6 Summary

Rotational transitions of molecules are typically in the radio frequency region, which is observable through the atmosphere. Thus, interstellar molecules are mostly discovered and detected with their rotational transitions. Rotational transitions not only provide distinct fingerprints to identify molecular species but also reveal the physical conditions of molecules, which are essential to investigate the ISM, especially hot cores in this thesis.

The electric dipole moment plays a critical role in rotational spectroscopy. It directly affects the Einstein A coefficient of spontaneous emission, which determines the transition rate and spectral line intensity. The rotational Hamiltonian of a molecule decides the transition frequency, depending on the principal angular moments of inertia. Rotating molecules are classified as spherical tops, linear molecules, symmetric tops or asymmetric tops. Each group has a particular spectral pattern. Moreover, many large molecules have internal rotors that create torsion-rotation transitions, which can be use to identify molecules.

Hot molecular cores are molecule-rich regions in the ISM. Many large molecules, including biologically important molecules, have been detected in hot cores. Gas phase and grain surface chemical reactions have been suggested as equally important to large molecule formation. Chemists have constantly improved the hot core chemical models to match observations. However, hot core molecules are so abundant and diverse that they form a chemical "ecosystem" extensively with myriad chemical reactions. It is difficult to clearly show pathways and precursors for certain large molecules. O/N chemical differentiation has been observed and studied. It is suggested to be strongly related to the hot core ages. However, without confirmation from other measurements, the uncertainty is still high. To date, unlocking the secret of large molecule formation still relies on a great amount of observations to better constrain the hot core chemical models.

Chapter 2

First Acetic Acid Survey With CARMA In Hot Molecular Cores

We report the first acetic acid (CH_3COOH) survey conducted with the Combined Array for Research in Millimeter-wave Astronomy (CARMA) at 3 mm wavelengths towards G19.61-0.23, IRAS 16293-2422 and NGC 1333 IRAS 4A. In addition to CH_3COOH, we also have observed methyl formate ($HCOOCH_3$) and ethyl cyanide (CH_3CH_2CN) to determine oxygen/nitrogen chemical differentiation. In this work, we have successfully detected CH_3COOH with two degenerate transitions toward G19.61-0.23. Therefore, following Sgr B2(N-LMH), W51e2 and G34.3+0.15, G19.61-0.23 is the fourth high-mass hot core source of CH_3COOH to date. The column density of CH_3COOH is 2.4×10^{16} cm^{-2} and the abundance ratio of CH_3COOH to methyl formate ($HCOOCH_3$) is 8.5×10^{-2}; both are comparable to the other CH_3COOH sources. The CH_3COOH emission is cospatial with other large O and N-bearing molecules, which indicates that O-rich and N-rich chemistry are strongly correlated with CH_3COOH formation i.e. no O/N chemical differentiation exists in the CH_3COOH sources. We did not detect CH_3COOH in either IRAS 16293-2422 or NGC 1333 IRAS 4A. IRAS 16293-2422 has been reported as the first low-mass CH_3COOH source by Cazaux et al. Based on their report, our observation should have reached the required sensitivity and detected CH_3COOH. Thus, the CH_3COOH in IRAS 16293-2422 is still not confirmed. Moreover, we have detected $HCOOCH_3$ but not ethyl cyanide (CH_3CH_2CN) in IRAS 16293-2422, suggesting that it lacks active N-rich chemistry and may not be yet chemically and physically suitable for CH_3COOH formation.

2.1 INTRODUCTION

To date, over 130 molecular species have been detected in the interstellar medium (ISM) (**?**). Especially, a diversity of large and complex organic species is abundant in hot molecular cores (e.g. Miao et al. 1995; Mehringer & Snyder 1996). Hot molecular cores (HMCs) have high temperature (T > 100 K) and high molecular density (n > 10^6 cm^{-3}). Furthermore, HMCs have been suggested as active star forming regions. The discoveries of large organic molecules link chemical evolution and star formation in hot cores, including planet formation. Among these large organic molecules, acetic acid (CH_3COOH) is probably the most

biologically important due to its association with glycine (NH_2CH_2COOH), which is key to the origin of life. It is possible that many prebiotic or large molecules were formed in the ISM and then embedded in comets, asteroids and meteorites traveling to the early earth to trigger biological evolution (Bernstein et al. 1999). However, to date, the pathways of NH_2CH_2COOH formation in the ISM still remain unclear. CH_3COOH structurally contains the same C-C-O backbone as NH_2CH_2COOH with a difference of the radical NH_2^+. Thus, CH_3COOH is very likely one of the important precursors in NH_2CH_2COOH formation (Mehringer et al. 1997).

Interstellar CH_3COOH was first discovered in Sgr B2(N-LMH) (Large Molecule Heimat) with the Berkeley-Illinois-Maryland Association (BIMA) and Owens Valley Radio Observatory (OVRO) millimeter-wavelength arrays by Mehringer et al. (1997). With high resolution observation, Sgr B2 has been resolved into many clumps (see Friedel et al. 2004); among these clumps, Sgr B2(N-LMH) is a molecule-rich hot core that has been the best place to search for large and complex molecules. The compactness of the CH_3COOH emission in Sgr B2(N-LMH) ($<3''$) highlights the importance of interferometers. To clearly detect CH_3COOH and other large molecules toward hot cores embedded in clumpy clouds, high resolution interferometric observation is a necessity. Thus, following the first CH_3COOH detections in Sgr B2(N-LMH), Remijan et al. (2002) confirmed the CH_3COOH detections in Sgr B2(N-LMH) and discovered the second CH_3COOH hot core, W51e2, with the BIMA array. Later on, Remijan et al. (2003) launched an extensive CH_3COOH survey of 12 galactic hot cores, including high-mass (≥ 10 $M_\odot$) and low-mass (< 10 $M_\odot$) sources, and they found the third CH_3COOH high-mass hot core, G34.3+0.15.

Acetic acid (CH_3COOH), methyl formate ($HCOOCH_3$) and glycolaldehyde (CH_2OHCHO) are isomers. However, their abundances and spatial distributions in Sgr B2(N-LMH) are dissimilar. The emissions of CH_3COOH and $HCOOCH_3$ are compact (2-5$''$, Remijan et al. 2002) while that of CH_2OHCHO is extended (60$''$, Hollis et al. 2001). The abundance of $HCOOCH_3$ is 26 times higher than that of CH_3COOH and 52 times that of CH_2OHCHO. The chemical difference suggests that hot core chemistry is active and may be affected by physical conditions in the vicinity.

Gas phase and grain surface chemistry both play critical roles in the formation of large molecules (Hasegawa, Herbst, & Leung 1992; Garrod & Herbst 2006; Garrod, Weaver, & Herbst 2008). Like glycine, the pathways of CH_3COOH formation in the ISM are still unclear. Remijan et al. (2004) have suggested that both N-bearing and O-bearing molecules may play important roles in CH_3COOH formation, even if it lacks nitrogen atoms. The reported CH_3COOH sources have shown no O and N-rich chemical differentiation at all, while some molecule-rich hot cores with distinguishable O/N chemical differentiation, such as Orion KL (e.g. Sutton et al. 1995) and W3(OH) (e.g. Remijan et al. 2003), do not show comparable

CH_3COOH detections. Thus, large O and N-bearing molecules are strongly related to CH_3COOH detection. To investigate this premise, we observe methyl formate ($HCOOCH_3$) and ethyl cyanide (CH_3CH_2CN) in our survey to indicate the chemical preference of the hot cores.

The rotational transitions of large molecules at 3 mm wavelengths are weak compared with diatomics and maser species. As hot cores are extremely compact with other nearby molecular clumps, spectral line confusion is a severe problem in large molecule surveys (e.g. Friedel et al. 2004). Thus, interferometers are required to resolve the molecular lines and gain good signal coupling with the hot cores to best obtain a high signal to noise ratio (SNR). To search for acetic acid and address its relationship with O/N chemical differentiation, we have used the high sensitivity of the Combined Array for Research in Millimeter-wave Astronomy (CARMA) to carry out an acetic acid survey toward three hot cores. The observed sources are G19.61-0.23, IRAS 16293-2422 and NGC 1333 IRAS 4A, and the observed molecules are acetic acid (CH_3COOH), methyl formate ($HCOOCH_3$) and ethyl cyanide (CH_3CH_2CN).

2.2 OBSERVED SOURCES

2.2.1 G19.61-0.23

G19.61-0.23 is a molecule-rich ultracompact H II region, which is also a high-mass hot core. Numerous masers have been detected in this region, including OH (Matthews et al. 1977; Garay, Reid, & Moran 1985) , H_2O (Genzel & Downes 1977), CH_3OH (Kalenskii et al. 1994; Larionov et al. 1999). NH_3 (Garay et al. 1998), CS (Shirley et al. 2003; Wu & Evans 2003; Larionov et al. 1999), HCN (Wu & Evans 2003) and CO (Hofner et al. 2000). Methyl formate ($HCOOCH_3$) and ethyl cyanide (CH_3CH_2CN) have been detected by Remijan et al. (2004), which shows a high possibility of the existence of acetic acid (CH_3COOH). We have used the BIMA array to search for CH_3COOH in G19.61-0.23 (Remijan et al. 2004). However, the CH_3COOH transitions were below our detection limit at that juncture. Based on the reported CH_3COOH sources, the abundance ratio of CH_3COOH to $HCOOCH_3$ seems universal in high-mass CH_3COOH hot cores. If G19.61-0.23 indeed contains CH_3COOH, our $HCOOCH_3$ detection indicated that the CH_3COOH transitions are just slightly lower than the BIMA sensitivity. To clearly detect the CH_3COOH transition lines, we needed a higher sensitivity by a factor of 4, which could be provided by CARMA in this survey.

2.2.2 IRAS 16293-2422

IRAS 16293-2422 is one of the most well-studied and observed low-mass star forming regions. It consists of two clumps denoted as component A and B (hereafter I16293A and B). The structure of I16293A is

much more complex than I16293B. I16293A has been reported to contain two centimeter sources A1 and A2 (Wootten 1989), and two submillimeter sources Aa and Ab (Chandler et al. 2005). Moreover, I16293A2 has recently been reported to be a bipolar ejection with components A2α and A2β (Loinard et al. 2006). Despite their low masses, both component A and B have been suggested to be as molecule-rich as high-mass hot cores Schöier et al. (e.g. 2002); Cazaux et al. (e.g. 2003).

Large O-bearing molecules, methyl formate, formic acid (HCOOH), and N-bearing molecules, methyl cyanide (CH_3CN), vinyl cyanide (CH_2CHCN) and ethyl cyanide (CH_3CH_2CN) have been detected (Cazaux et al. 2003; Bottinelli et al. 2004a; Kuan et al. 2004; Remijan & Hollis 2006). With the Institute de Radioastronomie Millimétrique 30-m (IRAM) telescope, Cazaux et al. (2003) have reported the CH_3COOH detection of $9_{*,9} - 8_{*,8}$ E line at 100.855 GHz. That makes IRAS 16293-2422 the only low-mass CH_3COOH source to date. However, Cazaux et al. (2003) did not detect the counterpart, $9_{*,9} - 8_{*,8}$ A line. The IRAM single dish had a 28″ beam compared with an estimated source size of 5″; beam dilution may severely degrade the detection or the IRAM beam may pick up interlopers. To confirm the CH_3COOH in IRAS 16293-2422, we observed two CH_3COOH transitions in this survey with the high resolution of the CARMA, which can clearly resolve the A and B components.

2.2.3 NGC 1333 IRAS 4A

NGC 1333 IRAS 4A is a low-mass protostellar binary system first designated as A1 and A2 by Looney, Mundy, & Welch (2000). Reipurth et al. (2002) have resolved this 1.″8 binary system with the Very Large Array (VLA). Blake et al. (1995) have conducted a 1 mm survey and detected CO, CS, SIO, SO, HCN, DCN, HNC, HCO^+, DCO^+, N_2H^+, CH_3OH and H_2CO. Moreover, Bottinelli et al. (2004b) have shown that this region contains many large molecules by detecting methyl formate ($HCOOCH_3$), formic acid (HCOOH) and methyl cyanide (CH_3CN). Therefore, it is indeed a molecule abundant region and needs to be further investigated in our acetic acid survey.

2.3 OBSERVATIONS

The acetic acid (CH_3COOH) survey was carried out with the CARMA 3 mm receivers from spring 2006 to spring 2008 in the B and C configurations. The individual angular resolutions are about 1″ and 2″, respectively. Table 2.1 summarizes the properties of the observed sources, which includes the source position, gain calibrators, flux calibrators, distances, masses and LSR velocities. The six windows in the CARMA correlator were configured as two wide-band and four narrow-band windows. The wide-band window has 500

Table 2.1. OBSERVED SOURCES

Source	α (J2000.0)	δ (J2000.0)	Flux calibrator	Gain calibrator	Distance (kpc)	Mass ($M_\odot$)	v_{LSR} (km s^{-1})
G19.61-0.23[a]	18 27 38.1	-11 56 39.0	Neptune	1911-201	3.50	450	40.0
IRAS 16293-2422[b]	16 32 22.8	-24 28 33.0	MWC349	1625-254, 1733-130	0.16	5.4	3.9
NGC 1333 IRAS 4A[c]	03 29 10.3	31 13 31.7	Uranus	3c84	0.35	0.8	6.7

[a]Furuya et al. (2005)

[b]Schöier et al. (2002)

[c]Di Francesco et al. (2001)

Table 2.2. OBSERVED MOLECULES AND TRANSITIONS

Species	Transition	Frequency (MHz)	E_u (K)	$< S_{j,j}\mu^2 >$ (debye^2)
CH_3COOH[a]	$10_{*,10} - 9_{*,9}$ E	111,507.270(40)	30.5	54.8
	$10_{*,10} - 9_{*,9}$ A	111,548.533(40)	30.5	54.8
$HCOOCH_3$[b]	$9_{2,8} - 8_{2,7}$ E	107,537.189(24)	28.8	22.8
	$9_{2,8} - 8_{2,7}$ A	107,543.746(26)	28.8	22.8
CH_3CH_2CN[c]	$12_{3,10} - 11_{3,9}$	107,594.049(28)	43.6	166.8
	$12_{4,9} - 11_{4,8}$	107,543.926(26)	51.4	158.1
	$12_{4,8} - 11_{4,7}$	107,547.601(26)	51.4	158.1

Note. — The uncertainty of the frequencies is in units of kHz.

[a]Ilyushin, Kleiner, & Lovas (2008); the rotational partition is $Q_r = 14.1T_r^{3/2}$.

[b]Oesterling et al. (1999); $Q_r = 12.45T_r^{3/2}$.

[c]Lovas (1982); $Q_r = 7.17T_r^{3/2}$.

MHz bandwidth and 15 channels while the narrow-band window has 31 MHz bandwidth and 63 channels. The narrow-band high spectral resolution is 0.49 MHz per channel, which can provide sufficient sensitivity to resolve the observed transitions and lower the line confusion effect to detect large molecules. The amplitude and phase calibrations were accomplished by observing the gain and flux calibrators. During data reduction, pointing and system temperatures were checked to monitor data quality.

We observed the $10_{*,10} - 9_{*,9}$ E and A CH_3COOH lines at 111.50727 and 111.548533 GHz (Ilyushin, Kleiner, & Lovas 2008) in two narrow band windows. Based on previous observations (Remijan et al. 2002, 2003), they are unblended and have the same line strength. In addition to CH_3COOH, we include two methyl formate ($HCOOCH_3$) and three ethyl cyanide (CH_3CH_2CN) lines in the other narrow-band windows. $HCOOCH_3$ is the tracer for O-rich chemistry while CH_3CH_2CN is for N-rich chemistry. Table 2.2 summarizes the observed molecules and their transitions.

2.4 RESULTS

The observational data were reduced with the MIRIAD package (Sault et al. 1995). To increase the signal-to-noise ratio (SNR), spectra were Hanning-smoothed over 3 channels and continuum-subtracted. The observations in the B and C configuration were combined using nature weighting to obtain the best sensitivity.

2.4.1 Column Densities

Molecular column densities are essential physical parameters to constrain chemical models. First, we have applied least-square fitting with Gaussian functions to determine linewidths (Δv), intensities (ΔI) and $\int I dv$ (Miao et al. 1995). Then, assuming a molecular species in local thermodynamic equilibrium (LTE), its column density is

$$N_T(\mathrm{cm}^{-2}) = 2.04 \times 10^{20} \frac{\int I(\mathrm{Jy\ beam}^{-1}) dv(\mathrm{km\ s}^{-1}) Q_r e^{E_u(K)/T_r}}{\Omega_b(\mathrm{arcsec}^2)\nu^3(\mathrm{GHz}^3) < S\mu^2 > (\mathrm{debye}^2)}, \tag{2.1}$$

where Ω_b is the beam size, $\int I_v dv$ is the integral of the line intensity over velocity, ν is the spectral line frequency and $< S\mu^2 >$ is the line strength parameter. Q_r is the rotational partition function.

Rotational temperature, T_r, is generally obtained by the rotational temperature diagram method, which requires multiple detections of molecular transitions with various upper energy levels. In this work, the observed CH_3COOH transitions have very similar upper energies E_u and hence the uncertainty of the rotational temperature is enormous. However, we may adopt rotational temperatures from other well-detected molecules in each source to estimate column densities.

2.4.2 G19.61-0.23

Two acetic acid (CH_3COOH) transition lines toward G19.61-0.23, $10_{*,10} - 9_{*,9}$ E and $10_{*,10} - 9_{*,9}$ A, were detected in the two CH_3COOH spectral windows (Figure 2.1). The $10_{*,10} - 9_{*,9}$ E line is at the v_{LSR} of 40 km s^{-1} in Figure 2.1(a) as the $10_{*,10} - 9_{*,9}$ A line is in Figure 2.1(b). While some weak unidentified lines appear in the windows, The line strengths of the transitions are roughly equal as theoretically predicted. We have combined the two lines to produce CH_3COOH contours overlapping the continuum map in gray scale in Figure 2.2. G19.61-0.23 consists of several clumps at 3 mm wavelengths; the CH_3COOH emission is located at the center clump, the component C. Here we use the notation from Furuya et al. (2005). The other components are more extended than component C ($2'' \times 2''$). Remijan et al. (2004) was not able to detect the CH_3COOH with the BIMA array in G19.61-0.23 perhaps due to their large beam ($17'' \times 5\farcs5$)

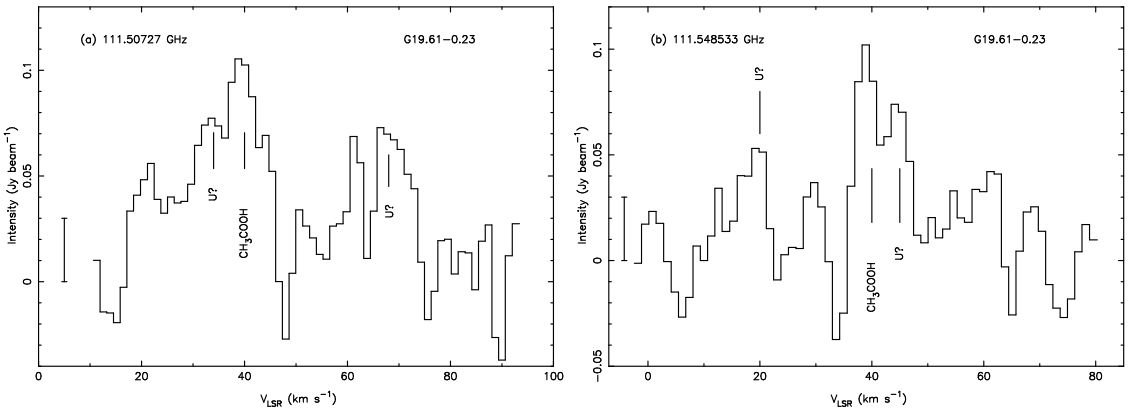

Figure 2.1 (a) and (b) are CH_3COOH spectra toward G19.61-0.23. The rms noise level is $\sigma = 0.03$ Jy beam^{-1}. (a) The $10_{*,10} - 9_{*,9}$ E transition is at the v_{LSR}, 40 km s^{-1}. U? marks two unidentified lines below 3σ but over 1σ. (b) The $10_{*,10} - 9_{*,9}$ A transition and two unidentified lines are shown.

Table 2.3. DETECTED MOLECULES AND TRANSITIONS TOWARD G19.61+0.23

Species	Transition	$\int Idv$ (Jy beam^{-1} km s^{-1})	ΔI (Jy beam^{-1})	Δv (km s^{-1})
CH_3COOH	$10_{*,10} - 9_{*,9}$ E	1.1±0.08	0.09±0.08	11.3±1
	$10_{*,10} - 9_{*,9}$ A	0.6±0.1	0.1±0.02	5.5±1
$HCOOCH_3$	$9_{2,8} - 8_{2,7}$ E	3.0±0.04	0.34±0.04	8.1±0.9
	$9_{2,8} - 8_{2,7}$ A	3.0±0.04	0.34±0.04	8.1±0.9
CH_3CH_2CN	$12_{3,10} - 11_{3,9}$	15.8±0.58	0.78±0.01	19.0±0.5
	$12_{4,9} - 11_{4,8}$	7.8±0.35	0.61±0.05	14.1±0.7
	$12_{4,8} - 11_{4,7}$	11.4±0.35	0.76±0.03	15.2±0.7

Note. — The $HCOOCH_3$ lines are assumed to have the same line peak and linewidth.

without a good signal coupling to component C.

In addition to CH_3COOH, we have detected methyl formate ($HCOOCH_3$) and ethyl cyanide (CH_3CH_2CN) as shown in Figure 2.3. Two degenerate transitions of $HCOOCH_3$, $9_{2,8} - 8_{2,7}$ A/E and two transitions of CH_3CH_2CN, $12_{4,9} - 11_{4,8}$ and $12_{4,8} - 11_{4,7}$, are shown in Figure 2.3(a). In Figure 2.3(b), along with two strong unidentified lines, a bright CH_3CH_2CN transition, $12_{3,10} - 11_{3,9}$, is at the v_{LSR} of 40 km s^{-1}. The $HCOOCH_3$ map (Figure 2.4) and CH_3CH_2CN map (Figure 2.5) show that both emissions mainly come from the component C as CH_3COOH.

To calculate the column densities of the detected molecules, we need to determine the spectral parameters. Table 2.3 summarizes the fitting results of the detected transitions toward G19.61-0.23. In our fitting routine, we assume that the $HCOOCH_3$ transitions share the same linewidth and peak intensity. The column density of CH_3COOH is estimated to be 2.4×10^{16} cm^{-2} using a rotational temperature of 230 K from Kurtz et al. (2000). The column density of $HCOOCH_3$ is 2.8×10^{17} cm^{-2} and the column density of CH_3CH_2CN is 1.3×10^{17} cm^{-2}.

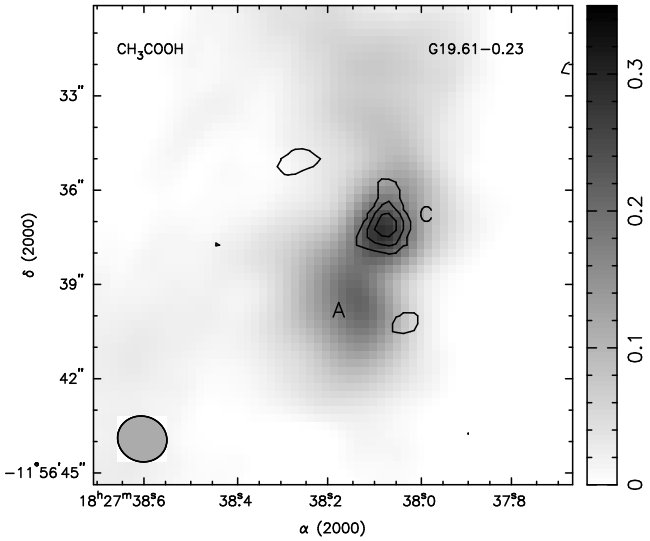

Figure 2.2 CH_3COOH contours overlap with the gray continuum map. The contour levels are 2, 3, 4 × σ = 0.024 Jy beam^{-1}. The gray scale unit is Jy beam^{-1}. The beam size is 1.″7×1.″4 (P.A.=36.4°). The CH_3COOH emission is from the component C.

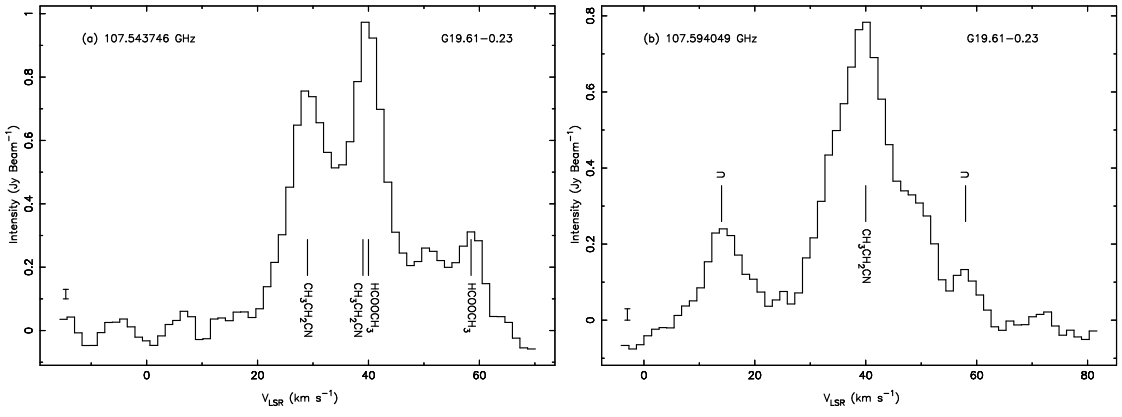

Figure 2.3 (a)$HCOOCH_3$ and CH_3CH_2CN are detected toward G19.61-0.23. The rms noise level is σ = 0.025 Jy beam^{-1} (b) CH_3CH_2CN and two over 3σ unidentified lines denoted as U are shown.

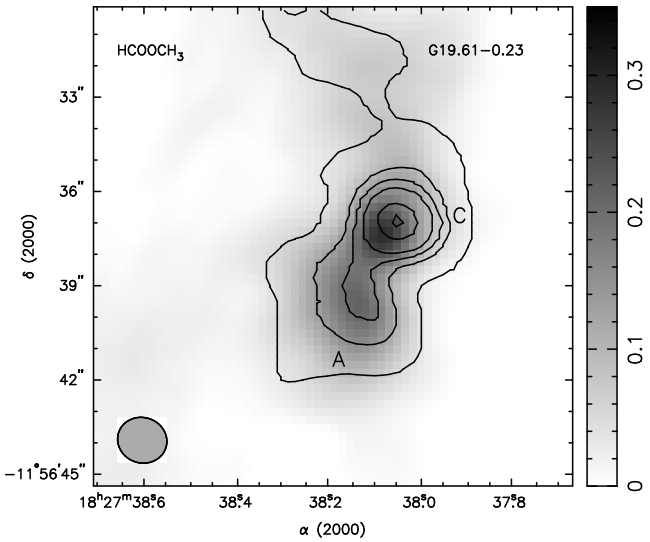

Figure 2.4 $HCOOCH_3$ contours overlay with the gray continuum map. The contour levels averaged over 3 channels are 3, 9, 12, 15, 21, 24 and 27 $\times$ σ = 0.02 Jy beam^{-1}. The beam size is 2.″2×1.″7 (P.A.=59.3°). $HCOOCH_3$ emission is slightly extended to the component A.

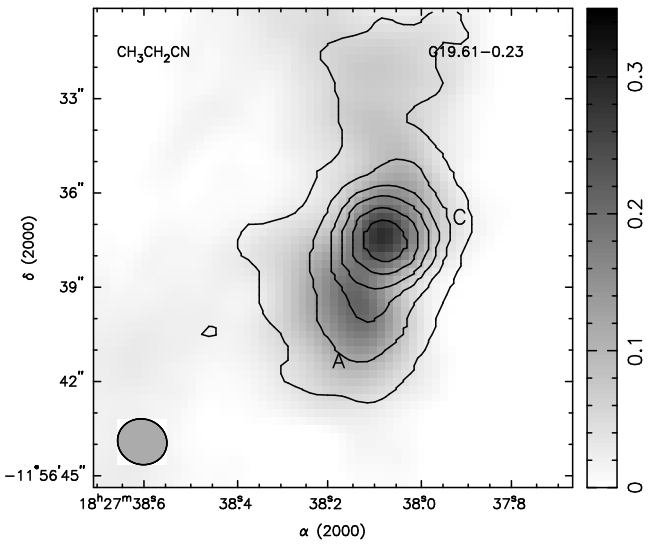

Figure 2.5 CH_3CH_2CN contours overlay with the gray continuum map. The contour levels averaged over 6 channels, are 3, 9, 15, 21, 30, 40, 50 and 60 $\times$ σ = 0.018 Jy beam^{-1}. The beam size is 2.″2×1.″7 (P.A.=60.3°).

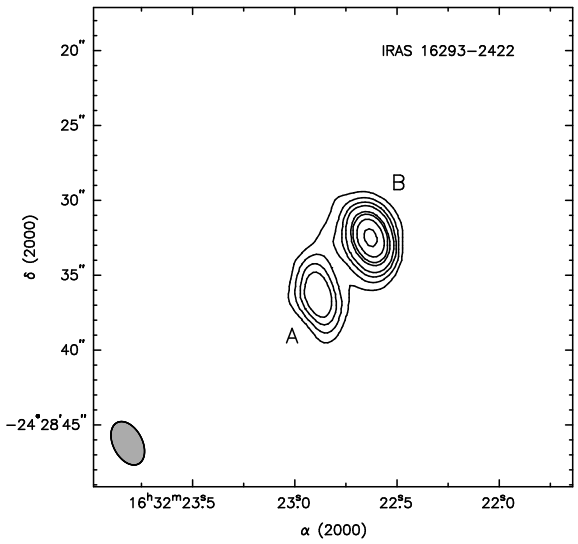

Figure 2.6 Continuum map of IRAS 16293-2422. The contour levels are 6, 9, 12, 15, 21, 24, 30, 40 and 50 $\times\ \sigma = 0.003$ Jy beam^{-1}. The angular resolution of the observation is 2.″0×1.″3 (P.A.=87.1°)

Table 2.4. DETECTED MOLECULES AND TRANSITIONS TOWARD IRAS 16293-2422

Species	Transition	$\int Idv$ (Jy beam^{-1} km s^{-1})	ΔI (Jy beam^{-1})	Δv (km s^{-1})
$HCOOCH_3$	$9_{2,8} - 8_{2,7}$ E	0.32±0.11	0.067±0.012	4.4±0.9
	$9_{2,8} - 8_{2,7}$ A	0.41±0.13	0.061±0.01	6.2±1.2

2.4.3 IRAS 16293-2422

We have successfully resolved IRAS 16293-2422 into I16293A and B with our 2.″2× 1.″7 beam in Figure 2.6. Our primary target in IRAS 16293-2422 is I16293B (5″× 5″), which should show more distinct spectral features. Therefore, the beam dilution in this observation is minimized. However, we did not detect the CH_3COOH transition lines (Figure 2.7) toward I16293B. We have only confirmed $HCOOCH_3$ with two new transitions (Figure 2.8) but did not detect CH_3CH_2CN either.

Table 2.4 summarizes the fitting results of the $HCOOCH_3$ transitions. The 3σ upper limit of the column density of the CH_3COOH is 3.5×10^{14} cm^{-2} using a rotational temperature of 80 K from Bottinelli et al. (2004a). The column density of $HCOOCH_3$ is 1.4×10^{16} cm^{-2} and the 3σ upper limit column density of CH_3CH_2CN is 7.7×10^{13} cm^{-2}. The upper limits are taken with the integrated intensity over three channels.

2.4.4 NGC 1333 IRAS 4A

We did not detect any molecular transitions toward NGC 1333 IRAS 4A. This binary system is not resolved with our angular 5″×3″so beam dilution may be severe. Figure 2.9 shows the CH_3COOH windows. The 3σ

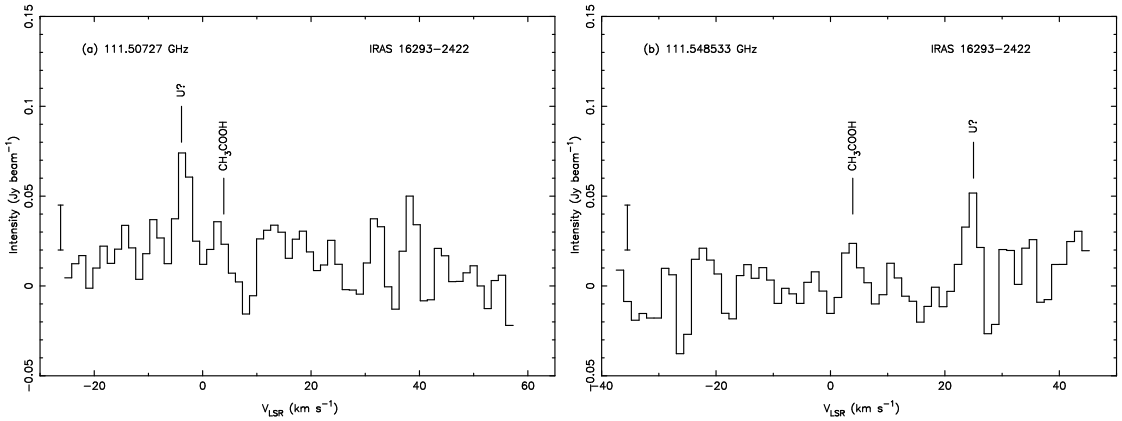

Figure 2.7 The CH_3COOH spectra of $10_{*,10} - 9_{*,9}$ E transition in (a) and $10_{*,10} - 9_{*,9}$ A in (b) toward I16293B. The rms noise level is 0.025 Jy beam^{-1} and the v_{LSR} is 3.9 km s^{-1}.

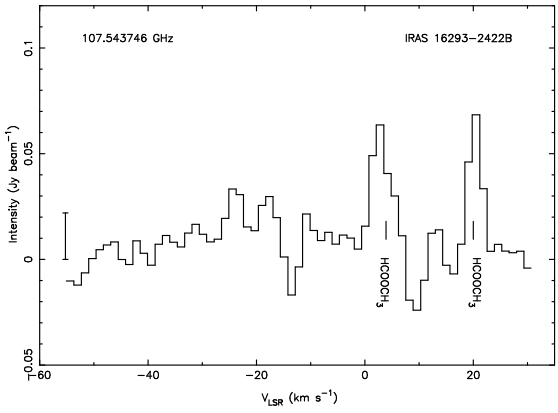

Figure 2.8 $HCOOCH_3$ spectrum toward I16293B. The rms noise level is 0.023 Jy beam^{-1} and the v_{LSR} is 3.9 km s^{-1}.

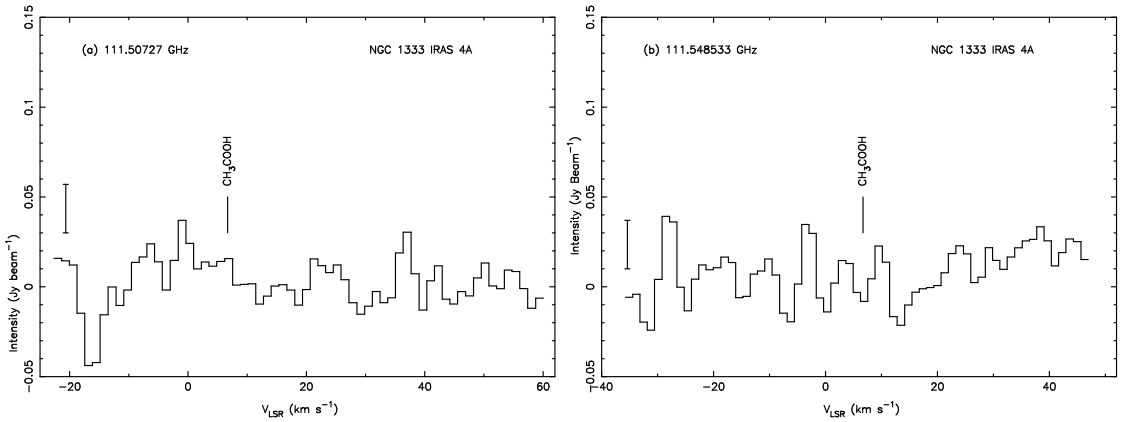

Figure 2.9 The CH_3COOH spectra of $10_{*,10} - 9_{*,9}$ E transition in (a) and $10_{*,10} - 9_{*,9}$ A in (b) toward NGC 1333 IRAS 4A. The noise levels are 0.027 Jy beam^{-1} and the v_{LSR} is 6.7 km s^{-1}.

Table 2.5. COLUMN DENSITIES OF THE OBSERVED MOLECULES

Species (cm^{-2})	G19.61-0.23	IRAS 16293-2422	NGC 1333 IRAS 4A
CH_3COOH	$(2.4\pm0.5)\times10^{16}$	$\leq3.5\times10^{14}$	$\leq 1.8\times10^{14}$
$HCOOCH_3$	$(2.8\pm0.1)\times10^{17}$	$(1.4\pm0.4)\times10^{16}$	$\leq 4.3\times10^{14}$
CH_3CH_2CN	$(1.3\pm0.1)\times10^{17}$	$\leq 7.7\times10^{13}$	$\leq 5.1\times10^{13}$

Note. — The column densities are in units of cm^{-2}.

upper limit of the column densities of CH_3COOH, $HCOOCH_3$ and CH_3CH_2CN are 1.8×10^{14}, 4.3×10^{14} and 5.1×10^{13} cm^{-2}, respectively. Here, we assume that the rotation temperatures of CH_3COOH and CH_3CH_2CN are 36 K as that of $HCOOCH_3$ from Bottinelli et al. (2004b).

2.5 DISCUSSION

2.5.1 Acetic Acid Sources

We have successfully detected acetic acid (CH_3COOH) toward G19.61-0.23. G19.61-0.23 is the fourth high-mass CH_3COOH hot core, following Sgr B2(N-LMH), W51e2 and G34.3+0.15. We can compare these CH_3COOH hot cores with the CH_3COOH column density and the abundance ratio to methyl formate ($HCOOCH_3$) in Table 2.6. CH_3COOH and $HCOOCH_3$ are isomers; however, they do not share the same column density. It is of interest that the CH_3COOH column density and abundance ratios in the hot cores are similar. The column densities are about 10^{16} cm^{-2} and the ratios are about 10^{-2}. Therefore, the consistent ratio may reliably be used to constrain the chemical models of CH_3COOH formation.

When CH_3COOH was first detected with interferometers (Mehringer et al. 1997), it emphasized the important use of interferometers for the study of astrochemistry in hot cores. The CH_3COOH detection toward G19.61-0.23 was conducted with an extremely compact beam size, $1\farcs6\times1\farcs9$, which is the smallest to date used in the acetic acid survey. Numerous works have reported that G19.61-0.23 (Furuya et al. 2005) and other hot cores have very complex structures, which include compact and extended clumps. While large molecule emissions are mostly from those compact clumps, our three observed molecules in G19.61-0.23 are located at the same component, and that agrees with the CH_3CH_2CN observation by Furuya et al. (2005). As we continue extending acetic acid survey to smaller hot cores, the required resolution of observations may be higher.

Although the detected emission of CH_3COOH is compact, lower abundance CH_3COOH may be extended in a larger region. The key parameters of successful detection is the beam size and the size of the high concentration of large molecules. The emission of dense large molecules need to be higher than noise levels so they can be detected. Large molecule formation possibly begins at near the center of the hot core, which has the higher temperature but not too high to destroy them. The CH_3COOH at the edge of the hot core may form later but not as abundantly as that at the vicinity of the center. Without considering the density differentiation in hot cores, chemical models may be misled by observational results. We suggest to employ radiative transfer models with dynamical evolution models in the chemical models (e.g. Rodgers & Charnley 2003).

2.5.2 O and N Chemistry in Hot Cores

G19.61-0.23 and the other CH_3COOH sources have demonstrated that a diversity of abundant large O and N-bearing species and CH_3COOH are strongly correlated. One possibility is that the mix of O and N-bearing species may serve as an efficient chemical network for CH_3COOH and other large molecules. Thus, they need to wait for large N-bearing molecules to form first before they can be efficiently produced. Another possibility is that if O/N chemical differentiation is simply time dependent, gas-phase CH_3COOH concentration just by coincidence starts to increase along with large N-bearing species.

As higher resolution maps and spectra reveal the morphology of molecular emission, O and N-bearing molecules are not fully co-spatial in some complex hot cores, such as Orion-KL (e.g. Blake et al. 1987; Friedel & Snyder 2008) and W3(OH) (e.g. Remijan et al. 2003). Blake et al. (1987) and Rodgers & Charnley (2001) have suggested the difference of O and N-rich chemistry reflects the timescales of chemical evolution in some cases. N-bearing molecules represent the later stage of the evolution while O-bearing molecules represent the earlier stage. Their models can indicate the ages of hot cores by comparing the

O and N chemical differentiation; however, no direct observation can measure the hot core ages. The uncertainty of this method is still high until the chemical models can be fully confirmed.

The gas phase and grain surface chemistry both undoubtedly play important roles in hot cores (Hasegawa, Herbst, & Leung 1992; Garrod & Herbst 2006; Garrod, Weaver, & Herbst 2008). Large molecule abundances can be enhanced enormously by the grain surface chemistry while the gas phase chemistry alone is not sufficient to match observations. Garrod & Herbst (2006) have demonstrated radicals on grain surfaces can move around when temperature gradually increases from 10 to 200 K in the regions of star formation. The grain surfaces become efficient environments for large molecules to form. Heavy radicals become mobile on the grain surfaces at the warm-up stage. However, the details of CH_3COOH formation in hot cores still remain unclear. The correlation between CH_3COOH and large N-bearing molecules may suggest that some N-bearing molecules are catalysts indirectly to CH_3COOH formation. In short, the chemical and physical evolution timescales of star formation lacks direct observational evidence to confirm chemical models. Without the support of observation, it is difficult to establish solid chemical models. Garrod, Weaver, & Herbst (2008) have reported their new chemical model in CH_3COOH hot cores. Grain surface reactions have been enhanced to meet the observation. However, the model assumes all molecules are co-spatial with a simple heating process. Based on our survey, it is important to investigate the chemical models with spatially physical differentiation. Some molecules are extended in the hot cores while some molecules may be compact. Large O- and N-bearing species may have distinct chemical pathways while the CH_3COOH pathways may go through both. Therefore, to examine chemical pathways, we suggest to further test chemical models with various physical and chemical conditions.

2.5.3 Acetic Acid in IRAS 16293-2422?

IRAS 16293-2422 has been reported as the first low-mass CH_3COOH source by Cazaux et al. (2003) with the IRAM 30 m telescope. In this work, we have resolved IRAS 16293-2422 into I16293A and B. I16293B is a better place in IRAS 16293-2422 to identify new molecular transitions. The single dish beam size used by Cazaux et al. (2003) is $28''$ and I16293B is less than $5''$. According to their result, we should have detected the CH_3COOH lines at more than 200 mJy beam^{-1} with our synthesized beam, $3\farcs1\times1\farcs9$. We have a smaller beam and higher line strength parameter in this survey. The CH_3COOH transitions are still below our detection limit. By setting 3σ noise level, the upper limit of CH_3COOH is 3.5×10^{14} cm^{-2}, which is lower than the 2.6×10^{15} cm^{-2} reported by Cazaux et al. (2003).

We have confirmed methyl formate ($HCOOCH_3$) in 16293-2422B but we did not detect ethyl cyanide (CH_3CH_2CN). The upper limit of $HCOOCH_3$ in our survey is 5.1×10^{13} cm^{-2}. Perhaps N-rich chemistry in

Table 2.6. COMPARISON OF ACETIC ACID SOURCES

Species	Sgr B2(N-LMH)[a]	W51e2[b]	G34.3+0.15[c]	G19.61-0.23
N_{CH_3COOH} (cm^{-2})	7.3×10^{15}	1.7×10^{16}	$(0.77\text{-}1.64)\times10^{15}$	2.4×10^{16}
$N_{CH_3COOH}/N_{HCOOCH_3}$	$(4\text{-}7)\times10^{-2}$	$(1\text{-}6)\times10^{-2}$	3.3×10^{-2}	8.5×10^{-2}

[a]Mehringer et al. (1997); T_r =200 K

[b]Remijan et al. (2002); T_r =201 K

[c]Remijan et al. (2003); T_r =70-185 K

IRAS 16293-2422 may be just starting weakly to occur with a warm temperature (80 K); I16293B is still at the early stage of the hot core chemical evolution. Since large N-bearing species are not abundant, it is consistent with the non-detection of CH_3COOH.

2.5.4 NGC 1333 IRAS 4A

NGC 1333 IRAS 4A has been reported with $HCOOCH_3$ detections by Bottinelli et al. (2004b). To date, CH_3CH_2CN or other large N-bearing molecules has not detected in NGC 1333 IRAS 4A. Compared with hot core temperatures (T > 100K), NGC 1333 IRAS 4A temperature of 36 K is considerably low. NGC 1333 IRAS 4A may be at very early stage of star formation. As discussed above, rich N-bearing molecules are important to CH_3COOH detection. The lack of CH_3CH_2CN detections in NGC 1333 IRAS 4A may agree with the non-detections of CH_3COOH.

2.6 SUMMARY

We have conducted a high resolution acetic acid (CH_3COOH) survey at 3 mm wavelengths for the first time with CARMA towards a high-mass hot core, G19.61-0.23, and two low-mass embedded protostar systems, IRAS 16293-2422 and NGC 1333 IRAS 4A. We have discovered CH_3COOH in G19.61-0.23, with two CH_3COOH transitions, $10_{*,10} - 9_{*,9}$ E and A. While G19.61-0.23 consists of several clumps, the high resolution maps reveal that the CH_3COOH emission is extremely compact ($<2''$) at component C. Other large molecules, such as methyl formate and ethyl cyanide, are detected with slightly larger emission regions but the peaks of the emissions are also at component C. The $HCOOCH_3$ column density and abundance ratio to methyl formate ($HCOOCH_3$), are 2.4×10^{16} cm^{-2} and 8.5×10^{-2} respectively, which are comparable to the other high-mass CH_3COOH sources. We have detected methyl formate ($HCOOCH_3$) in IRAS 16293B-2422 with two new transitions, $9_{2,8} - 8_{2,7}$ E and A. However, we did not detect CH_3COOH or ethyl cyanide (CH_3CH_2CN) in IRAS16293-2422. The detection are mainly toward I16293B, which shows narrower and

more distinguishable line profiles. We suggest that IRAS 16293-2422 may lack active N-rich chemistry for CH_3COOH formation or it is still at a fairly early stage of the hot core chemical evolution. While NGC 1333 IRAS 4A is not spatially resolved and the noise levels are still considerably high in this work, none of the observed molecular transitions were detected. Higher resolution and sensitivity observation is needed to further investigate large molecules in this region.

The CH_3COOH detection has highlighted the importance of the diversity of N and O-rich chemistry in hot cores for the formation of CH_3COOH and perhaps other large molecules. The timescale of hot cores may also play a role in N and O-rich chemistry and hence CH_3COOH formation. However, we need more CH_3COOH detections to confirm these suggestions. The compactness of large molecule emission stresses the need of interferometers for hot core chemistry. Our high resolution survey has provided critical information on the chemical and physical conditions in hot cores, which can be used to constrain the chemical models of molecular formation. Higher resolution observations are still required to precisely determine temperature and the density distribution of large O and N-bearing molecules, which are essential to physical-parameter sensitive chemical models. Through well-improved chemical models, we can better understand the distinctive hot core chemistry.

Chapter 3

Introduction to Water Vapor Radiometer Phase Corrections

Radio astronomers constantly exploit cutting edge technology to obtain high resolution astronomical images and spectra at various wavelengths for their scientific goals. However, Earth's atmosphere plays a crucial part in observational quality for ground-based telescopes. New technology cannot solely produce high quality data without a translucent and stable atmosphere. The atmosphere is opaque except for several windows at the infrared, visible light and radio regions. Moreover, within these windows, the opacity and the refraction index of the atmosphere vary in terms of time and space. The variation of the opacity changes the amplitude of astronomical signals while the variation of the refraction index causes phase incoherence. The wavefronts of the signals, which should be perfectly perpendicular to the propagating direction, are distorted randomly.

For radio interferometers, phase incoherence severely affects observational quality. Generally, the scale of the phase incoherence is much greater and faster than that of the amplitude variation. It is necessary to compensate the phase incoherence with phase correction techniques. The phase incoherence is due to tropospheric water vapor turbulence. Therefore, by observing the water vapor turbulence, water vapor radiometers may provide a new phase correction technique. In this chapter, we first introduce interferometers and tropospheric water vapor. Then we demonstrate the phase incoherence effect on interferometric observations and the water vapor phase correction technique.

3.1 Interferometer

Radio astronomy has unlocked many fundamental questions in astronomy such as the discoveries of the cosmic microwave background (CMB) in 1965 (Penzias & Wilson 1965; Dicke et al. 1965) and the first pulsar in 1967 (Hewish et al. 1968). These radio observations were carried out at centimeter wavelengths. Over the last 50 years, with technology advancing, the observable wavelength band has been extended from centimeter to submillimeter. To date, novel devices, such as superconductor-isolator-superconductor (SIS) mixers and bolometers, have been invented to extend the useable window.

Instead of mirrors and lens, in the radio frequency region we use antennas to collect signals from space.

A diversity of antennas have been designed to observe astronomical objects at various radio wavelengths. At millimeter to submillimeter wavelengths, parabolic dishes are generally used for radio telescopes to detect faint radio sources. The most important performance of an antenna is antenna sensitivity. With a higher sensitivity antenna, astronomers can detect and study more astronomical objects. The sensitivity of a parabolic dish is determined by its size or collecting area. Thus, researchers tend to build large dishes for radio telescopes. However, the construction of giant dishes is costly and time consuming. It has been a great challenge for engineers and scientists to build such huge instruments even in modern times (e.g. Gawronkski 2007). To maintain a large collecting area, instead of building a single large dish, researchers divide it into a number of small dishes. Such multi-antenna design can ease the difficulty of antenna structural engineering, which therefore becomes appealing and feasible for radio telescopes with large collecting areas.

Multiple antennas, an antenna array, can be operated to detect astronomical objects in two modes. In the first mode, we can simply combine the signals of the antennas to increase the signal-to-noise ratio (SNR) of data. The total antenna collecting area is that the number of the antennas times the antenna size. However, the combined beam size is exactly the same as the beam size of the antenna. In the second mode, the signals can have artificial delays to synthesize an interference beam pattern, a synthesized array pattern. The array pattern is a multilobe pattern that consists of a mainlobe and many sidelobes. Here the mainlobe is the lobe in the pointing direction of the array. This mainlobe is also called the synthesized beam size. The synthesized beam is normally smaller than the antenna beam and provides higher mapping resolution. The distances between antennas are baselines, which mainly decide the mapping resolution. This multi-antenna design is generally called an interferometer.

The phase coherence between antennas is not critical to data quality in the first mode. However, in the second mode, phase incoherence can significantly degrade the data. If the phase incoherence is up to 180°, the signal is completely diminished. Under normal weather conditions, the atmosphere opacity fluctuation at millimeter and submillimeter wavelengths in several hours is generally a few $\pm 10\%$ but the phase fluctuation can be a few $\pm 10\%$ to 100% of 2π. Thus, the phase fluctuation is one the most critical issue for radio interferometers.

In the following section, we introduce the Combined Array for Research in Millimeter-wave Astronomy (CARMA), which is the combination of the former the Berkeley Illinois Maryland Association (BIMA) array and the Owens Valley Radio Observatory (OVRO) millimeter-wavelength array.

Figure 3.1 The BIMA array.

3.2 CARMA

In 2004, construction began on the new CARMA project (Woody et al. 2004) by moving the BIMA and OVRO millimeter-wavelength antennas to the CARMA site. The site, Cedar Flat in eastern California, is at 7200 feet elevation, which significantly reduces the effect of atmospheric decorrelation. In the following subsections, we introduce the BIMA and OVRO arrays in technical details first. Then, we describe the current performance and status of CARMA.

3.2.1 BIMA and OVRO Arrays

BIMA (Figure 3.1) was a consortium consisting of University of California at Berkeley, University of Illinois at Urbana-Champaign and University of Maryland, College Park. The BIMA interferometer was at Hat Creek, California, before it was moved to the CARMA site. It consisted of ten 6-m dish antennas and $\lambda = 3$ and 1 mm cooled receivers that could observe at 75-115 and 210-270 GHz. The bandwidth of the IF (intermediate frequency) was 830 MHz while the correlator could be set to 200, 100, 50, 25, 12.5 and 6.25 MHz bands; the narrower bandwidth mode the higher spectral resolution. There were four configurations, A, B, C and D, corresponding to synthesized beams of about $0\farcs5$, $2''$, $5''$and $17''$at $\lambda = 3$ mm, respectively.

The OVRO (Figure 3.2) millimeter-wavelength array founded by California Institute of Technology, consisted of six 10.4-m dish antennas and $\lambda = 3$ and 1 mm cooled receivers at 80-115 and 210-270 GHz. The

Figure 3.2 The OVRO millimeter-wavelength array.

site was at Big Pine, California at 4000 feet height. The overall bandwidth of the IF amplifier and correlator was 1 GHz. There were five configurations, compact (C), low (L) equatorial (E), high (H) and ultra-high (U). The angular resolutions of configuration C, L and L+H are 10″, 5″and 2″at $\lambda = 3$ mm, respectively, where L+H is a mixed configuration.

3.2.2 Current CARMA Status

Combining the BIMA and OVRO dishes, the collecting area of CARMA (Figure 3.3) is about 725 m^2, which increases the observing efficiency by 50%-100%, compared to the BIMA or OVRO arrays. Currently, CARMA has four configurations, B, C, D, and E corresponding to 0.″8, 2″, 5″and 10″at $\lambda = 3$ mm, respectively. The number of baselines is 105, and the longest baseline is 1 km in the B configuration. Much of the original CARMA hardware and software has been upgraded during the integration of CARMA. The new 3 mm and 1 mm receivers can operate at 85-116 and 215-270 GHz. The total IF bandwidth to the correlator is 4 GHz. The current correlator has six windows or three bands (Hawkins et al. 2004). The widest bandwidth mode is the 500 MHz band. The highest spectral resolution is 30.5 kHz/channel with 2 MHz bandwidth. An 8-hour track with six 500 MHz bands can reach to of approximately the sensitivity of 0.5 mJy/beam at $\lambda = 3$ mm.

With a better site, new receivers and correlators, the CARMA is indeed a powerful tool for astronomers to explore star forming regions, molecular clouds, galaxies and other astronomical objects if the atmosphere conditions are in favor. Unfortunately, even with such great improvement, CARMA still sometimes suffers

Figure 3.3 CARMA.

from atmospheric fluctuations. In 2007 winter, we just went through the worst winter observing weather ever. Only a few days of 1 mm weather were available, and the observation efficiency seriously plummeted. Better phase correction techniques to increase the efficiency become urgent. Before we seek a better phase correction technique, we need to understand how phase fluctuations affect interferometric observations and what water vapor radiometers can do to solve this problem.

3.3 Phase Incoherence Impact

An astronomical signal goes through the atmosphere before it reaches an antenna. Then, the signal passes a receiver, with amplifiers, mixers and filters, to a correlator. Finally, the correlator processes the signal and the output is stored as observational data. The atmosphere, dish, receiver and correlator can produce noise and affect the observational data. Based on observational experience and instrumental measurements, the dish, receiver and correlator are more likely to be stable compared with the atmosphere. Therefore, the quickly varying data noise is mostly contributed by the atmosphere.

The data sets from antennas are convolved by the correlator. The convolution of two data sets is

$$r_{ij}(\tau) = r_i * r_j = \int r_i(t) r_j(\tau - t) dt, \tag{3.1}$$

where r_i and r_j are the data sets, r_{ij} is the cross correlation function, t is time, $*$ is the convolution operator, and τ is a variable of the shifted phase between two data sets. τ can be considered as a displacement on a source image. In interferometry, phase shifting usually implies a delay in terms of time or a displacement in terms of space. The data sets are normally two dimensional data i.e. the signal is sampled by two orthogonal signals, such as *sin* and *cos* functions. A data point consists of two data values at the same time. So astronomers can adjust the phase of the data points by changing the two values during data reduction. Since the data sets are two dimensional, all functions in Equation 3.1 are complex functions and so is the embedded noise.

The complex noise function can be considered as amplitude noise and phase noise. The amplitude noise is caused by the change of the atmospheric opacity while the phase noise is caused by the fluctuation of the refraction index of the atmosphere, which varies the path delay of astronomical signal to an antenna dish. Interferometric data quality is basically dominated by such phase noise. To show how the phase noise affects the data quality, we simulate the relationship between a coherence factor and the phase noise. The coherence factor is defined as the receiving power ratio of partially coherent waves to perfectly coherent waves. In this simulation, we use the MIRIAD task, `uvgen`, to generate observational data with a given phase noise level. The simulation basically demonstrates a constructive and destructive wave experiment by varying the phases of combining waves. For example, two $sin(kx)$ waves produce a constructive wave $2sin(kx)$ with a doubled amplitude. However, if one of these waves has been phase shifted to $-sin(kx)$ by 180°, the combined wave in the direction of k is completely destructive. We used 1000 waves to conduct the simulation. The large number of the waves is to minimize the sampling effect by a limited number of samples.

Figure 3.4 shows the coherence factor versus the phase noise rms. The blue line is the simulated result of `uvgen` with an uniform noise model. The red line is the theoretically calculated coherence factor with a Gaussian noise model. In this simulation, we assume that atmospheric absorption is not involved, i.e. the opacity of the atmosphere is constant. When the phase noise rms is 0°, the waves are perfectly coherent and the coherence factor is 100%. On the other hand, when the phase noise rms is 103.9°, the waves are completely incoherent and the coherent factor is 0. Based on Figure 3.4, one can determine how the observational data is degraded by the atmospheric phase fluctuation. When the phase noise rms is 50°, the astronomical signal strength is lowered to a half. If the phase noise rms is increased to 75°, only a tenth of the strength remains. The task `uvgen` uses an uniform noise model to produce observational data. We add the theoretical prediction from a Gaussian noise model in Figure 3.4 to compare with the simulation. The two noise models do not qualitatively show a great differentiation.

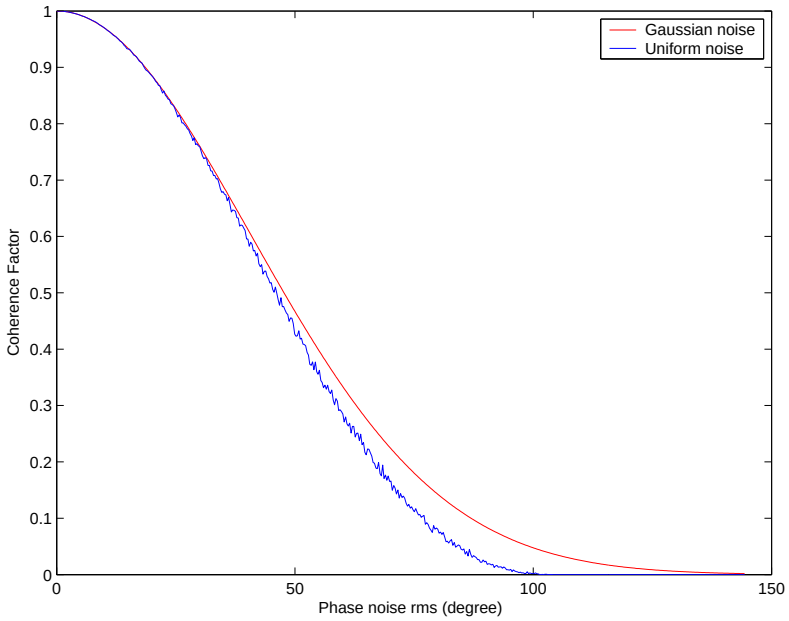

Figure 3.4 Coherence factor versus phase noise.

The simulated spectra in Figure 3.5, demonstrates the severe impact of the additional atmospheric phase noise on weak spectral line observations, such as large molecule surveys. Setting an overall system noise of 0.16 Jy, we simulate observations of a 2 Jy spectral line at 100 GHz with a 1 Jy continuum. In the case of 65° phase noise rms in Figure 3.5(a), the strength of both the spectral line and the continuum drop below the noise power, and a non-detection results. If a phase correction system can lower the phase noise rms to 36°, in Figure 3.5(b), the detection of the spectral line is enormously improved to 3σ and a detection occurs.

Comparing the spectra with different noise levels in Figure 3.5, we conclude that the phase noise is indeed critical to interferometric data quality. Generally, observing phase calibrators such as quasars every 20-30 minutes, can only recover atmospheric phase fluctuation on the time scales of 1 hour. To correct phase fluctuations for CARMA on shorter time scales, a new phase correction system is required. To lower the effect of the phase noise, the "twinkling" of path delays, the new phase correction system must recover the extra path delays in seconds. As mentioned before, the varied path delays are due to the fluctuation of the refraction index of the atmosphere. Water vapor is the major component in the atmosphere that alters the refraction index (Waters 1976). To overcome the water vapor effect, we have explore tropospheric water vapor with numerical simulations and site observations.

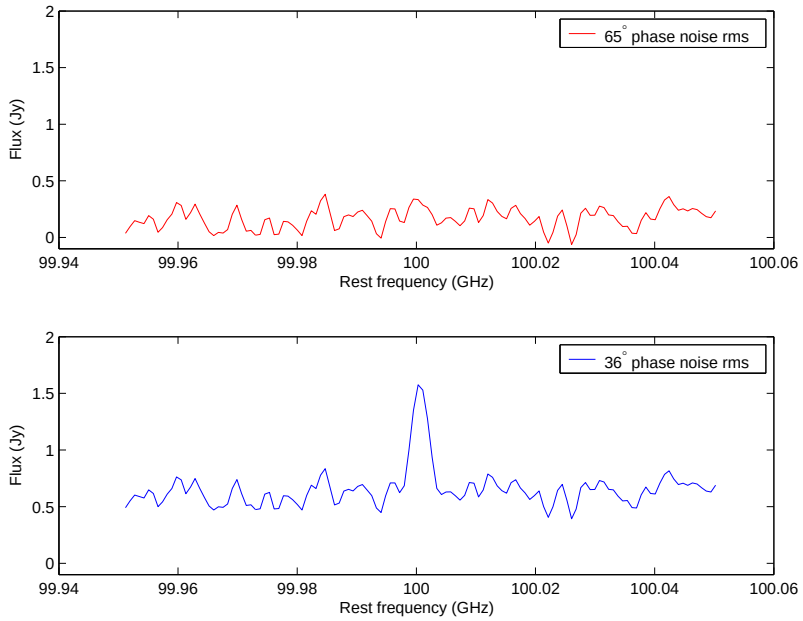

Figure 3.5 (a) The spectrum on the top shows a 100 GHz spectral line with 65° rms of the phase noise. (b) The spectrum on the bottom is improved by lowering the rms to 36° and a 3σ detection occurs.

3.4 Atmospheric Models

The atmosphere contains many molecules in gas, liquid and sometimes even solid phases. Normally we classify the gas phase molecules as dry components and the water vapor. Compared with the dry components in the atmosphere, like oxygen (O_2), nitrogen (N_2) and carbon dioxide (CO_2), the water vapor affects the refraction index of the atmosphere and distorts the wavefronts of astronomical radio signals the most (Waters 1976; Thompson et al. 2001). According to laboratory experiments, the path delay variation L_w of the atmosphere can be obtained by using the following equation (Thompson et al. 2001)

$$L_w(\rho_w, T)(\mu\text{m}) = 0.299 \times PWV(\text{mm}) + 1742.2 \times 10^{-6} \int_{ground}^{\infty} \frac{\rho_w(s)(\text{kg cm}^{-3})}{T(s)(\text{K})} ds, \tag{3.2}$$

where s is the height above the ground, $T(s)$ is the temperature function, $\rho_w(s)$ is the water vapor density function, and PWV is the precipitable water vapor. The second term on the right-hand side is an integral from the ground to infinite height. As long as $\rho_w(s)$ and $T(s)$ are known, one can determine the path delay of each antenna and apply phase correction with the differences of path delays.

To use Equation (3.2) to calculate the path delays, one needs an atmospheric model to describe the distributions of the water vapor temperature $T(s)$ and density $\rho_w(s)$. The simplest model uses exponential functions with scale heights to describe the temperature, pressure, and water vapor density in the atmosphere.

Table 3.1. Cedar Flats Atmospheric Opacity

Percent of Time	Estimated τ_{225} Opacity	Estimated PWV (mm)
90%	0.53	12
50%	0.26	5
25%	0.2	4.5
10%	0.14	3
5%	0.12	2

For example, the temperature can be described as

$$T(s) = T(0) \times e^{-\frac{s}{h_T}}, \tag{3.3}$$

where h_T is the scale height of the temperature function. Besides the simplest model, United States 76 (US76) is the standard model adopted by industries and governments, which consists of piece-wise functions to fit the long time atmospheric measurements. Generally, it is more accurate, however, the functions are not analytical so the model can only be used numerically. Another technique is to use radiosonde data collected by weather balloons every few hours, which is the most exact but not realistic for full-time measurements.

The CARMA site is at Cedar Flat, California, with an altitude of 7200 feet. Based on the long-term observations at 225 GHz, the radiometer data shows that the precipitable water vapor (PWV) at the CARMA site is less than 5 mm 50% of the time. Table 3.1 summarizes the probabilities of the estimated opacities and corresponding PWVs at the site.

Given the estimated PWVs, we have used the atmospheric modeling in the MIRIAD `ATM` code to simulate the atmospheric emission at the CARMA site. The `ATM` code developed by University of Maryland and University of California, Berkeley, models the atmospheric emission with given atmospheric models and physical conditions, like extra water vapor layers. One can easily obtain the atmospheric opacity and sensitivities by inputting the physical parameters. In our atmospheric simulations, three atmospheric models do not show perceptible differentiation in the spectra. Figure 3.6 shows the atmospheric emission and sensitivity from 10-500 GHz with different PWVs. We can clearly see several strong emission lines in Figure 3.6(a) at about 60, 118 and 183 GHz. The 60 and 118 GHz lines are oxygen emission while a small bump at 22 GHz and the huge bump at 183 GHz are water vapor emission. Figure 3.6(b) shows the sensitivity of the atmospheric emission to extra water vapor clouds. The sensitivities are calculated by adding an extra water vapor layer with 50 μm delay in the model and measuring the change of the atmospheric emission. It indicates what frequency is sensitive to extra water vapor, which causes extra path delay. The 183 and 325

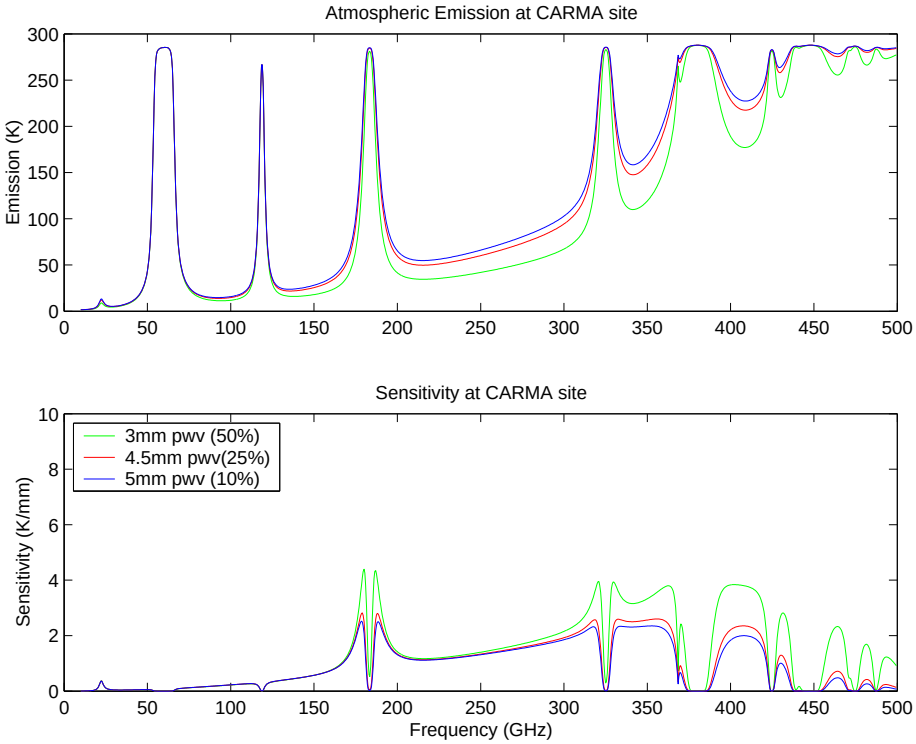

Figure 3.6 The spectra on the top show the simulated atmospheric emission with 3, 4.5 and 5 mm PWVs. The plot on the bottom show the spectral sensitivities. The sensitivities are calculated by adding an extra water vapor layer with 50 μm delay in the model and measuring the change of the atmospheric emission.

GHz water vapor lines create a relatively flat zone at 200-300 GHz.

3.4.1 Water Vapor Lines

There are two well-known water vapor lines in the millimeter region, at 22 and 183 GHz. The 22 GHz water vapor line is the $6_{16} - 5_{23}$ rotational transition while the 183 GHz line is the $3_{13} - 2_{20}$ transition. H_2O is an asymmetric top molecule, which requires K_a and K_c quantum numbers. The two digits in subscript are K_a and K_c. The 22 GHz water line is relatively weak but the 183 GHz line is very bright. Here, we re-examine the sensitivities of both lines. Figure 3.7 shows that with a 50 μm delay water vapor layer the peak of the 22 GHz line changes less than 2 mK when the PWV varies from 2 to 5 mm. The sensitivity of the 22 GHz water vapor line to extra delay water vapor seems to be constant regardless of PWV. Therefore, a simple scale factor in unit of (μm/mK) can directly convert the atmospheric emission to extra path delay. The 183 GHz line saturates when the PWV is greater than 2 mm as shown in Figure 3.8. However, the wings of the 183 GHz line may be a good indicator for the amount of an extra path delay by water vapor radiometers. However, there is no such simple scale factor for the wings to be converted into a path delay. Computational

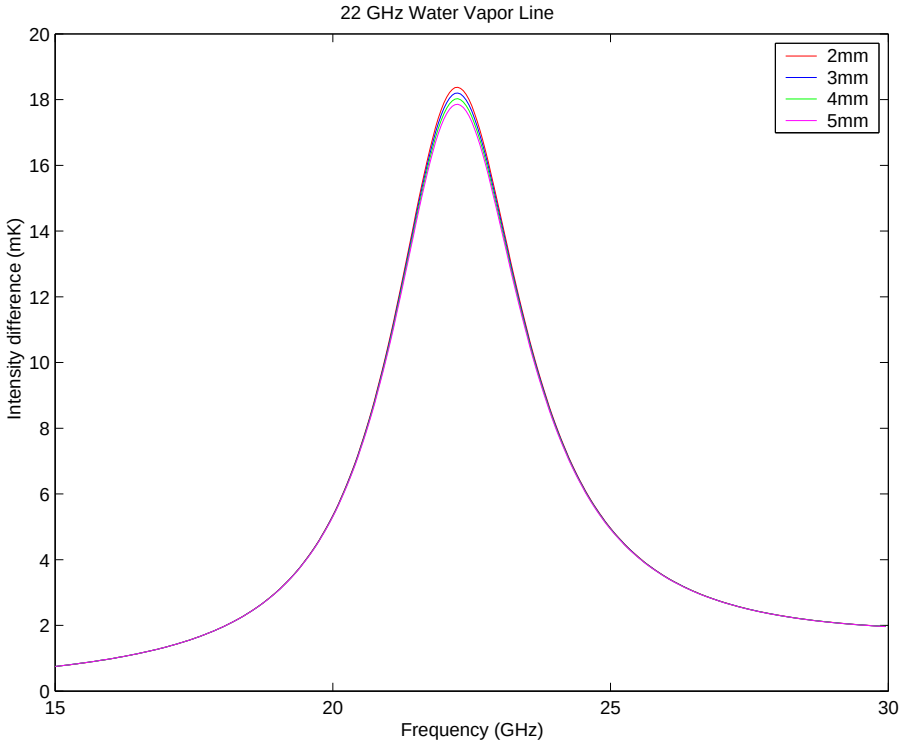

Figure 3.7 22 GHz water vapor line with 50 μm delay water vapor and 2, 3, 4 and 5 mm PWVs.

iteration is needed to determine the delay by fitting the spectra of the wings. Therefore, considering the CARMA site condition, the 22 GHz may be a better option to indicate the path delays.

3.5 Water Vapor Radiometers

Since water vapor turbulence causes the path delay or phase fluctuations and the amount of the water vapor can be measured by radiometers, Zivanovic (1992) suggested that by monitoring the water vapor in the atmosphere along the lines of sight of antennas, water vapor radiometers (WVRs) may provide sufficient information to recover the phase fluctuations from every few seconds to minutes. Therefore, the WVR phase correction system may be an alternative to better correct phase fluctuations.

Based on this premise, WVR systems, including 22 GHz and 183 GHz receivers, have been built and tested by many radio interferometer associations, such as OVRO (Marvel & Woody 1998), BIMA (Staguhn et al. 1998), the Very Large Array (VLA) (Chandler et al. 2004), the Institute for Radio Astronomy at Millimeter wavelengths (IRAM) (Bremer, Guilloteau & Lucas 1995), the Submillimeter Array (SMA) (Wiedner et al. 2001), and the eventual Atacama Large Millimeter Array (ALMA) (Hills & Richer 2000).

In the following sections, we particularly introduce the BIMA WVRs and OVRO water line monitors

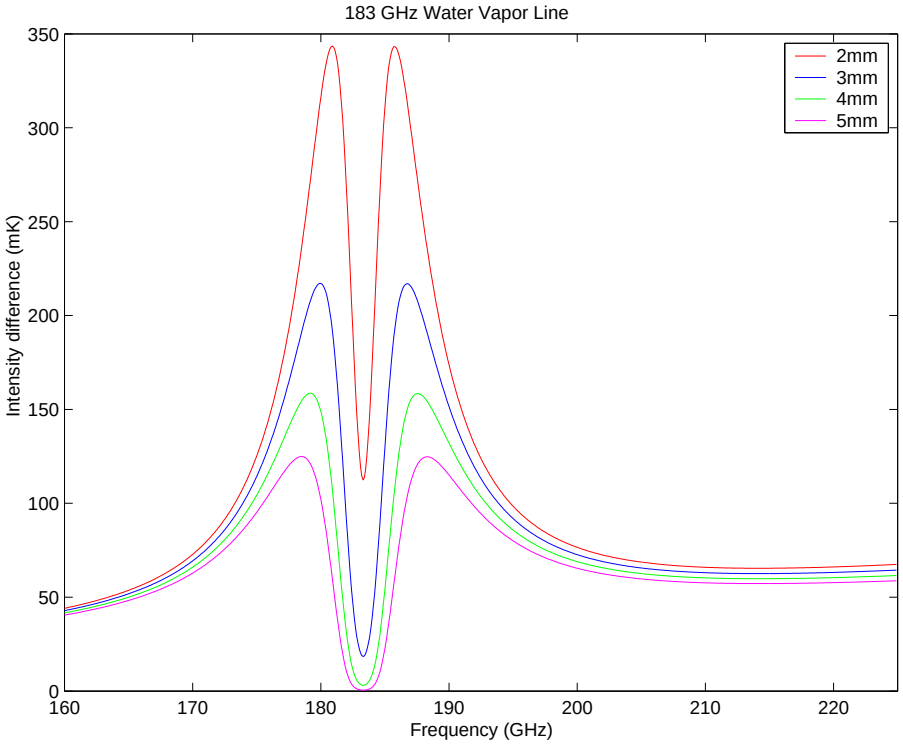

Figure 3.8 183 GHz water vapor line with 50 μm delay water vapor and 2, 3, 4 and 5 mm PWVs.

(WLMs).

3.6 BIMA Water Vapor Radiometers

Millimeter wave continuum radiometry at BIMA using total power receivers (Staguhn et al. 1998) was successful only under certain atmospheric conditions. Analysis of the data showed that only in clear weather was there any correlation between the atmospheric phase fluctuations and the total power measurements (Wright 1996). During those times, the phase correction was successful only about 50% of the time.

At BIMA in April 1999, similar 22 GHz water line radiometry experiments were performed on three BIMA antennas (Wright 2000) with two types of backends: a one channel swept frequency system and a 16 channel 4 GHz bandwidth autocorrelator spectrometer (the Atmospheric Phase Inference Device, or APHID (Harris 2000)). These tests also showed that about 50% of the time the interferometry data were improved. Unfortunately in the other 50% of the data, drifts in the measurement degraded the rms phase. An atmosphere scale factor was used instead of an atmospheric model. From this work, it was quickly realized that one of the limiting factors was the gain fluctuation in the system that was degrading the data.

To develop a more stable WVR, the BIMA researchers decided to build a correlation receiver at 22

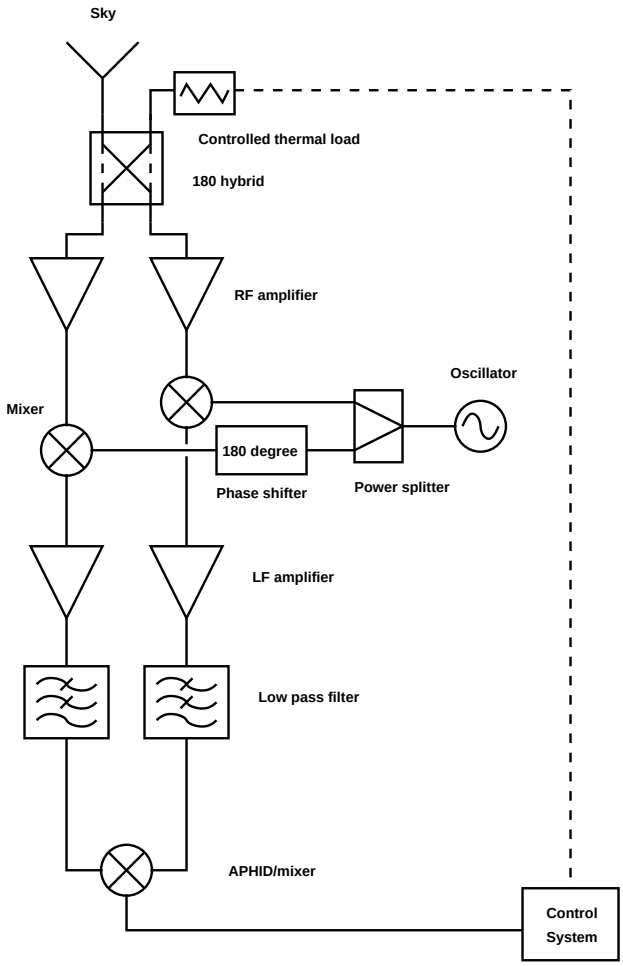

Figure 3.9 The system block diagram of the BIMA WVRs.

GHz that will provide the most stable system for phase correction experiments. As shown in Fig. 3.9, the system involves a 180° hybrid, RF amplifiers, mixers and low pass filters for two channels. The two channel signals are compared with a low frequency mixer and read-out by a control system. The gain calibration and signal detection are processed simultaneously. A controlled thermal load (CTL), like a noise-adding receiver system, is added in the system to calibrate the gains; however, due to the 180° hybrid, water vapor signal and the CTL signal both go through the same signal path to the comparator. Thus, by tuning the power of CTL to minimize the comparator output, one measures the temperature difference between the sky and a cryogenically cooled reference load. Errors due to amplifier gain fluctuations, which mimic water vapor fluctuations, are significantly decreased by regulating the load temperature to track the sky temperature. However, the receiver was not finished before the BIMA array is merged with the OVRO millimeter-wavelength array.

3.7 OVRO Water Line Monitors

At OVRO, WVRs were installed in 1999 (Marvel & Woody 1998) with cryogenic cooled, low-noise 18-26 GHz, InP amplifiers Fig. 3.10. These receivers were an upgrade to previous less sensitive uncooled systems. Basically, the OVRO WVRs are total-power systems with double side-band receivers, which is a simple and robust design. As shown in Fig. 3.10, the receiver includes radio frequency (RF) amplifiers, band pass filters, power combiners/splitters, and detectors. The water vapor emission power goes into the horn antenna and is amplified by the RF amplifier. The horn is driven by a motor so it can observe sources from different directions: sky, hot load, or cold load. The band pass filter behind the RF amplifier is designed with 18-26 GHz pass band so the water vapor signal can go through the mixer without interference from other frequency signals. The mixer shifts the signal to a lower frequency band. An intermediate frequency (IF) filter and IF amplifiers can increase the magnitude of the signal again.

There are three output bands in the power splitter, 4 to 6 GHz, 7 to 9 GHz and 10 to 12 GHz. They are filtered separately by band-pass filters and later combined by power combiners. To decrease mis-match effects between different channels, two switches are installed. Finally, the signals are amplified and converted to low frequency signals by diode detectors. After the signals come out of the WVR, the data are sampled. The sensitivity needed for detecting water vapor suffers from fluctuations in system gain, offset, bandwidth and noise temperature. To stabilize the WVRs, constant calibration of these parameters is done by observing calibrators, the hot load and the cold load.

By analyzing the last few years of data, the residual delay errors of 100-200 μm are obtained under some

conditions by cross-calibrating the temperature scales of the WVRs and linking the delay phase of the target source to that of a phase calibrator at a different elevation. Point source observations show that high quality images can be extracted from previously unusable data when the corrections are applied.

However, the general result is that the WVRs increase phase coherence less than 50% of the time. Although the accurate measurement of the relative gains and offsets of the InP amplifiers is the most critical and difficult step in the this phase correction approach, the simplified conversion factor may play a large role as well. The results gathered to date suggest that using a simple constant conversion factor to infer the phase correction from the 22.2 GHz line intensity does not work consistently and that there may be further atmospheric physics at play. As illustrated in Fig. 3.11, there is a trend that the worse the initial phase coherence the more likely the phase coherence will be improved by the assumption of a constant atmospheric conversion factor. The problem is that during median weather, when the phase correction should also be improving the observations, the water vapor emission does not well track the phase fluctuations. So although the coherence is often increased by tracking the atmospheric water vapor, we need to make the system more reliable.

3.8 CARMA Water Vapor Radiometer Project

Many WVR projects have been carried out, however, these projects seem to encounter unknown difficulties and only occasionally show correlations between the water vapor data and observed path delays (e.g. Chandler et al. 2004; Wiedner et al. 2001). We started a water vapor project for CARMA in 2006 to carefully re-examine the WVR phase correction technique and attempt to seek any explanations.

During the early stages of CARMA, we have used the existing OVRO WLMs to systematically investigate both the instrument stability and the atmospheric properties at the CARMA site, e.g., what correlations with atmospheric conditions will emerge? Are we missing any atmospheric physics? We have tested the OVRO WLMs in a window lab test as shown in Figure 3.12. We set up one dewar cooled and the other warm. The result in Figure 3.13 shows that two WLMs have consistency to some degree. However, the difference between two WVRs is considerably high. Moreover, the cooled WLM is very unstable. The gain fluctuation is enormous when the temperature is not properly regulated.

We conclude that the system stabilities, including system temperature, system gain and receiver temperature, are crucial to the WVRs. Thus, the receiver temperatures need to be regulated. The system temperature and gain need to be measured accurately so the gain fluctuation can be calibrated. Before we can further investigate why the WVR phase correction is unreliable, we need to build WVR prototypes with

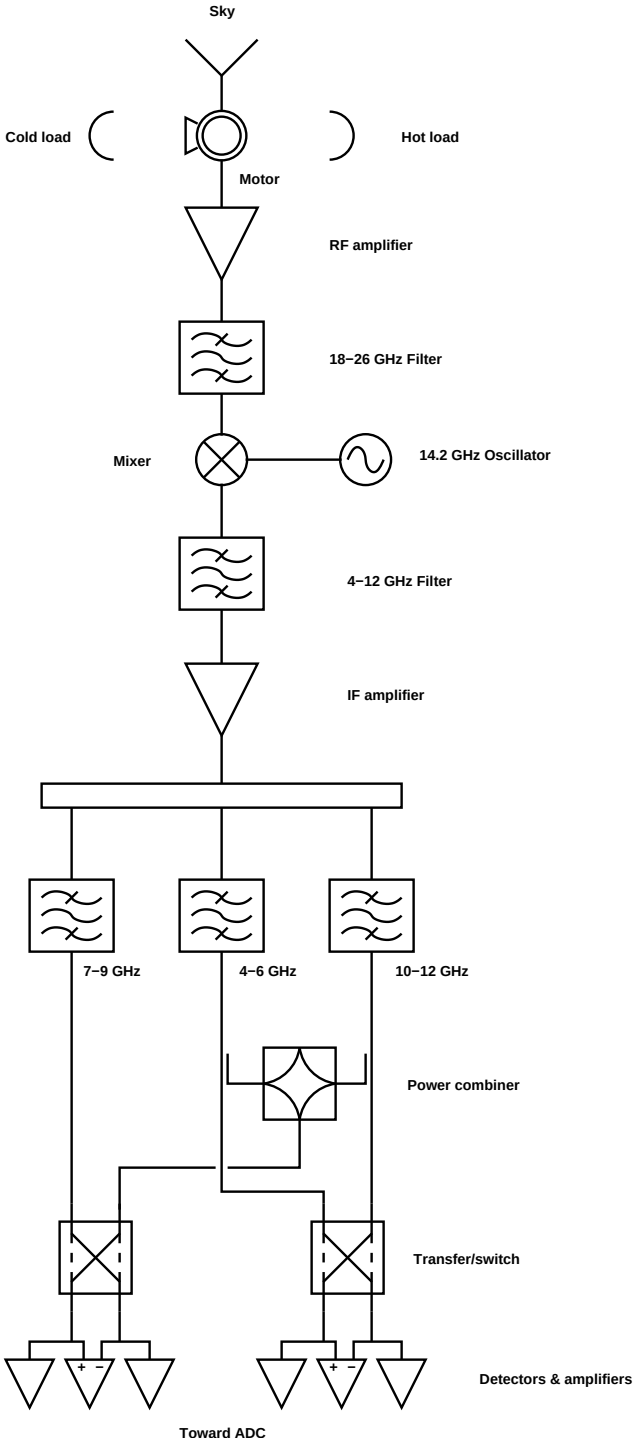

Figure 3.10 The system block diagram of the OVRO WVRs.

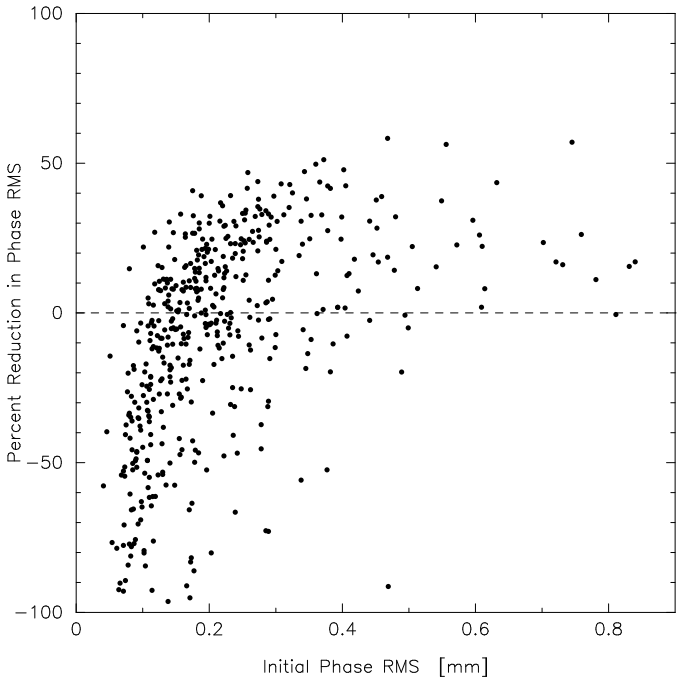

Figure 3.11 Phase rms before versus after the OVRO WLM phase correction. When the initial phase rms is higher than 200 μm, the WLMs improved the rms. However, when the initial phase rms is lower, the WLMs worsen the rms.

better performance.

3.9 Summary

We have shown the impact of phase incoherence on interferometric data quality. Since water vapor turbulence is the major factor to cause the phase incoherence, water vapor radiometers may provide a good phase correction technique. The 22 GHz and 183 GHz water vapor lines have been used to test water vapor phase correction by many interferometer associations. However, the results remain unsatisfactory to date.

We have simulated the atmospheric emission at the CARMA site with the MIRIAD `ATM` code to explore the water vapor condition. While the 183 GHz water vapor line saturates and 183 GHz receivers are costly, the 22 GHz water line is more suitable for CARMA to develop water vapor radiometers. The simulation also indicates a simple scale factor may exist for the 22 GHz line, which can be used to directly convert the line brightness temperature to a path delay.

After examining the OVRO water line monitors (WLMs), we decided to redesign and upgrade the WLMs into WVR prototypes for CARMA to systematically test the water vapor phase correction technique.

Figure 3.12 OVRO WLMs in the window lab test.

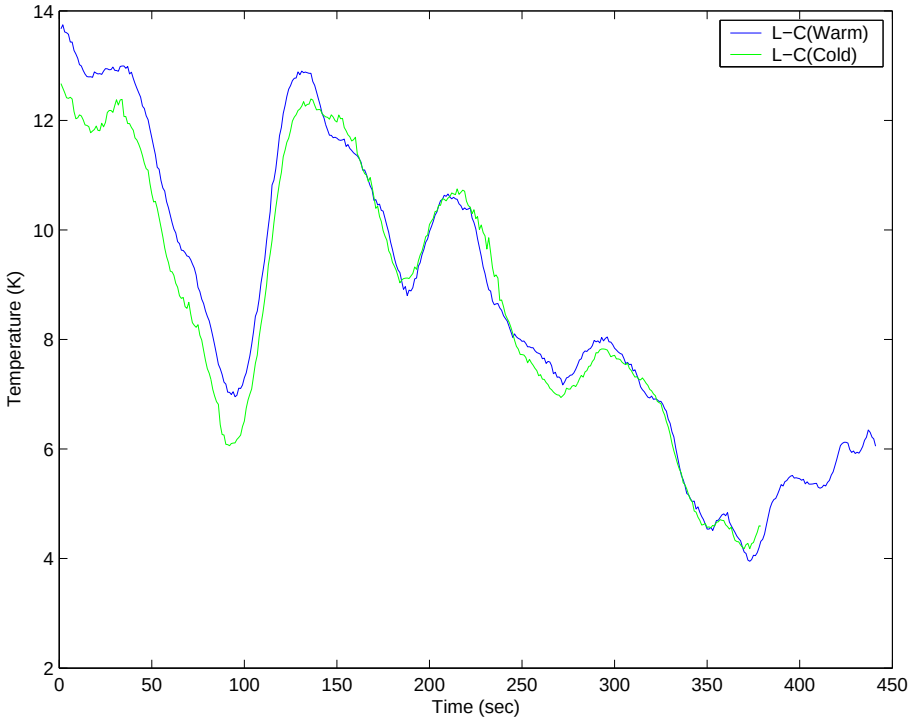

Figure 3.13 OVRO WLM observation at the window lab test. Two tracks from a warm and cooled WLMs show similar but not exact patterns in this 7.5 minutes. With their huge beam (49°), the two WLMs should almost detect the same part of the sky and the patterns should be nearly the same.

Chapter 4

Exploring Antenna Power Patterns

In this chapter, we discuss the antenna power patterns of the CARMA 10-m dishes. Without considering the tapers on the secondary mirrors, we show that the antenna beams do not exactly overlay with the water vapor column along the line of sight of the antennas. This geometric difference may causes deviation of path delays derived from the water vapor radiometer (WVR) data. We have conducted numerical simulations to address this problem and quantitatively demonstrated that the water vapor detection efficiency significantly depends on the sizes and heights of water vapor clouds. The water vapor detection efficiency is an efficiency that determines the difference between the water vapor emission temperature and antenna temperature. We suggest that this varied efficiency may play a key role in the WVR phase correction technique and explain that the well-known scale factor of the 22 GHz water vapor line varies in many WVR experiments (Shiao et al. 2006; Shiao, Looney, & Sutton 2008).

4.1 Introduction

Water vapor radiometers (WVRs) are designed to compensate atmospheric phase fluctuations at millimeter and submillimeter wavelengths for radio interferometers on short time-scales. Water vapor has been considered the main component that causes phase fluctuation (Waters 1976). Thus, monitoring water vapor along the lines of sight of antennas and deriving path delay differences of the two antennas on a baseline should allow us to implement a phase correction scheme. However, ground-based antennas are surrounded by water vapor clouds at various heights. The mechanism of detecting such water vapor clouds along the lines of sight of antennas may be very different from that of detecting the astronomical sources.

The atmospheric water vapor turbulence consists of water vapor clouds in various sizes. The path delays are varied by the water vapor clouds in the columns along the lines of sight of antennas to astronomical sources. The clouds are in both the near- and far-field regions of the antennas unlike astronomical sources which are only in the far-field region. Indeed, water vapor is predominantly at the ground, which is in the near-field region. However, the various size of the clouds in the columns may fail to exactly cover the

antenna beams. Thus, the antenna temperatures and the brightness temperatures of the water vapor clouds are no longer the same. Without the information about the sizes and the heights of the clouds, the difference between these two temperatures may cause a problem in deriving the path delays. Moreover, the antenna temperature responds to both the water vapor clouds inside and outside the antenna column. The correlation between the antenna temperature and path delays may be negative under certain circumstances.

To quantitatively demonstrate this effect, we explore the power patterns of the CARMA antennas with numerical simulations to determine the detection efficiency of atmospheric water vapor. The detection efficiency is defined as a ratio of antenna temperature to the brightness temperature of a given water vapor cloud.

4.1.1 Atmospheric Model Review

Here, we use a set of functions in terms of the height h to describe the physical conditions of the atmosphere, like temperature, density and pressure. The atmosphere is considered as an infinite number of layers. For example, the atmospheric brightness temperature is generally written as

$$T_a = \int_0^\infty T_b(h)dh = \int_0^\infty T(h)(1 - e^{-\tau(h)}) \times e^{-\tau'(h)}dh, \tag{4.1}$$

where $T(h)$ is the brightness temperature at h, $T_b(h)$ is the corresponding observed brightness temperature from the ground, T_a is the antenna temperature, and τ and τ' are the opacity of the dh thickness layer at h and the total opacity from the ground to h, respectively (Thompson et al. 2001). This model is simple but gives a good estimate of long time-scale atmospheric conditions.

This model assumes the atmospheric layers fully cover the antenna beam so that the antenna temperature is equal to the brightness temperature $T(h)$. Thus, the antenna temperature can be calculated without considering the direction and the size of the layers. In the case of the WVR phase correction, most researchers use Equation 4.1 to derive the relationship between water vapor temperature and the amount of path delay (e.g. Pardo, Cernicharo, & Serabyn 2001). However, the antenna temperature does not completely reflect the water vapor brightness temperature. Therefore, the equation may overestimate the antenna temperature.

In practice, water vapor clouds are finite-size. Like beam dilution, the antenna temperature is actually lower than the true brightness temperature of the clouds. Moreover, the geometry of the antenna beam in the near field is quite different from that in the far field, which can not be explained simply by beam dilution. Thus, the mechanism of detecting water vapor clouds is more complicated than the models expected.

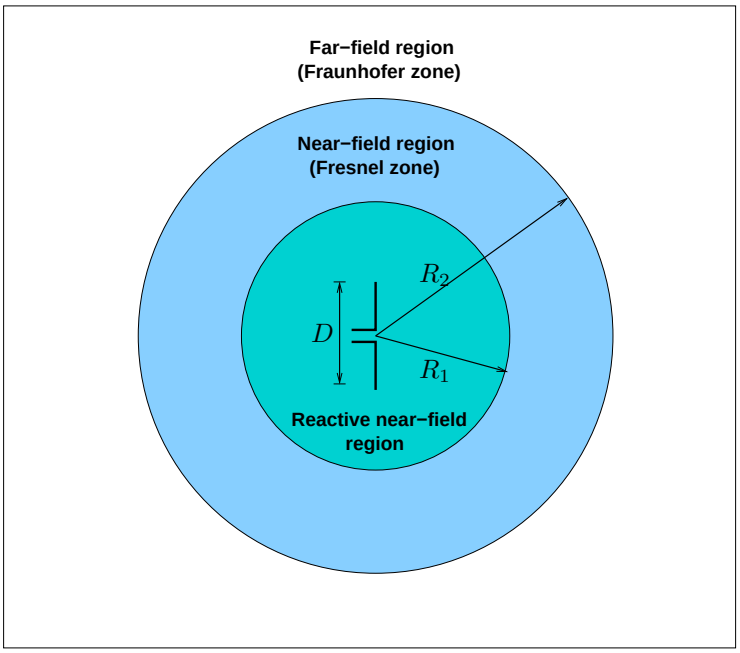

Figure 4.1 The antenna field, including the far-, near- and reactive near-fields, $R_1 = \sqrt{D}/\lambda$ and $R_2 = 2D^2/\lambda$. D is the size of the antenna, 10 m, and λ is the wavelength, 1 cm so R_1 is 200 m and R_2 is 20 km.

4.1.2 Near-field and Far-field

For ground-based antennas, tropospheric water vapor is in the both near and far-fields. Here we review the antenna field at various distances. The antenna field can be divided into three different regions, the far-field, the near-field and the reactive near-field regions as shown in Figure 4.1 (e.g. Balanis et al. 1996). For ground-based telescopes, atmospheric water vapor surrounds antennas. Most water vapor is in the near-field and reactive near-field regions. So the near-field and the reactive near-field water vapor is more important to WVRs. However, considering the amount of water vapor, we can ignore the effect of water vapor in the reactive near-field, which likely contributes less than the others. Water vapor in near-field regions seems more critical to the WVR phase correction. Thus, to further understand the detection of tropospheric water vapor, we need to investigate the near-field antenna patterns.

4.1.3 Antenna Power Patterns

Water vapor clouds are finite-size in both the near- and far-field regions. Therefore, we need to quantify the impact of the finite-size clouds on the water vapor detection efficiency, which is essential to deriving path delays. The investigation of the detection efficiency of the water vapor in the near and far field regions is carried out with numerical simulations. First, we need to generate the antenna power patterns to obtain the

sensitivity of an antenna in terms of direction and distance. Then, the antenna patterns can be considered as two dimensional cross views of three dimensional beams.

Besides the numerical simulations, Gaussian beam analysis is a well-known mathematical tool to analyze near-field problems in the first order. However, to better quantify the impact of the finite-size water vapor clouds, we decide to precisely simulate the patterns instead of an analytic approximation.

The antenna power patterns are usually referred to as the far-field power patterns. In the far-field region, the power patterns are only functions of direction so they generally are written as normalized functions $P_n(\theta, \phi)$ in polar coordinates. In the near-field region, the patterns do not just only depend on direction but also distance. In our simulations, we use the Cartesian coordinate to present the results so that we can illustrate the antenna patterns better in both near and far-field regions.

4.2 Simulation Setup

We simulate a two-dimensionally parabolic antenna receiving radiation power emitted by a group of finite-size sources. By calculating the received power from these sources at different positions, we can produce the plots of the antenna power patterns or beams. The group of sources can be in any kind of geometric shape, a slab or a multi-layer structure, depending on the given cloud models.

We use a two-dimensional antenna instead of a three dimensional in our simulations because three-dimensional simulations consume extensive computing time. We can re-construct the three dimensional results by simply multiplying a factor to each received power data point.

The parabolic antenna is modeled as a linear antenna array in our code. Each antenna represents a small segment of the parabolic antenna. The antenna array is set up along the x-axis, and the finite-size sources are in the first and second quadrants in Figure 4.2. The height of a water vapor cloud is y meter. The size can be controlled by the number of sampled sources. The number of the antenna segments is M and the number of the sampled sources is N, $|\overrightarrow{r_{mn}}|$ is the distance from an antenna segment m to a source n, and Δl is the length of the antenna segments. The electronic field $\overrightarrow{E}$ is perpendicular to the x-y plane.

4.2.1 Electric Field Equation

To obtain the antenna power patterns, we begin with an electric field equation,

$$\overrightarrow{dE(x,y)} = \frac{E_0}{r} e^{-j\overrightarrow{k}\cdot\overrightarrow{r}} dl\hat{z}, \tag{4.2}$$

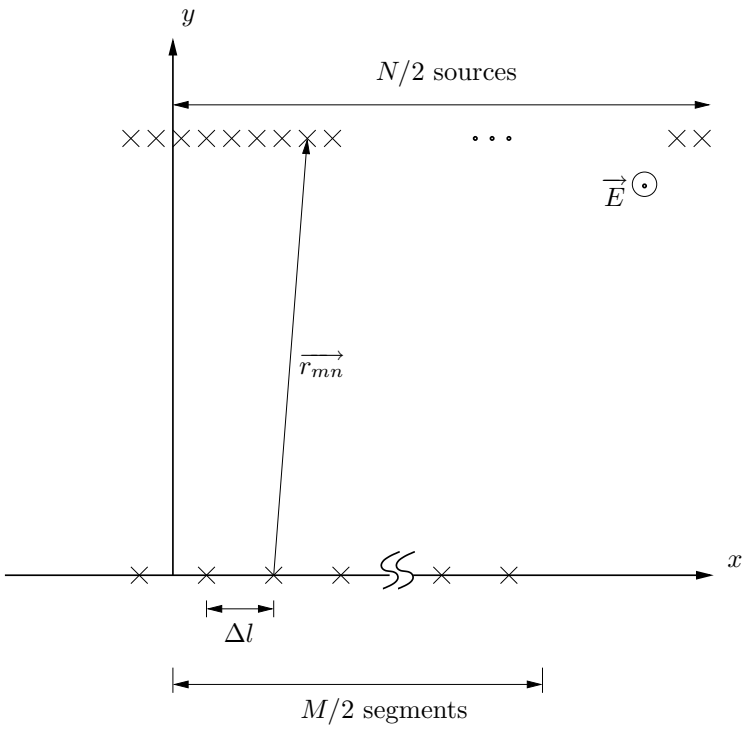

Figure 4.2 Simulation setup.

to describe microwave propagation. Here dl stands for the infinitesimal length of the finite antenna segments along the x-axis, r is the distance from a segment to a source, $\overrightarrow{k}$ is the wave vector and E_0 is the amplitude of the electric waves. The direction of the electric field is toward $\hat{z}$, and all of the electric waves have the same electric field direction so that the total strength of the electric field of the received waves is simply the integral of $\overrightarrow{dE(x,y)}$. The magnitude of the Poynting vector $\left|\overrightarrow{S_{av}}\right|$ is given by

$$\left|\overrightarrow{S_{av}(x,y)}\right| = \frac{1}{2\eta}\left|\int_{-\frac{D}{2}}^{\frac{D}{2}} d\overrightarrow{E}\right|^2, \tag{4.3}$$

where η is the intrinsic impedance of free space. D is the length of the array or the diameter of the parabolic antenna. The procedure to calculate the received power is to obtain $\left|\overrightarrow{S_{av}}\right|$ first, then integrate over the solid angle, Ω, to find $P_{ant}(\Omega)$, the total power transmitted by the group of sources.

$$P_{ant}(\Omega) = \iint_{\Omega} \overrightarrow{S_{av}} \cdot d\overrightarrow{s}, \tag{4.4}$$

where $d\overrightarrow{s}$ is an infinitesimal surface of the source.

4.2.2 Computational Method

Equation (4.2), (4.3) and (4.4) are converted to the following forms so they can be easily processed:

$$\left|\overrightarrow{S_{av}}\right| = \frac{1}{2\eta}\left|\sum_{n}^{N}\frac{e^{-j\overrightarrow{k}\cdot\overrightarrow{r_{mn}}}}{|\overrightarrow{r_{mn}}|}\right|^2 = \frac{1}{2\eta}\left[\left(\sum_{n}^{N}\frac{\cos(k\times r_{mn})}{r_{mn}}\right)^2 + \left(\sum_{n}^{N}\frac{\sin(k\times r_{mn})}{r_{mn}}\right)^2\right]. \tag{4.5}$$

This allow an easy calculation of the magnitude of the Poynting vector from a source n to a segment m on the x-y plane. As shown in Figure 4.2, r_{mn} is the distance from an antenna segment n to a source m. To calculate the power transmitted by a cloud or a group of the finite-size sources to the antenna, the angles θ of $\overrightarrow{r_{mn}}$ must be determined first, which at (x, y) is given by

$$\tan\theta(x,y) = \frac{\sum_{n}^{N}\frac{x_{mn}}{|r_{mn}|^2}}{\sum_{n}^{N}\frac{y_{mn}}{|r_{mn}|^2}}, \tag{4.6}$$

where x_{mn} and y_{mn} are the components of $\overrightarrow{r_{mn}}$ on the x- and y-axes.

$$P(y) = \sum_{m}^{M}\left|\overrightarrow{S_{av}}\right|\Delta x \times \pi y\cos\theta \tag{4.7}$$

gives the transmitting power of the cloud at the height of y to the antenna segments. Δx is the size of the source. To assure the simulation accuracy, the size of the antenna segments, Δl and Δx, must be less than one-tenth wave length, $\lambda/10$.

4.3 Simulation Results and Discussion

4.3.1 Near-Field and Far-Field Patterns

The size of the antenna in our simulations, D, is 10 m, which is from -5 m to 5 m on the x-axis. The wavelength λ is 1 cm, approximately corresponding to the 22 GHz water vapor line. Therefore, the far-field limit in our simulations is $2D^2/\lambda$, 20 km (Balanis et al. 1996). Below 20 km, the power patterns are in the near-field region, Fresnel zone; the power patterns beyond 20 km are in the far-field region, Fraunhofer zone, as shown in Figure 4.1.

In Figure 4.3 (a), the antenna power pattern at 200-m height, a Fresnel pattern is presented, which does not contain side lobes. The Fresnel pattern represents a single-slit diffraction pattern, so it is also

called Fresnel diffraction. The antenna dish can be considered as an aperture that receives microwaves from sources. The power density near 5 m, the edge of the aperture, is nonzero even when it is off the edge of the antenna. Within the edge, the power density oscillates like a sinusoidal function.

When the sampled sources move up to 2 km as in Figure 4.3 (b), sources off the edge share more power density, but the power pattern becomes more concentrated in the center of the aperture. The peaks of the power density appear at the edges of the main lobe. The half maximum power width of the main lobe is smaller than the antenna diameter, which is quite interesting.

In Figure 4.3 (c) and Figure 4.3 (d), the far-field power pattern can be clearly recognized. Comparing the power patterns at 20 km and 40 km, the peak power density reduces to half but the size of the main lobe doubles. This can be explained by energy conservation. The power density decreases as the beam size increases.

By showing the line of the half maximum power density in Figure 4.4, we can depict the antenna beam better to fully understand how the beam evolves in terms of the distance from the antenna. In the far-field region, the antenna beam looks like a cone with a solid angle depending on the antenna size; however, in the near-field region, the antenna beam lacks a simple geometric shape and at some distances the beam is narrow.

4.3.2 The Impact of Finite-size Clouds of Water Vapor

The brightness temperatures of infinite-sized water vapor clouds are the same as the antenna temperatures regardless of their heights. Additionally, according to the ATM simulations (Staguhn et al. 1998), the cloud altitude barely affects the 22 GHz water line. Therefore, for a 22 GHz WVR system, we can derive the path delays without knowing the exact height of water vapor clouds. However, with finite-size clouds, the cloud height and size affect the antenna temperature enormously. In Figure 4.3 (c) and (d), comparing a 20-m wide cloud at 20-km and 40-km height with the same temperature, the detected power from the latter is only half of the former. The path delays caused by the cloud at 20 and 40 km should be similar. Therefore, the antenna temperature may fail to respond to path delay change accordingly. We note that this is not equivalent to the beam filling factor, which decreases much faster.

To further investigate the effect of finite-size water vapor clouds, we compare the brightness temperature and its corresponding antenna temperature with different-size clouds at different heights. The detection efficiency as the ratio of antenna temperature to brightness temperature can be scanned by moving the same cloud from one height to another. In Figure 4.5, we show the detection efficiencies for four clouds of the sizes, 10, 20, 40, 200 m wide. For the 10-m cloud, the antenna temperature reduces to only 90% at 1 km and

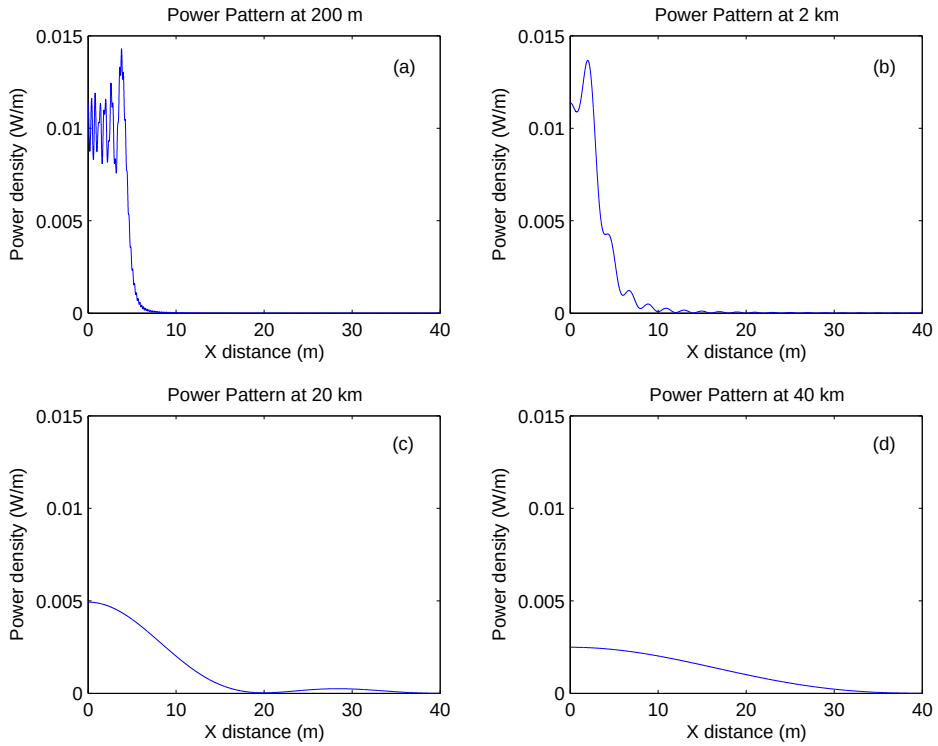

Figure 4.3 Beam power patterns at 200 m (a), 2 km (b), 20 km (c) and 40 km (d).

80% at 5 km. For the 20-m cloud, the antenna temperature is reduced by 5% of its brightness temperature at 5 km. Apparently, the larger cloud has the higher detection efficiency. A 10 m cloud and 20-m cloud may cause the same path delay but their corresponding antenna temperatures indicate a huge difference in importance to path delay. Varied detection efficiency severely degrades the feasibility of the WVR phase correction. To overcome this problem, new atmospheric models are needed.

4.4 Summary

We have introduced the basic calculation of a simple atmospheric model, which is used to derive path delays from the WVR observation toward water vapor lines. By demonstrating the 10-m antenna patterns in the near and the far-field regions, we have shown that the beam size can be either larger or smaller than the antenna size and the most sensitive positions of the power patterns are not necessarily at the centers.

The water vapor detection efficiency varies enormously depending on the sizes and heights of water vapor clouds. As a result, the scale factor of the 22 GHz water line is not a constant and varies by the physical conditions of water vapor clouds in real weather. Atmospheric models suggest that the cloud height plays a minor role in the WVR phase correction scheme. However, our simulations show that, with small water

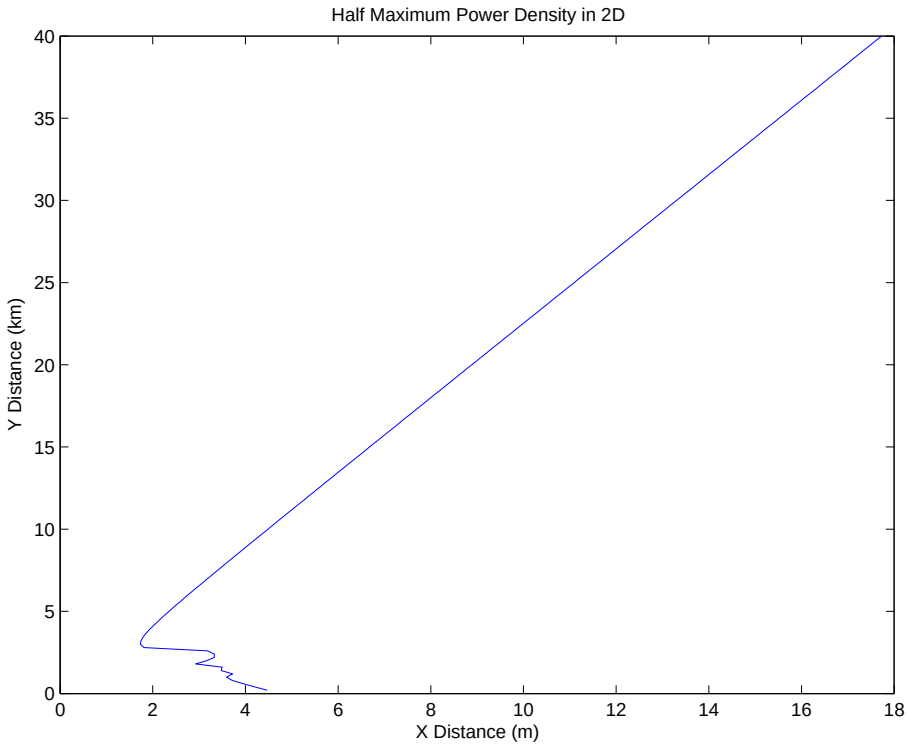

Figure 4.4 The simulated beam size from near- to far-field regions. The antenna is located from -5 m to 5 m along the x-axis. The straight line above 4 km implies the far-field patterns; the curvy line below 4 km indicates the irregular the near-field patterns.

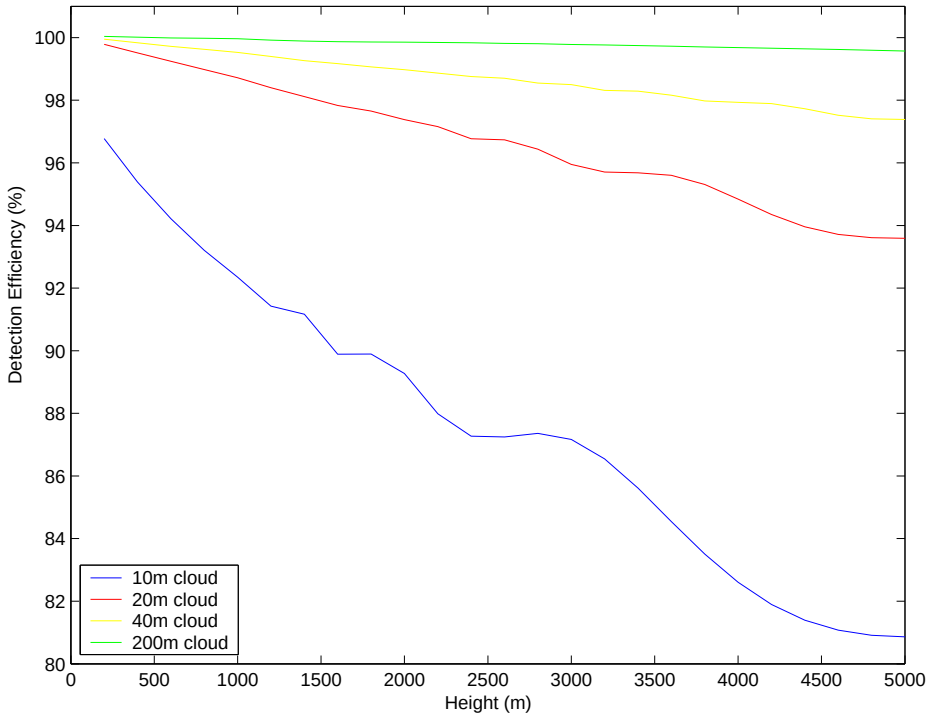

Figure 4.5 Detection efficiency toward water vapor clouds. The detection efficiency is the ratio of the antenna temperature to the sky brightness temperature.

vapor clouds, the antenna temperature still can suffer from the effects of the cloud size and height.

While the detection efficiency is low with small water vapor clouds, a higher scale factor is expected. Practically all clouds are finite-size so that the antenna temperature is always smaller than the brightness temperature, i.e. the scale factor should be always higher. However, the scale factor can be negative occasionally when a significant amount of water vapor is in the main beam but not in the column. We conclude that atmospheric models (e.g. Stirling et al. 2005; Pardo, Cernicharo, & Serabyn 2001) should include small-size water vapor clouds to improve the performance of the WVR phase correction.

Chapter 5

Water Vapor Radiometer

To examine the water vapor radiometer (WVR) phase correction technique, we have built two prototypes, which are referred as WVRs in the following discussion. In this chapter, we discuss our design for the CARMA WVRs, which mainly includes RF (radio frequency), IF (intermediate frequency) circuits, diode detectors, digitizers, signal processors and read-out computers. In addition, to keep the WVR temperature stable and calibrate gain fluctuations, we also designed a thermal regulation system and calibration system for the WVRs. We introduce these devices and systems in detail as well as software that controls the WVRs and reduces the WVR data.

5.1 System Requirements

5.1.1 Sensitivity

The WVRs measure the 22 GHz water vapor line to derive path delays for antennas. To recover the path delay variation for CARMA at millimeter and submillimeter wavelengths, the WVRs need to suppress the variation down to 1/10 λ. For 3 and 1 mm wavelengths, the ideal corrected path delay variations are 300 and 100 μm, respectively. Based on our simulations of the 22 GHz water vapor line, the scale factor to convert the atmospheric water vapor brightness temperature (mK) to path delay (μm) is 6. Previous observations suggest that it may be up to 12 (Chandler et al. 2004; Marvel & Woody 1998). If we assume that it is about 10, the sensitivity of the WVR should be 30 and 10 mK for $\lambda = 3$ and 1 mm phase corrections.

The system temperature T_{sys} of an uncooled 22 GHz receiver is generally 1000-2000 K. We can estimate the integration time t_{int} that we need by

$$WVR_{rms} = \frac{T_{sys}}{\sqrt{t_{int} \times BW}}, \tag{5.1}$$

where WVR_{rms} is the WVR sensitivity and BW is the channel bandwidth of the receiver. In our WVRs, BW is 2 GHz. Therefore, t_{int} is 0.5-2.2 seconds for $\lambda = 3$ mm phase correction and 5-20 seconds for 1 mm.

The integration times are reasonably short so we may not need cooled receivers to implement the water vapor phase correction technique.

Cooled receivers sometimes have long-term stability issues even when they have better sensitivities. The OVRO window tests (Chapter 3) suggest that the stability is more important than the sensitivity in the WVR application. So we decide to build our WVRs with uncooled receivers.

5.1.2 Cost

In the early stages of CARMA, we have a very limited budget for this WVR project. To minimize the cost, we have reused several RF devices from the OVRO water line monitors (WLMs), including antenna feed horns, RF amplifiers, IF amplifiers, filters, mixers, oscillators and diode detectors. Since these devices are not tunable, the WVR receivers will operate at the exact frequency as the OVRO WLMs.

According to the WVR sensitivity requirement, cryostats are not required for the WVR receivers. This significantly lowers the cost and allows us to purchase better devices for the rest of the system. We intend to use off-the-shelf solutions if possible. To date, commercial electronics are cheap and adequate for our WVRs. Embedded systems are affordable and powerful to replace desktop computers in many aspects. High density programmable logic chips are able to process 16-bit data at over 50 MHz clock rate. To date, digitizers and low frequency amplifiers are available by numerous companies. Thus, we can benefit from these in-production electronics to greatly improve our WVR system performance.

5.1.3 Stability

The WVR system stability, which includes the gain and system temperature stability, is one of the major concerns in our design. Poor stability can generate noise in the WVR data. Equation 5.1 estimates the sensitivity by considering only the characteristic of the system noise is like resistor noise, white noise. White noise is noise with a flat power spectral density over a very wide frequency band, i.e. any color or frequency shares the same power density (W/Hz). However, the system noise contains other types of electronic noises, such as power line noise and flicker noise. The power line noise is from the 60 Hz alternating current electricity, which can be easily eliminated by an over-sampling technique. The flicker noise is also known as 1/f noise; the noise power spectral density decreases as frequency increases. In other words, the lower frequency has higher power. The 1/f noise not only affects the system gain but also the system temperature. The gain stability can be improved by fast-switching scheme to calibrate the gain fluctuation. However, the system temperature stability needs a good thermal regulation system.

Besides the 1/f noise, the physical temperature of the receivers also varies the system temperature

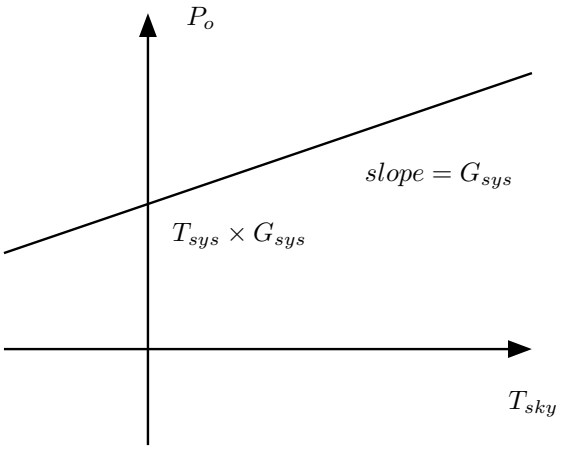

Figure 5.1 The output data P_o is a linear function of T_{sky}. The offset on the y-axis is $T_{sys} \times G_{sys}$ and the slope is G_{sys}.

and also slightly the gain. Most electronic devices are sensitive to physical temperature. The WVRs will be installed in an outdoor environment. The outside temperature fluctuation is about a few K in minutes, depending on the Sun and wind. A warm WVR receiver in a metal box sitting outside with a fair temperature regulation system cannot remain its temperature within a few K. It would be very difficult for such WVRs to detect 10 mK difference of water vapor signal when its physical temperature changes over 1 K. When the physical temperature of a 1000 K receiver changes from 300 to 299 K, 0.3%, the system temperature will also approximately change to 997 K as 0.3%. The change of the system temperature of 3 K overwhelms the sensitivity of 10 mK. A cooled receiver at 30 K may help stabilize the system temperature but stabilizing the physical temperature and system gain will be much more difficult.

The output power of the WVR, P_o, can be written as

$$P_o = (T_{sky} + T_{sys}(t, T)) \times G_{sys}(t, T), \tag{5.2}$$

where T_{sky} is the sky temperature, $T_{sys}(t, T)$ is the system temperature, and $G_{sys}(t, T)$ is the system gain. As shown in Figure 5.1, $T_{sys} \times G_{sys}$ is the offset on the y-axis and G_{sys} is the slope of the linear function of T_{sky}. However, T_{sys} and G_{sys} are functions of the time t and the physical temperature T. Thus, P_o is dependent on the time t and the physical temperature T as well. The relationships between t and T_{sys} and G_{sys} are based on the noise characteristics of powered devices. However, the relationships between T and T_{sys} and G_{sys} are not well-known, which are caused by thermal expansion, device thermal noise, device thermal temperature dependence, and material thermal noise. To lower this effect, the receivers need to be well thermally regulated.

5.1.4 Dynamic Range

In addition to the challenge of system stability, system dynamic range is also crucial to the WVRs. System dynamic range represents the ratio of the the maximum input signal to the sensitivity of the system. Ideally, we need to achieve the required sensitivity for the WVRs without compromising the input range. However, with a 1000-2000 K system temperature and the sensitivity of 10 mK, the required dynamic range is 60 dB, which is nearly impossible for any radiometer.

To fulfill this requirement, we design a new backend and calibration system for the WVRs. When the system temperature and the weather condition are stable, the dynamic range of the WVRs is extended to 60 dB by using a subtracting circuit to remove the low frequency parts of the input signals from the sky and the system noise.

5.1.5 Simplicity

Numerous radiometer designs are already available. To better localize the system problems of instruments and the atmosphere, we design the WVR system as simply as possible. The WVR receivers are superheterodyne receivers while the calibration system is Dicke-switching system. We only use heaters to thermally regulate the WVRs. A cooler or fan will cause interference in the electric circuits.

As prototypes, the WVRs are used to explore the WVR phase correction technique. More complex designs may work better but it would be hard to identify the sources of problems.

5.2 Overview of WVR

After taking those considerations and requirements, we finalize our WVR design as shown in Figure 5.2. Figure 5.2 is the WVR system block diagram. The WVR consists of a feed horn, a 22 GHz frontend, digitizers, a signal processor and a single board computer (SBC). The 22 GHz frontend includes RF (radio frequency), IF (intermediate frequency) devices and diode detectors. The digitizers, signal processor and SBC are the backend system. Calibration system and thermal regulation system are controlled by the SBC.

The feed horn is basically a type of antenna. When the WVR boxes are mounted on the CARMA dishes, the feed horns will receive water vapor signal reflecting from secondary mirrors. The feed horn can be used directly as an antenna to receive water vapor signal as well. However, its aperture is only 5/8" diameter. Therefore, the beam size is huge, 49°.

The frontend is a plate consisting of RF, IF devices and diode detectors. It amplifies the signal from the feed horn and down-converts to three very low frequency signals for the digitizers. The digitizers convert

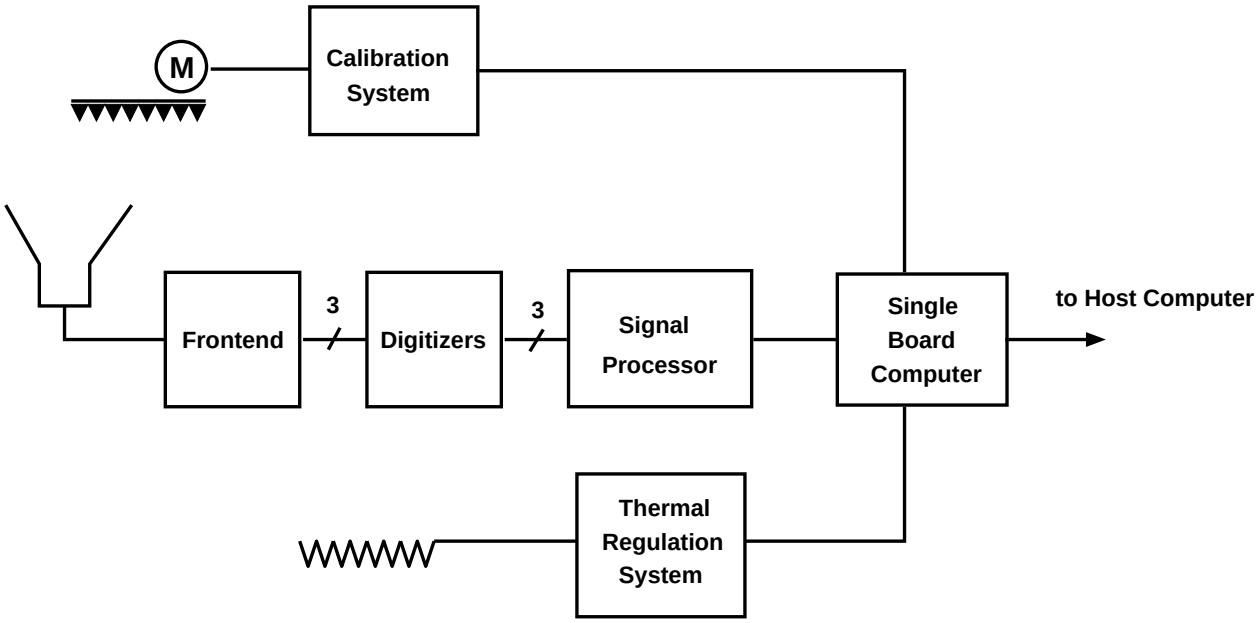

Figure 5.2 WVR system block diagram.

such low frequency analog signals to digital signals. The signal processor basically has two features. One is integrating the digitized signals as a digital integrator to lower the noise level by averaging millions of data points of the signals to a single data point every 1.4 seconds, which is sent to the signal processor. The other is to control the digital-to-analog converters (DACs) in the digitizers.

The SBC receives the data from the signal processor and stores it into computer files. The SBC also handles other control processes at the same time. It takes commands from a host computer. The host computer sends out commands, such as setting the gain value of amplifiers, motor positions, calibration timing and synchronizing time of the WVR clocks, to the SBC. The SBC accepts the commands and controls the digitizer boards, the calibration and thermal regulation systems. Moreover, the SBC can run sophisticated programs to automatically control the WVR based on weather condition.

The WVR is equipped with three thermal sensors, which indicate temperatures at three regions in and outside the WVR boxes. The temperatures are used by the SBC to control the thermal regulation system accordingly. We describe these devices and systems in more detail in the following sections.

5.3 Frontend System

Before the water vapor signal reaches the backend, it goes to an antenna feed horn and a RF amplifier, then a RF filter, a mixer, an IF filter, an IF amplifier, a triple-band filter, diode detectors and baseband amplifiers

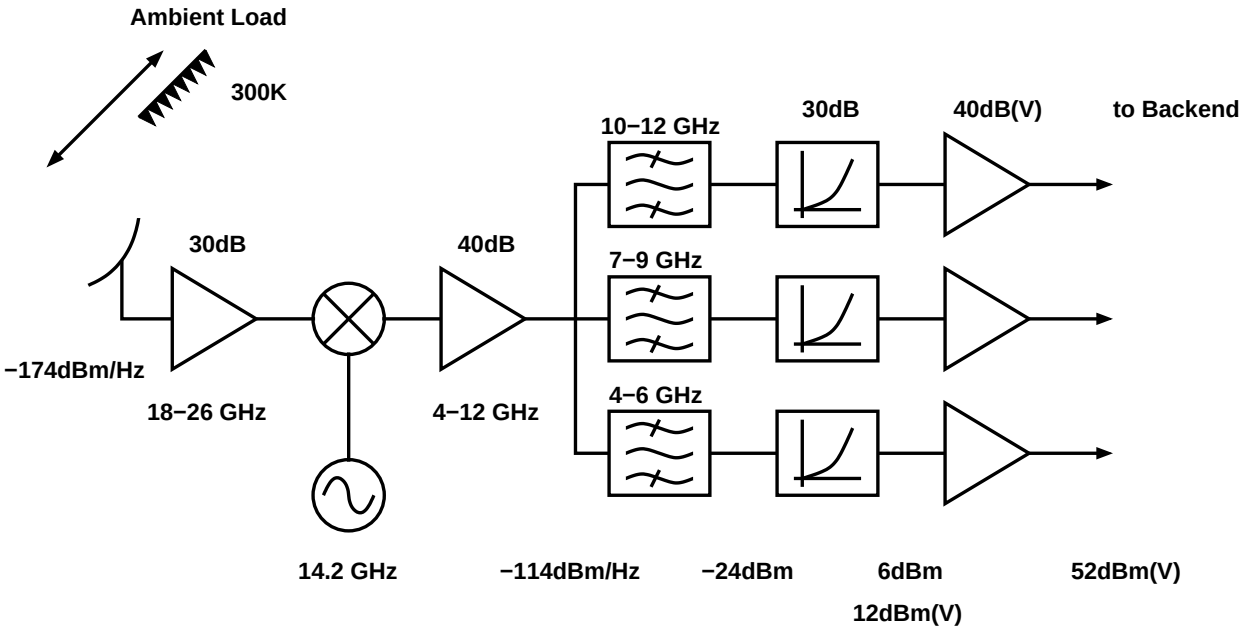

Figure 5.3 WVR frontend block diagram.

(see Figure 5.3). Since most of the RF components are taken from the WLMs, we basically simplify the OVRO WLM frontend design by using less components.

5.3.1 RF Amplifier

The first amplifier connected to the antenna feed horn is a low-noise amplifier (LNA), hereafter called the RF amplifier. The RF amplifiers used in the WVRs are commercial GaAs amplifiers, which are originally from the OVRO WLMs as the secondary RF amplifiers. The bandwidth is 18-26.5 GHz, which is a popular band for satellite and other industrial usage.

There are three types of RF amplifiers available in the CARMA project. The original OVRO LNAs from NRAO, the OVRO secondary RF amplifiers and the BIMA WVR amplifiers. We have compared the performances of these amplifiers at room temperature. The measurements of the performances are quite straightforward. We use the sky as a cold load and an echo absorber as a hot load to measure their system temperature and gains. The cold load temperature is assumed 10 K and the hot load temperature is about 300 K. The system temperatures of three amplifiers are about 1200, 1000 and 1800 K, and the gains are 35, 33 and 28 dB, respectively. For a LNA, a low system temperature is more important than a high gain. The gain can be compensated by low frequency amplifiers. Therefore, we decide to use the OVRO secondary RF amplifiers as our LNAs.

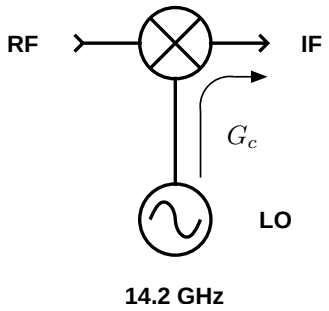

Figure 5.4 Conversion gain from LO

5.3.2 Oscillator

The local oscillators (LO) are dielectric resonator oscillators (DROs) generating a 14.2 GHz strong signal of 13 dBm for the mixers to downcovert RF signal to IF signal. The performance of DROs generally is better than those of Gunn and YIG oscillators. However, while DRO frequencies are fixed, Gunn and YIG oscillator frequencies are tunable. In our design, we only need a LO signal at 14.2 GHz. Thus, DROs are more suitable for the WVRs.

5.3.3 Mixer

The mixer and the LO signal convert the RF signal at 18-26.5 GHz to an intermediate frequency (IF) signal at 4-12 GHz. The mixer consists of a diode to operate at a nonlinear mode. Normally, when the LO signal is strong, the conversion gain from RF input to IF output is constant and the conversion gain from LO input to IF output is nearly 0. In most cases, the variation of the LO signal strength would not seriously affect the IF output. However, the sensitivity requirement of the WVRs is high enough to pick up the variation of the LO signal. Thus, we have conducted a test to measure the conversion gain G_c from the LO to IF to understand this impact.

Figure 5.5 shows that the IF output power versus the LO input power. The plot can be divided as two regions, a linear region and a saturation region. When the LO input power is -20 dBm, G_c is 14.5 dB. When the LO input power is greater than 5 dBm, G_c saturates as -3 dB. Therefore, the LO output needs to be greater 9 dBm. However, a G_c of -3 dB is still significant to the WVR sensitivity. We need to stabilize the LO output power by constraining the LO physical temperature. Otherwise, the variation of the LO output power can severely interfere the WVR data.

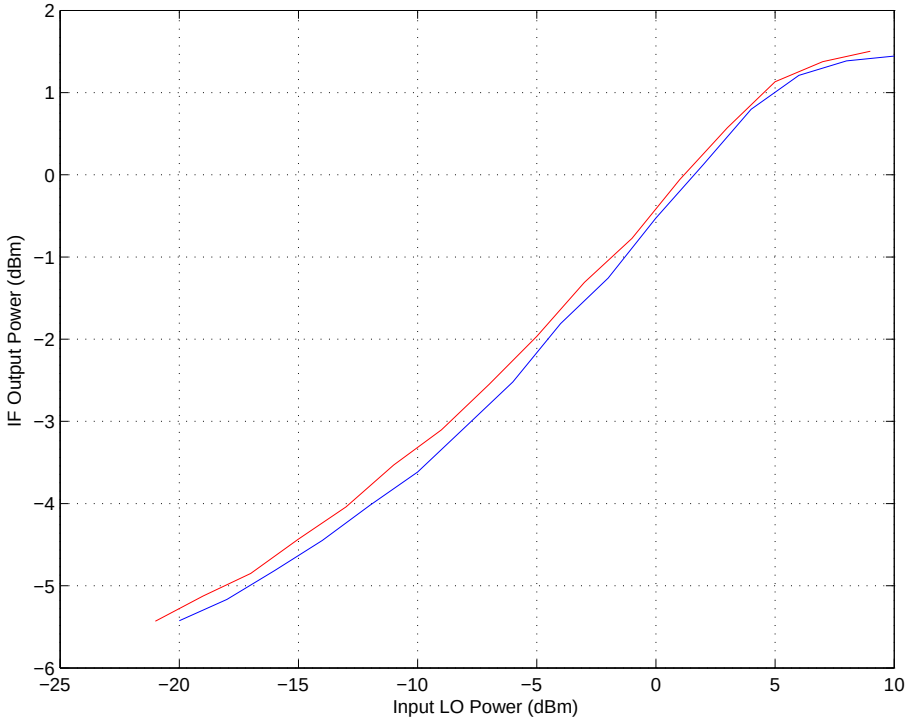

Figure 5.5 Conversion gain test. The plot shows the IF output power versus the input LO power. The gain can be obtained simply by subtracting the output from the input. In this test, we used a tunable 0-30 dB attenuator, 2 dB per step and a 1 dB fixed attenuator to generate 0-31 dB attenuation for the LO signal. However, the mismatch between the tunable and fixed attenuators caused a $sim0.5$ dB offset. The two lines are measured with and without the 1 dB attenuator.

5.3.4 Filters and Pads

We put a RF filter in the path between the RF amplifier and the mixer to suppress the image signal at 3.8-12.3 GHz. An IF filter in the output of the mixer suppresses another image signal at 32.2-40.7 GHz. The image signals are produced by the nature of mixers. Filters can select the demanded frequency bands to the output, while the images signals are blocked. With this design, the WVRs are technically single side band (SSB) receivers.

Pads are attenuators to lower standing waves in cables and connectors due to impedance mismatches. The mismatches cause the amplifier and mixer to be more sensitive to frequency and input power levels, which may produce unwanted results in the WVR data. Especially, filters are bi-directional devices. Without proper attenuation, standing waves can seriously occur in the filter paths. We put three pads on the input and output connectors of the mixer. Two of them particularly suppress the standing waves for the filters.

5.3.5 IF Amplifier

The IF amplifier amplifies the signal at an IF frequency range. The gain of the IF amplifier is 40 dB and the frequency range is 4-12 GHz. The WVR receiver is a superheterodyne receiver. The IF amplifiers provide an opportunity to select frequency bands and eliminate the corresponding image bands. Most wide band receivers are superheterodyne receivers.

5.3.6 Triple Band Filter

The triple band filter consists three bandpass filters at 4-6, 7-9 and 10-12 GHz corresponding to the sky frequencies, 18-20, 21-23 and 24-26 GHz, respectively. Comparing with the 22 GHz water vapor line as shown in Figure 5.6, the lower band is on the left side of the line. The center band is at the line frequency and the upper band is on the right. In this thesis, we use C1, L and C2 to denote the three bands, respectively.

5.3.7 Diode Detectors

The diode detectors, which are connected to the outputs of the triple band filter, convert the IF signals of the three bands to baseband signals. The baseband signals contain the information of the IF signal power levels. Ideal diode detectors only linearly respond to the input power level regardless of the input frequency. However, practical diode detectors are nonlinear and frequency-dependent. The bottleneck of the WVR dynamic range is the diode detectors.

The diode detector bandwidth is 2-12 GHz. Although we use the same diode detector model on the

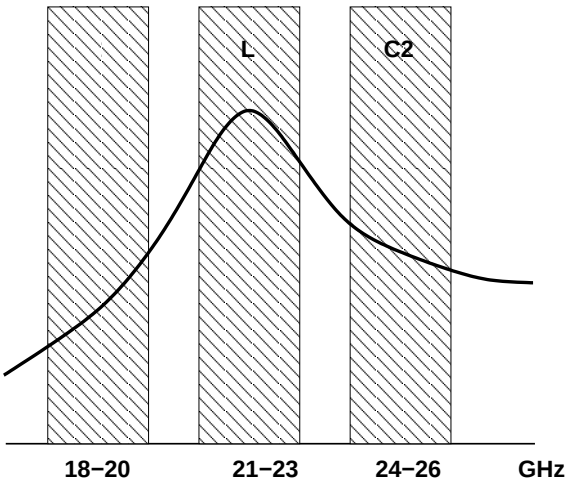

Figure 5.6 Triple band filter frequency response function.

three bands, we have tested the conversion gains of the diode detectors to make sure that they have similar gains. The conversion gains vary from 1 to 100 even in the same batch. We have picked the three diode detectors with similar conversion gains for each WVR so the differentiation of the system temperatures at three channels can be minimized.

5.3.8 Baseband Amplifiers

The baseband amplifier bandwidth is DC-10 KHz with a gain of 100 or 40 dB. The amplifier gain is programmable and set to fit the input range of the following digitizers, which is 0-2.048 V. The reason that we need to fit the range is to minimize the quantization noise of the digitizers. The amplifier model name is PGA405 made by TI Instruments.

We intend to install the baseband amplifiers near the diode detectors to lower the EMI noise from other electronics in the WVR box. Motors, heater and computers can generate relatively strong EMI noise to couple into the output cables of the frontend.

5.3.9 Frontend Integration

Figure 5.7 and 5.8 shows the spatial arrangement of these devices. A copper cylinder near the DRO LO is a thermal conductor regulating the heat flow from the frontend plate. Each powered device has an individual power regulator to stabilize the power supply voltage. To reduce cable losses, we avoid long cables and connectors when integrating these devices.

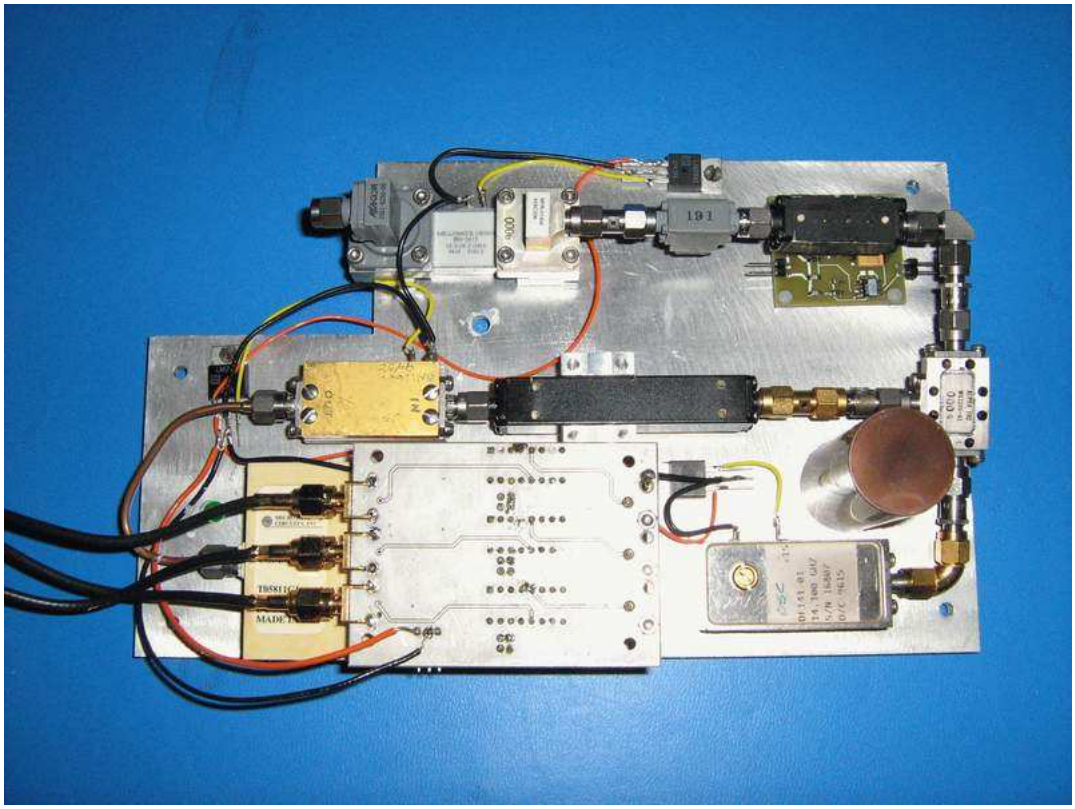

Figure 5.7 Top view of the frontend plate.

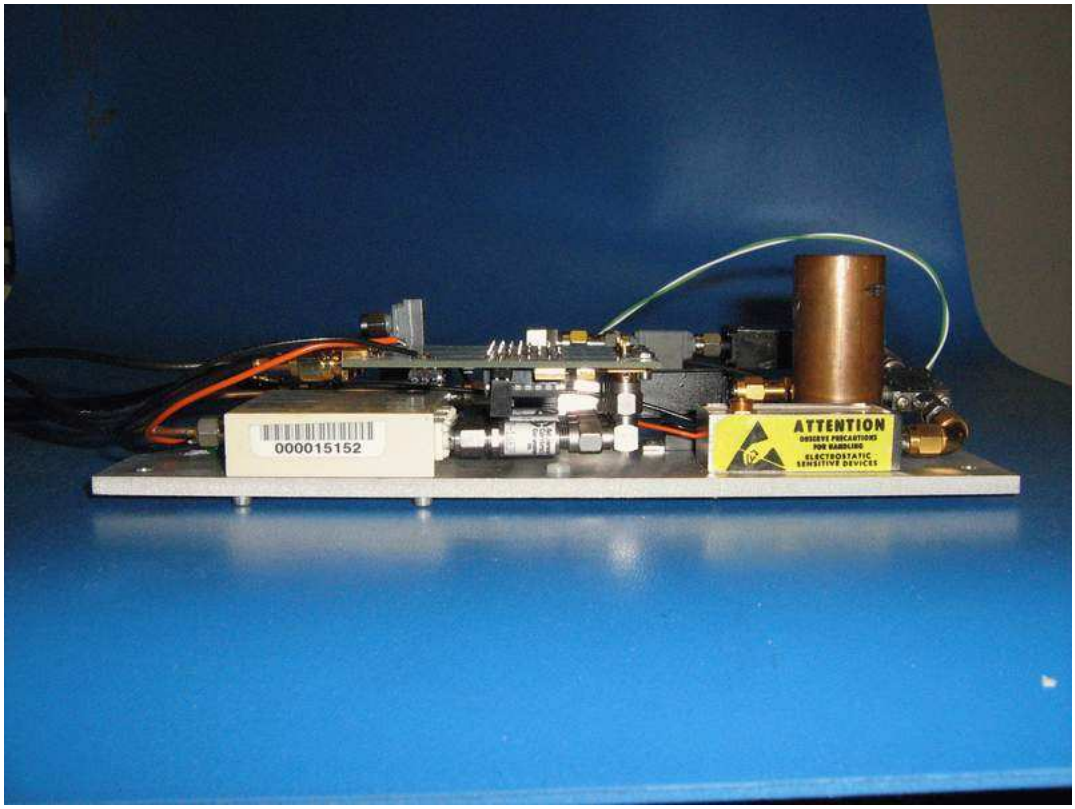

Figure 5.8 Side view of the frontend plate.

5.4 Backend System

The backend system includes digitizers, a signal processor and a single board computer (SBC). The three band signals from the frontend go into the digitizers, and then are integrated by the signal processor. The SBC receives and stores the data in a compact flash disk.

5.4.1 Digitizer

To improve the dynamic range of the WVR, we adopt a novel design for the digitizers. The digitizers are more than digitizing the analog signals into digital signals. A single digitizer contains a digital-to-analog converter (DAC), a analog-to-digital converter (ADC) and a programmable amplifier. The premise to achieve a higher dynamic range is to subtract the baseline of input signals and amplify the residue to the input range of the ADC. The DAC output is the amount of the signals to be subtracted. The programmable amplifier provides differential inputs to chop one input from the other. Both the ADC and DAC are 16-bit resolution with input range, 0-2.048 V. The gain of the programmable amplifier can be set as 1, 10, 100, 1000, which is exactly the same model as the baseband amplifiers. All control signals are from the signal processor.

The INL (integral nonlinearity) and DNL (differential nonlinearity) of ADCs and DACs meet the specification of 16-bit. The dynamic range is roughly 16×3, 48 dB. The new design does not make the digitizers become 32-bit or beyond 48 dB. However, if the input signal does not change over 48 dB in 15-20 minutes, which is the length of a single WVR data track, a control program can keep updating the DAC value and the amplifier gain to maintain the residue in the input range of the ADC. The input signal includes mainly the sky temperature and the system temperature. If the system temperature is stable, we should be able to detect the WVR with a dynamic range of 48 dB on short time scales and over 60 dB on long time scales.

Here, we compromise observable weather condition with a higher dynamic range. If the weather is unstable and the sky temperature changes over 48 dB during a period of a track, the input signal will saturate the digitizers. Such severe weather should happen less than 10% of the time at the site.

The ADC and DAC chips are AD7621 and AD5823 from Analog Device Incorporated. The ADCs run at 1 MSPS (mega sample per second) with a 25 MHz clock input. The output interface is parallel output with control signals. The output data rate is too high to be handled by a generic computer. The signal processor converts the high speed date rate to low speed data rate and sends to the SBC. The DAC interface is SPI (serial peripheral interface), which is not available on the SBC either. However, we wrote a logic circuit program for the signal processor so it will communicate with the DAC for the SBC.

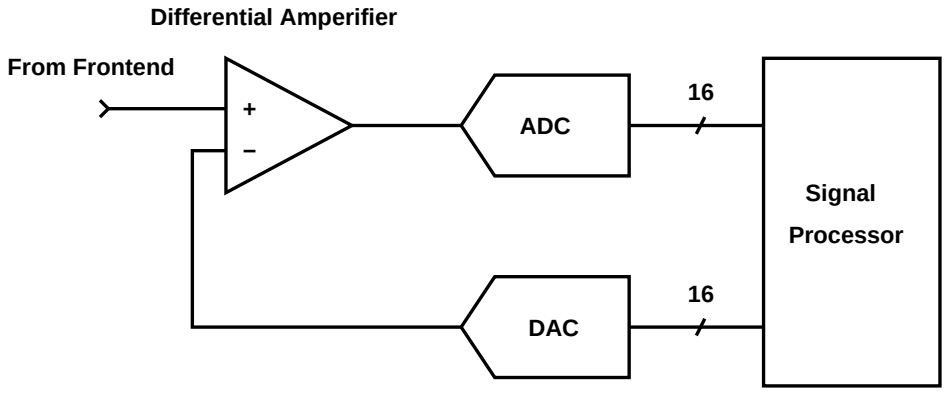

Figure 5.9 Digitizer block diagram

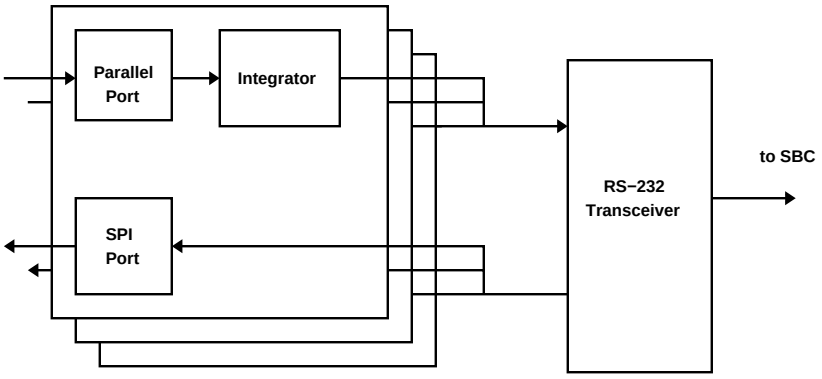

Figure 5.10 Signal processor block diagram

5.4.2 Signal Processor

The bandwidth of the digitizer boards is 10 KHz and the output data rate is 1 MSPS, which fully covers the bandwidth. However, the output data rate is too high to be handled by the SBCs. We need digital integrators to average out the data to a lower data rate.

The signal processor in our backend integrates the data from three digitizers and controls the DACs outputs to chop out the offsets of the input data. The integrator lowers the sampling rate, 1 MSPS (mega samples per second) down to one sample per 1.4 seconds. The data rate is so slow that the SBCs can receive the data via a RS-232 interface, which normally is 10 kByte/sec. The SBCs also control the DACs through the signal processor via the RS-232 interface.

The signal processors are physically field-programmable gate array (FPGA) chips, cyclone II, made by Altera Corp. The functional block diagram is shown in Figure 5.10. The serial peripheral interfaces (SPIs) are the interfaces to send commands to the DACs. The data from the ADCs are through parallel ports to the integrators in the FPGA chips.

5.4.3 Single Board Computer

The single board computers (SBCs) control the signal processors, calibration systems and thermal regulation systems. We installed Linux system in the SBCs to handle these tasks simultaneously. To make the WVR programming more flexible, we use a complete OS (operating system) with a CPU rather than a single program in a microcontroller. Multi-tasking Linux OS plays an important role in controlling the WVRs. Many concurrent events need to be processed by the SBC. The nature of Linux OS provides a robust environment to run multiple programs at the same time. We can write specific programs individually for the thermal regulation system and observing without extra efforts.

The SBCs are TS-5300 PC/104 model from Technologic Systems Corp. It is a X86 compatible system including a 133 MHz AMD 586 CPU, 16 MB SDRAM, a compact Flash disk, a 10 Mbps Ethernet port, a LCD output port, two RS-232 ports and a few general purpose input/output (GPIO) ports. The GPIO ports are used to control the servo motors in the calibration system and the heaters in the thermal regulation system. One of the SBC jobs is taking commands from a host computer via TCP/IP on an ethernet network. The delay of ethernet network is less than 10 ms so that we can synchronize the WVR clocks on the SBCs via the internet. The host computer can be any computer with internet access. The SBCs are so compact that they can be installed in the WVR boxes to simplify the integration of the WVR system.

5.5 Calibration System

To maximize the dynamic range of the WVR, we have used the DACs on the digitizer boards to subtract the offset of the output signals of the baseband amplifiers. However, such a design increases the difficulty of the absolute calibration, which is already a great challenge.

The absolute calibration has been a fundamental problem to radiometers. It can be solved generally by observing an exterior calibrator near the desired source with a similar power level of the source, which is the case with single-dish telescopes and interferometers. Unfortunately, it cannot be done with the WVRs because no such common calibrators exist for all WVRs. Installing individually external hot and cold loads as calibrators for each of the WVRs cannot eliminate the gain and system temperature errors between antennas. External hot and colds loads work only for a single radiometer to compare one channel data with others. These channel data share the same gain and system temperature errors, which are roughly 1-10%. Therefore, the feature of data remain intact. When comparing two radiometer data, the errors are uncorrelated and will completely reflect on the WVR data. Not only the absolute gain and system temperature are incorrect but also the features of data disappear or is unreal.

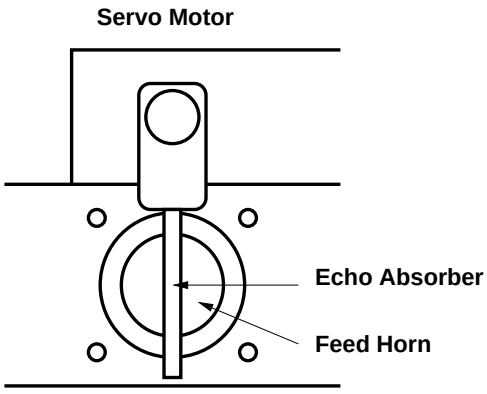

Figure 5.11 Ambient load. The ambient load is an echo absorber strip attached to a servo motor. The servo motor controls the position of the ambient load.

Therefore, we calibrate the gains of the two channel data with a reference channel but leave the absolute gain calibration of the reference channel to interferometers. The interferometric data can indicate the difference of the path delay between two WVRs and then apply that information to figure out the corresponding gain values. In this way, we can obtain the spectral profile of the 22 GHz water vapor line in terms of time first. Then the interferometric data decides how to derive the path delays from the WVR data.

In our calibration system, we only use a single ambient load to couple into the signal path. It is unnecessary and difficult to know the WVR system temperature and the gain within the accuracy of a few mK. Thus, the ambient load provides a little bit extra wide band power to the WVR receiver so we can compare the power levels at the three channels and reconstruct the 22 GHz line feature by subtracting the continuum (C1 + C2) /2 from channel L.

The calibration system consists of a servo motor and a narrow strip of echo absorber as shown in Figure 5.11. The servo motor is attached on the top of the frontend box. We decide to only chop the antenna beam partially because a fully beam-covered ambient load saturates the system. The sky temperature is theoretically 10 K and the ambient load is about 300 K. We subtract the offset of the baseband amplifier output signals, since the absolute amplitude of the signals are not required any more. The sky temperature rms is about 100 mK and the system temperature is about a few 100 mK. The WVRs will adjust the gains and offsets to detect a few mK with the 16 bit ADCs. Thus, a fully beam-covered 300 K ambient load signal is too bright when the system input range is only 1 K. However, the drawback is the power level of the ambient load is unknown and standing waves may degrade the stability of the calibration at some frequencies.

$$P_o = ((1-a)T_{sky} + aT_{amb} + T_{sys}) \times G_{sys}, \tag{5.3}$$

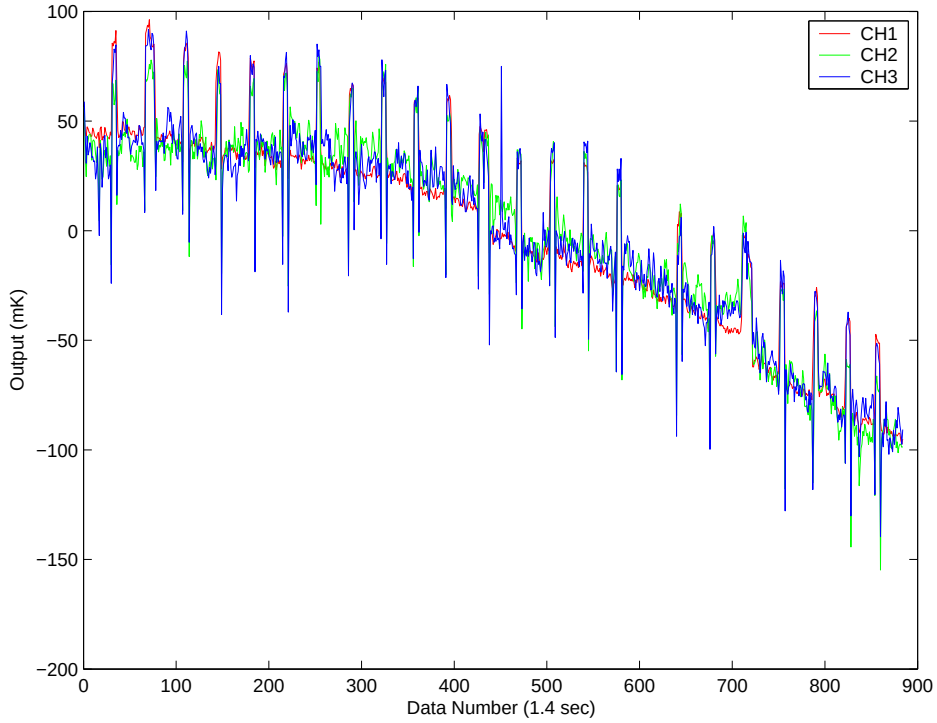

Figure 5.12 Calibration test. We tested the calibration by putting an echo absorber in front the WVR antenna horn to check the consistence of the three channel data set. Here we subtract the means of the data sets and apply the gain calibration.

The test result shows that the repeatability of the calibration system fulfills our requirement in Figure 5.12. Three channel data show almost exact trends after calibration, when the WVR observes a large echo absorber in the most sensitive mode.

5.6 Thermal Regulation System

Physical temperature is extremely critical to the gain G_{sys} and system temperature T_{sys} stabilities of the WVRs. Since our stability requirements are unusually high, almost the thermal effects of every component before the digitizers can be comparable or even greater than water vapor signal strength. Especially the frontend box that downconvert the high frequency signals to baseband signals is the most sensitive part of the WVR. Therefore, we intend to minimize the frontend temperature rms to a few mK per 10 seconds for a 15-20 minute long track.

Figure 5.13 illustrates the basic design of the thermal regulation system for the WVRs. We use a heater to control the temperature of the WVR. There are three temperature monitor points in a WVR. T1 is the one attached on the frontend plate, T2 monitors the WVR box air temperature. and T3 records the outside

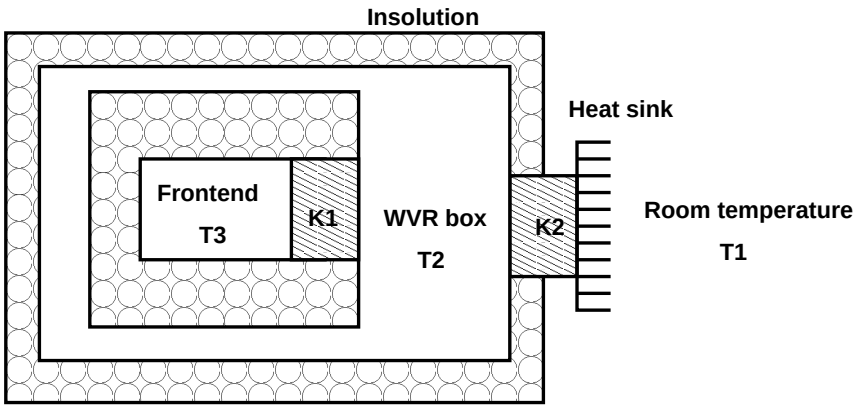

Figure 5.13 Thermal regulation system. K1 and K2 are thermal conductivities from T3 to T2 and T2 to T1.

temperature. The thermal regulation control program will control the heat based on these three sensors.

5.6.1 Feedback Loop

Proportional-integral-derivative (PID) feedback loop is a well-known control mechanism to keep a system stable. We use the proportional feedback in our thermal regulation system to balance the system reaction speed and the deviation between the controlled temperature and target temperature. The controlled temperature is the physical temperature of the frontend plate, which is controlled by a heater. The target temperature is the temperature that we want the system to remain.

We have tested the response time from the heater to the thermal sensor is about 20 seconds to 1 minute. It implies that the WVR thermal capacity is relatively large and then we cannot control the temperature variation faster than the response time. Thus, we need to increase the thermal capacity or insulation of the frontend to suppress the high frequency parts of the temperature variation. We carefully insulate the frontend box with double-layer bubble wrap but install a copper rod to be a thermal pipe, which may be controlled by the system.

5.6.2 Convection

To further stabilize the temperature gradient on the frontend plate, we put plastic beads in the frontend box as shown in Figure 5.14. We compare the results before and after putting beads. The temperature rms is lowered by a factor of 4 by filling beads in the box. Therefore, we decide to use beads to prevent the air convection.

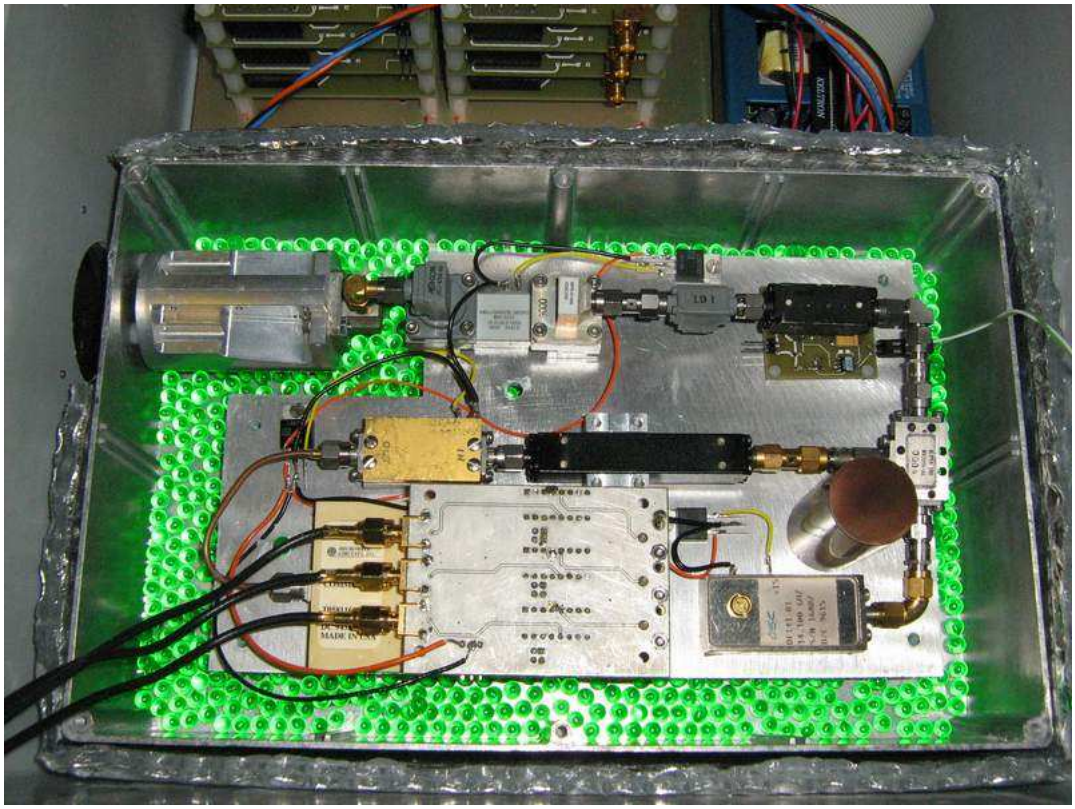

Figure 5.14 The frontend box. The beads will fully cover the plate. Most beads are remove so the plate can be seen.

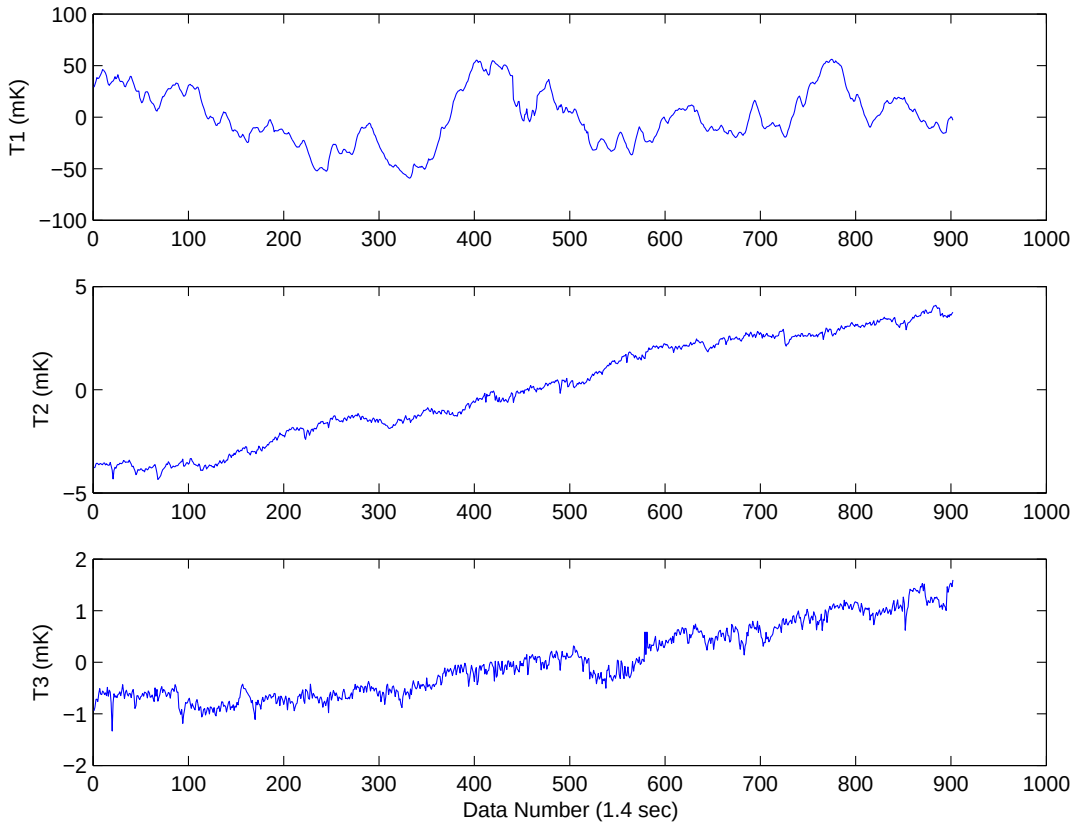

Figure 5.15 Temperature fluctuations outside the box (T1), inside the box (T2) and on the frontend plate (T3). The offests of the data set are subtracted.

5.6.3 Laboratory Test Results

We measure the temperature variations at three points, T1 outside the box, T2 inside the box, and T3 on the frontend plate. Figure 5.15 shows the temperatures versus time and Figure 5.16 shows the temperatures versus frequency. To further make sure that one monitor point on the frontend plate is enough, we have tested the temperature variations on three different locations of the plate and they share approximately the same rms.

5.7 WVR Control and Data Processing

We take extra precaution designing our software structure. There are many high and low level programming languages available in computer science. One does better than the other on certain types of tasks. The WVRs are prototypes used to explore the atmosphere and instrumentation. Thus, in this WVR project, we prefer to use simple and flexible programming languages and structures.

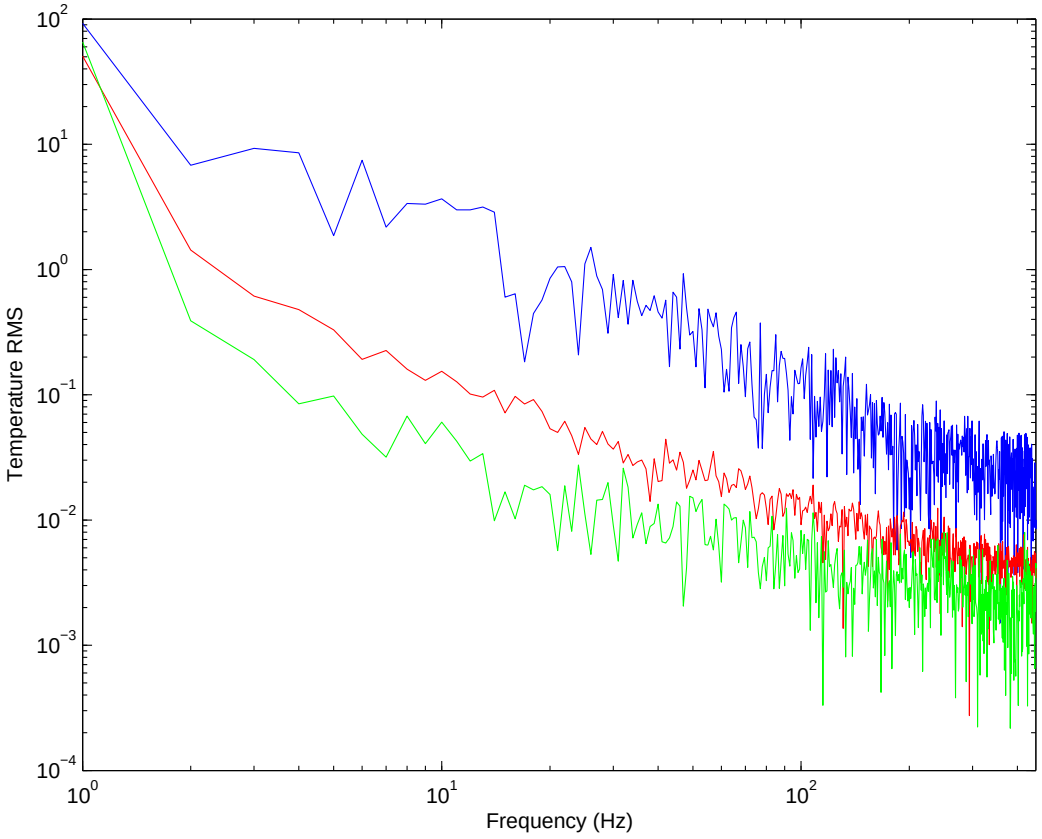

Figure 5.16 Spectra of the temperature fluctuations. The top is T1, the middle is T2, and the bottom is T3.

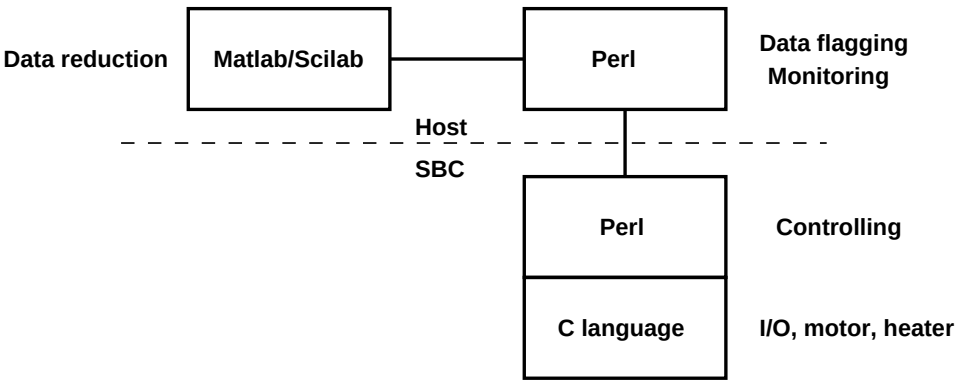

Figure 5.17 WVR software structure

We choose C language and Perl script language to build up our software package. C can be used to communicate with devices elegantly while Perl provides the flexibility to access data conveniently. Figure 5.17 presents our design of the WVR software structure. The host Perl scripts communicate with the SBC Perl scripts to control the WVRs. The host scripts check the time lag between two WVRs and monitor the atmosphere condition. The main script in the SBC controls the data stream from the signal processor to the host while other scripts control the calibration system with the servo motor and thermal regulation system with the heater and sensors. It is possible to have a master script in the host to control all tasks running in the SBCs. Currently, we do not have an interface for the MIRIAD package. We use Matlab or Scilab to reduce the WVR data.

5.8 WVR Integration

We use NEMA fiber glass boxes as enclosures for the whole WVRs, including the receivers, power supplies, heaters, servo motors and SBCs. NEMA weatherproof enclosures can protect delicate electronics from harsh environments in the outdoor tests. Figure 5.18 shows the view of inside the box. The frontend box is in the lower part of the box with a servo motor attached on it. A heat sink is attached to the thermal conductive copper rod on the frontend plate. The frontend box is insulated with double layer bubble insulation. The digitizer boards and a power supply are in the upper part of the box. The SBC and signal processor is on a plastic board as the second layer in the upper part of the box.

Figure 5.19 is the view on the back of the box cover. The heater with a solid state relay is on a copper plate. The copper plate and the heater control the heat flow from the WVR box to outside air. The ethernet and power cables go into the box from the front door. Figure 5.20 shows two WVRs on a workbench.

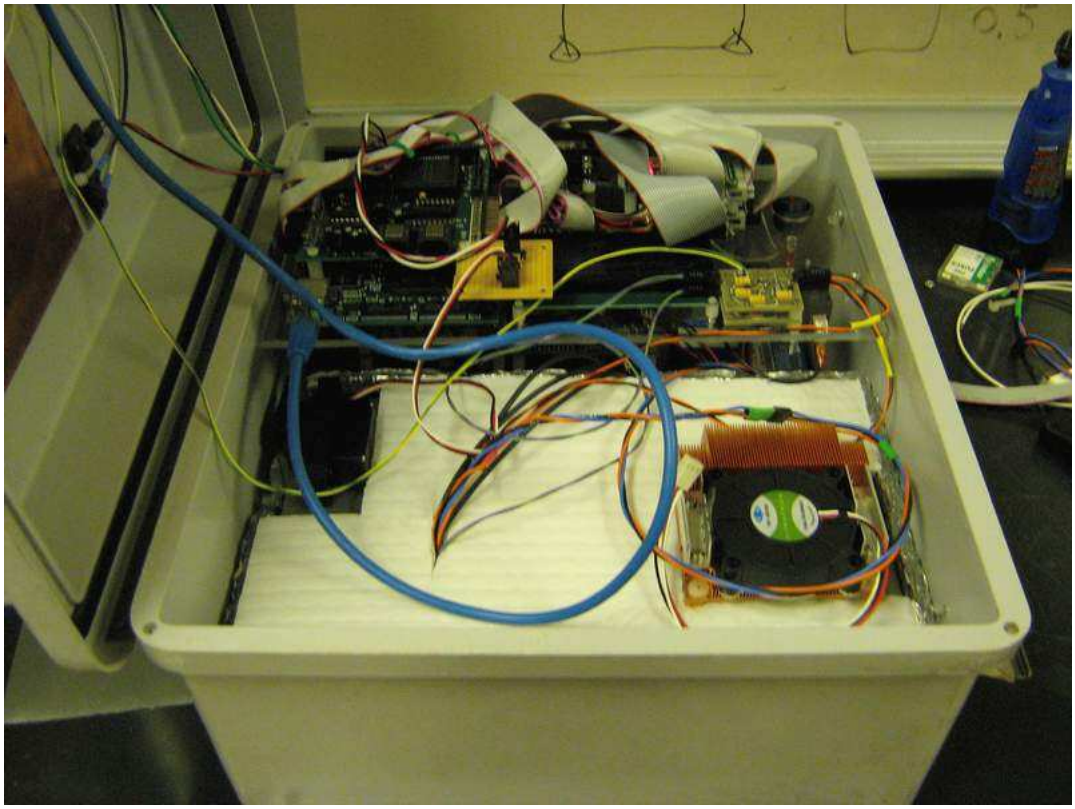

Figure 5.18 Inside view of the WVR box on the right.

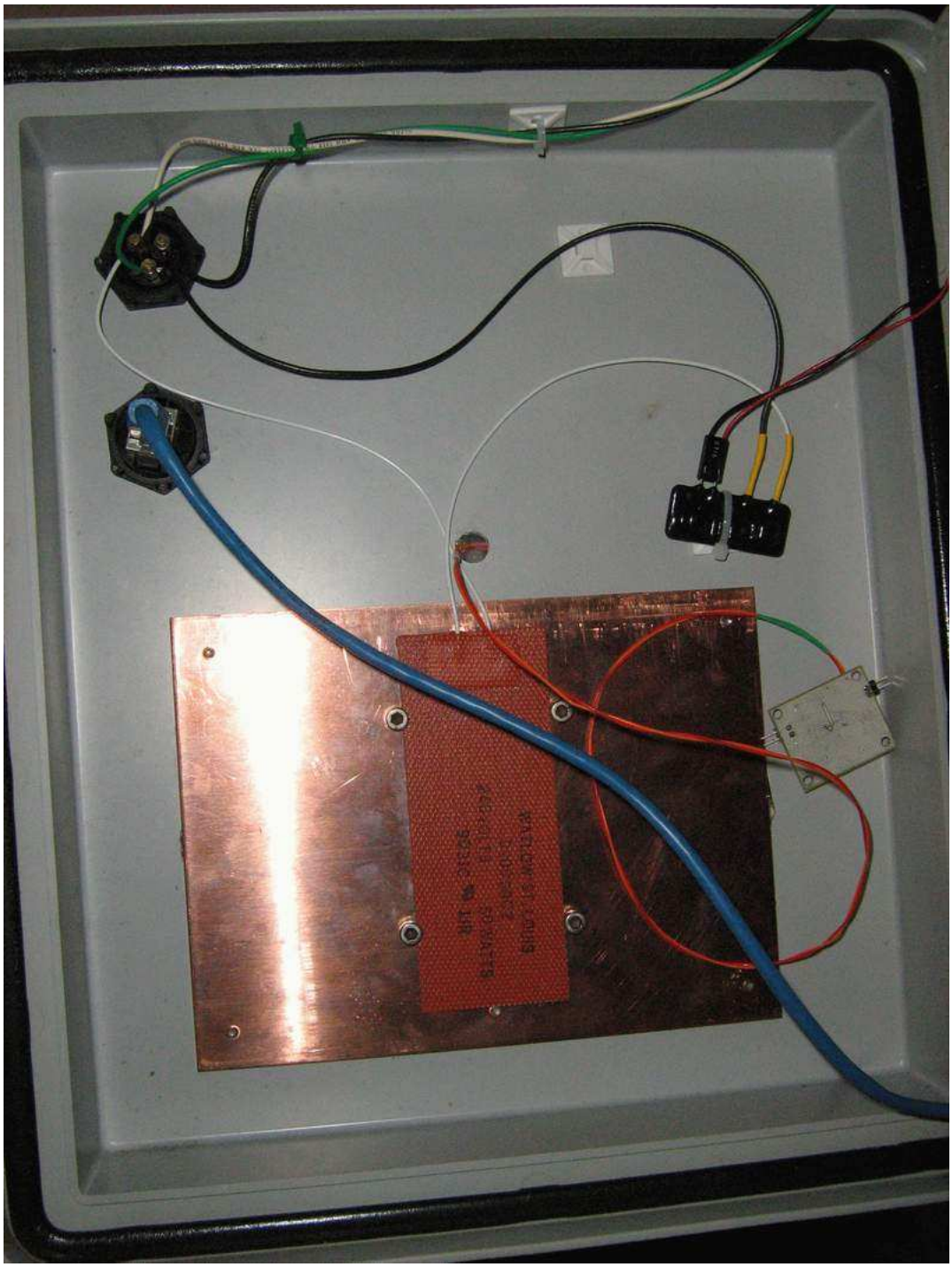

Figure 5.19 Inside view of the WVR box on the left.

Figure 5.20 WVR boxs.

5.9 Summary

We have introduced our WVR prototypes and verified our design in a laboratory. The backend system performance fulfills our requirements with a dynamical range of 48 dB, which potentially can be more than 60dB at an outdoor test. The frontend needs more tests toward the sky to determine its performance. However, the calibration system works better than expected. While the effect of the servo motor position error is negligible, the ambient load provides a steady reference signal for the WVR. Thermal regulation system can stabilize the frontend plate temperature within a few mK in the lab but also needs more outdoor tests. The required software has been completed and is available. We can further test our WVRs on the roof of the astronomy department and at the CARMA site to actually observer tropospheric water vapor.

Chapter 6

Water Vapor Radiometer Tests

We have shown our water vapor radiometer (WVR) design and built two prototypes for CARMA. So we can test their performance and investigate the WVR phase correction technique in practice. In this chapter, we present our WVR test results in a laboratory, on a roof and at the CARMA site. The laboratory test was carried out to ensure that the performance of the WVRs fulfills our requirements before we proceed to outdoor tests. The calibration system and thermal regulation system have been tested in the laboratory before the integration of the WVRs. However, we need the WVRs to observe the same external source for a long period of time to confirm their consistency. The roof tests can show the performance of the WVRs under real weather conditions. The roof tests occurred on the roof of the astronomy building in University of Illinois at Urbana-Champaign. The precipitable water vapor (PWV) on campus is presumably very high. Therefore, we expect the 22 GHz water vapor line is brighter than that at the CARMA site. The WVRs on the roof should also "see" larger water vapor fluctuations. Finally, only the CARMA site tests can truly demonstrate the feasibility of the WVR phase correction technique. While the phase monitor at the site produces reliable atmospheric phase rms data every minute, we installed the WVRs near the phase monitor mirrors. Then we can compare the phase rms from the phase monitor with that estimated by our WVR system. Thus, the correlation of two data sets and the scale factor of the 22 GHz water vapor line can be determined in this manner (Shiao & Looney 2008).

6.1 Laboratory Wall Test

We have checked the WVRs in a laboratory by setting up the WVRs to observe the same source, an echo absorber, which is attached to a wall. The WVRs pointed to the echo absorber from different directions of lines of sight perpendicular to each other as illustrated in Figure 6.1. The distance from the absorber to each WVR antenna window was about 60 cm. The echo absorber size is 30 cm $\times$ 30 cm. The far field limit of the WVRs is about 30 cm and the beam size is 49°. Although the sidelobes of the WVR may pick up other thermal sources such as the floor and the background around the echo absorber, in this setup the sidelobe

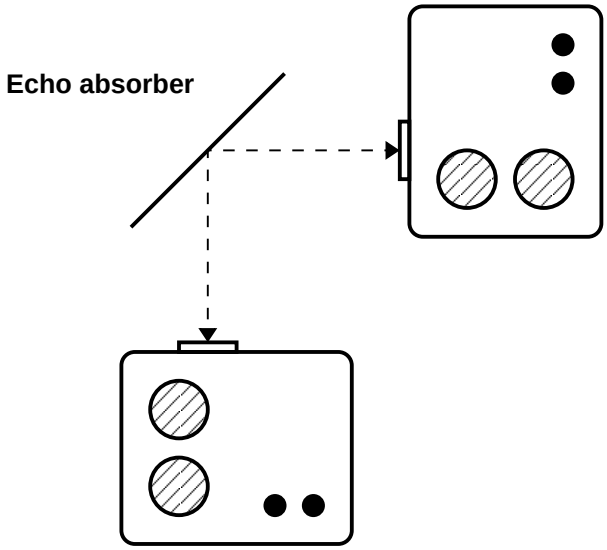

Figure 6.1 Two WVRs observe the same echo absorber in the wall test.

effect should be minimized.

Figure 6.2 shows the wall test result. We combined two successive tracks as an 80 minute long observation for each WVR data in Figure 6.2 (a). The result confirmed that the WVRs detected the echo absorber thermal emission with an uncertainty of 30-50 mK. The data tracks are C1 channels, which are sampled every 1.4 seconds. C1 channel data is the continuum channel at 18-20 GHz, which is the most sensitive channel in the WVR. The room temperature at the same time period is shown in Figure 6.2 (b). The room temperature were measured by the two WVRs separately. The two tracks in Figure 6.2 (b) show that the room temperature variation due to air convection is about ± 100 mK. The echo absorber temperature variation should be lower than that value because of its thermal capacity is much larger than the air. As mentioned in the last chapter, the air convection plays one of key roles in thermal stability. However, without knowing the temperature variation of the echo absorber, we cannot conclude the system stability at this point. Thus, the upper limit of the stability in the laboratory is 50 mK.

6.2 Illinois Roof Tests

The roof tests were conducted in 2007 winter. We have used the WVRs to monitor the water vapor under a variety of weather conditions, except for snow and rain. As shown in Figure 6.3, two WVR sat side by side with a control box on the roof. Although the roof is noisy at radio frequencies due to air conditioners and fans, the roof observation still gave useful information to evaluate the performance of the WVR. The roof tests included tasks to determine if the calibration system could function flawlessly when the sky temperature

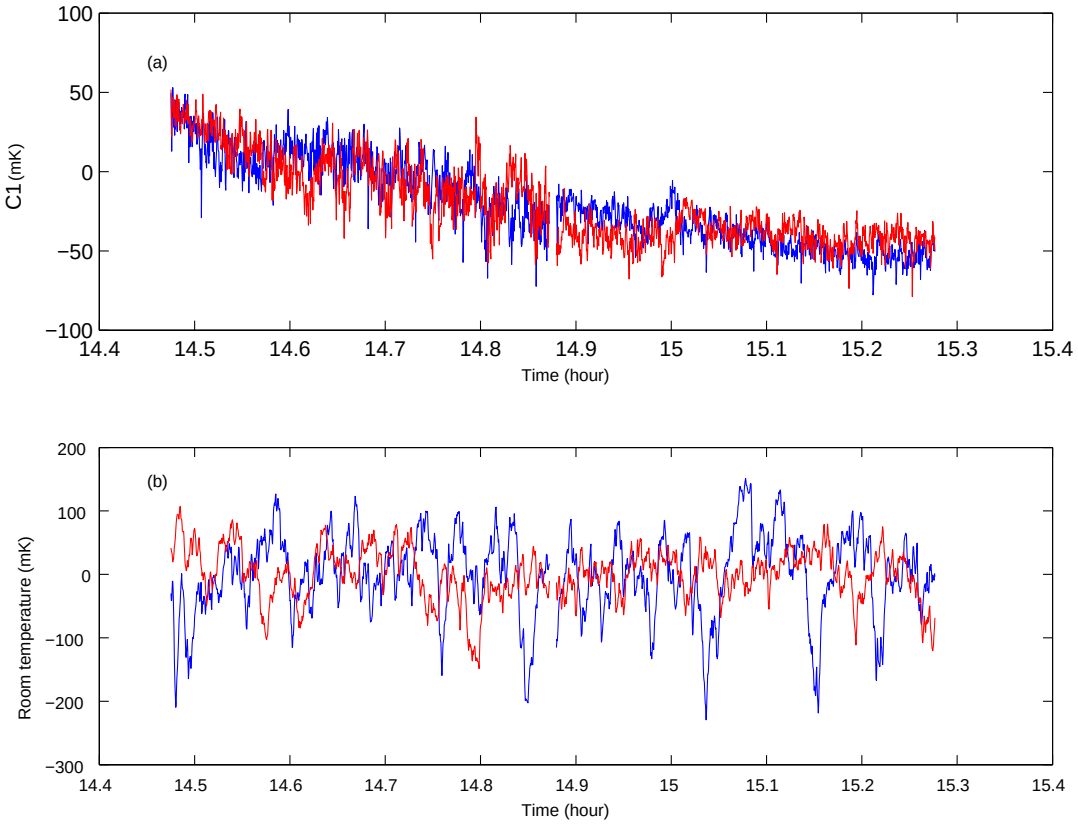

Figure 6.2 Wall test result. (a) Two C1 tracks of the WVRs. (b) Room temperatures. The negative values are due to the average subtraction.

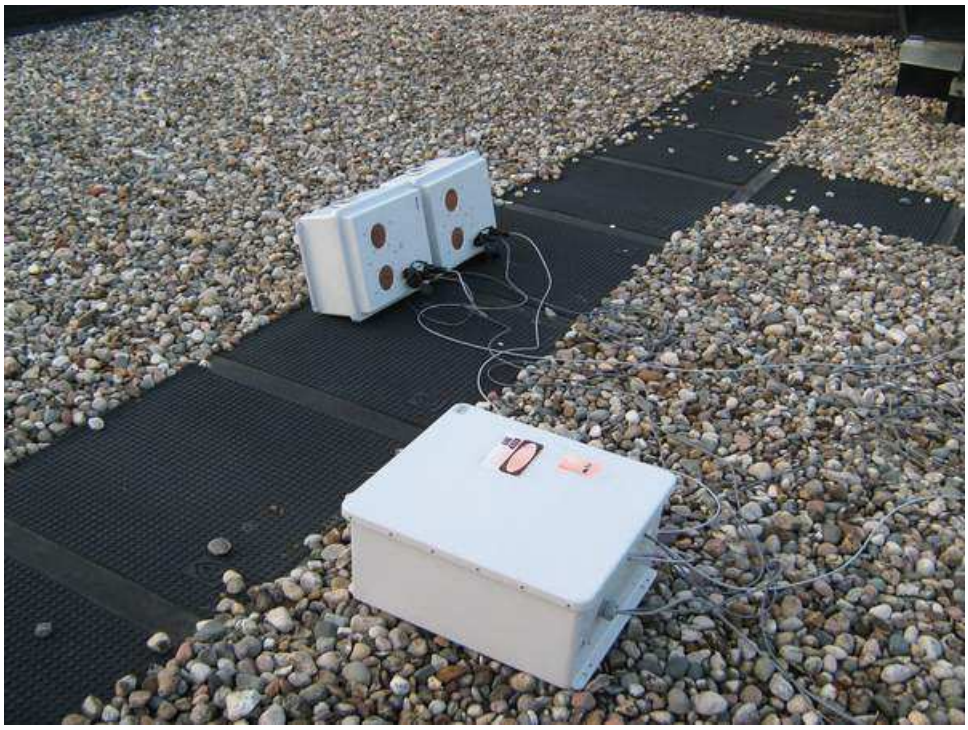

Figure 6.3 Two WVRs and a control box were set up on the roof.

changed rapidly and if the thermal regulation system could hold the temperature when the weather varied. The main task of the roof tests was to determine the stability and sensitivity of the WVR system as the wall test in the laboratory.

The setup of the roof tests was that the WVRs observed toward the same part of the sky by sitting side by side and slightly inclining to one side as shown in Figure 6.3 and 6.4. The premise of the roof tests was checking the consistency of the two WVR data set as the wall test. This time the source was the sky. The WVR beam size is 49° so the two WVRs should mostly observe the same part of the atmosphere. The control box in Figure 6.3 contained the host computer to communicate with the single board computers (SBCs) in the WVRs. It could synchronize the data streams from the both WVRs and stamp time on the data sets. When the SBCs hang for too long, the host computer could reboot the WVRs with solid state relays. The temperatures inside the WVR boxes took over six hours to gradually be stable. We usually waited over a night before taking data.

The calibration system under real weather conditions worked very well. Since we only seek relative gain calibration, we picked the C1 channel as the reference channel to calibrate the gains of the other two channels. However, the thermal regulation system could not hold the frontend temperature on the roof as well as in the laboratory. The wind strongly influenced the heat dissipating from the WVR box, i.e. the

Figure 6.4 A closeup view of the WVRs.

heater inside the box could not keep up the loss of heat under a windy condition. At night, the outside temperature also changed too fast. We needed to make the length of data tracks shorter to calibrate the system faster. Thus, the track length was 12-15 minutes in our tests depending on weather conditions.

First, we examine the weather conditions by checking data from one of the WVRs. Figure 6.5 to 6.20 were taken on October 18th 2007. The sky temperatures of three channels were not so stable. A cloudy storm was leaving when this track started to observe the sky. Three channel temperatures showed large fluctuations in the beginning of the track but they gradually subsided to relatively stable conditions. If we transform the data to a spectrum as shown in Figure 6.6, we can see a very typical spectrum of turbulence. Low frequency parts are stronger than high frequency parts. The blue, red and green lines stand for C1, L and C2 channel data, respectively. If we check another data set taken on a cloudy day in Figure 6.7 and also transform to a spectrum in Figure 6.8, we can see a similar characteristic of turbulence spectra. These two tracks were taken under normal cloudy weather. Figure 6.9, 6.11 and 6.13 were taken when the weather was really bad; Figure 6.10, 6.12 and 6.14, respectively, are their spectra. Figure 6.15, 6.17 and 6.19 were taken when the weather was relatively good. Figure 6.16, 6.18 and 6.20, respectively, are their corresponding spectra. When the weather was stable, the WVR data shows smooth and consistent results on the three channels. On the other hand, when the weather was extremely unstable, the data shows irregular patterns

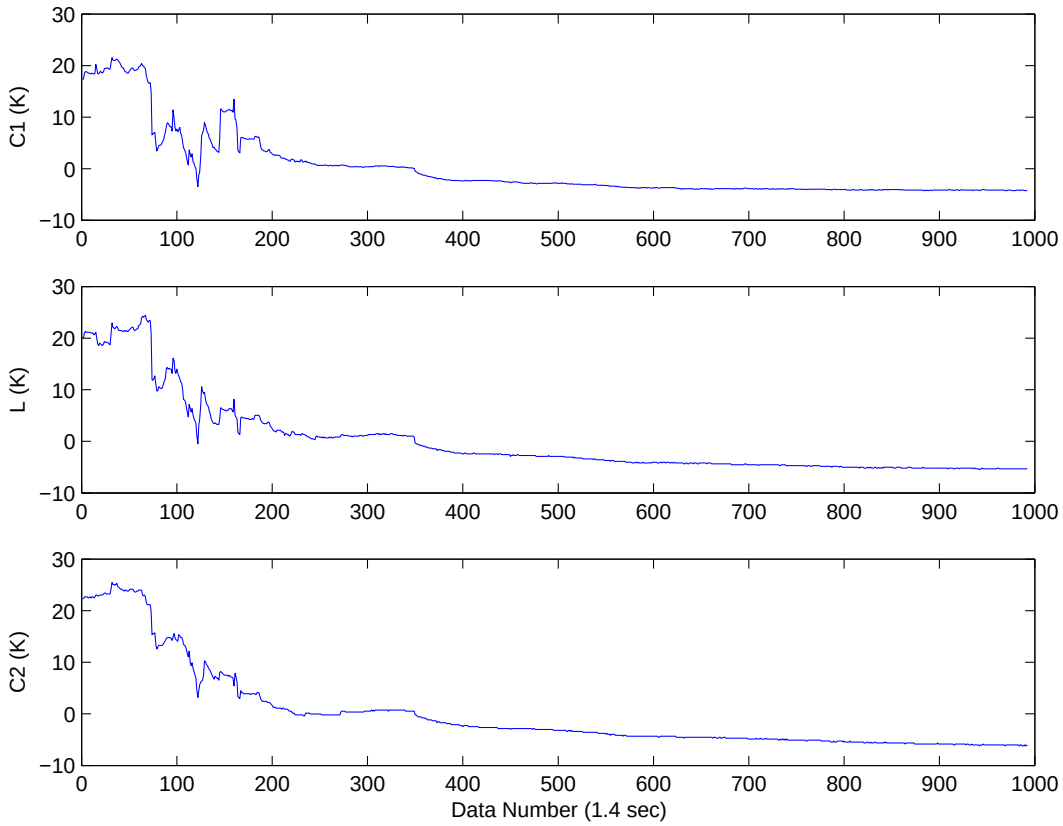

Figure 6.5 WVR observation on Oct. 18th 2007. The observation started when a cloudy storm was leaving. This data and the following in this chapter are average subtracted.

and the three channel data are less consistent.

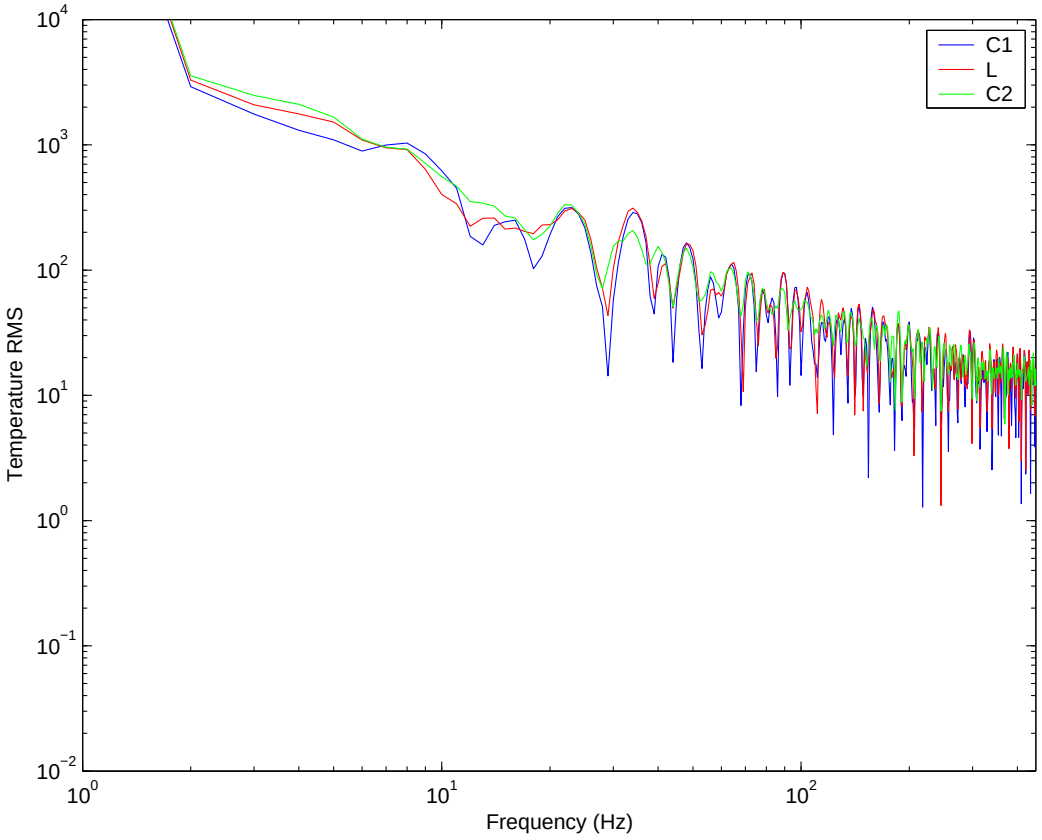

Figure 6.6 The spectrum of WVR data in Figure 6.5. Three channels show similar power density distributions.

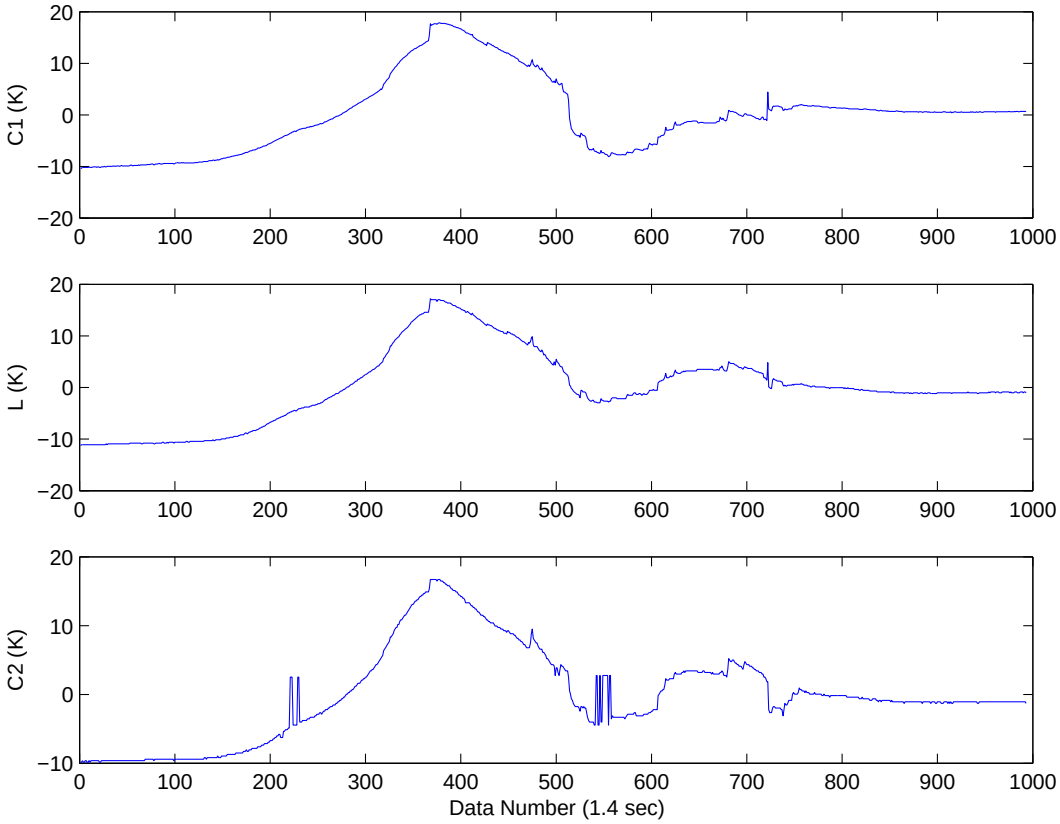

Figure 6.7 WVR observation on Oct. 11 2007. The weather was cloudy. Some quantization error occurred in this track.

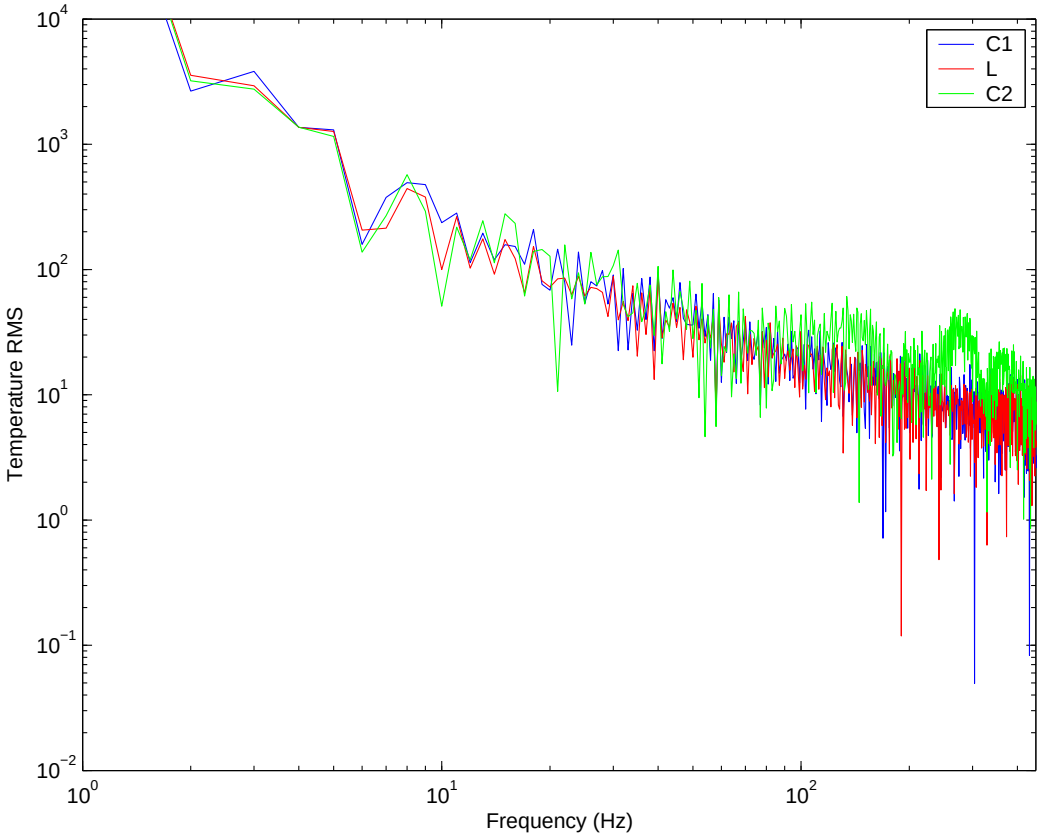

Figure 6.8 The spectrum of WVR observation in Figure 6.7.

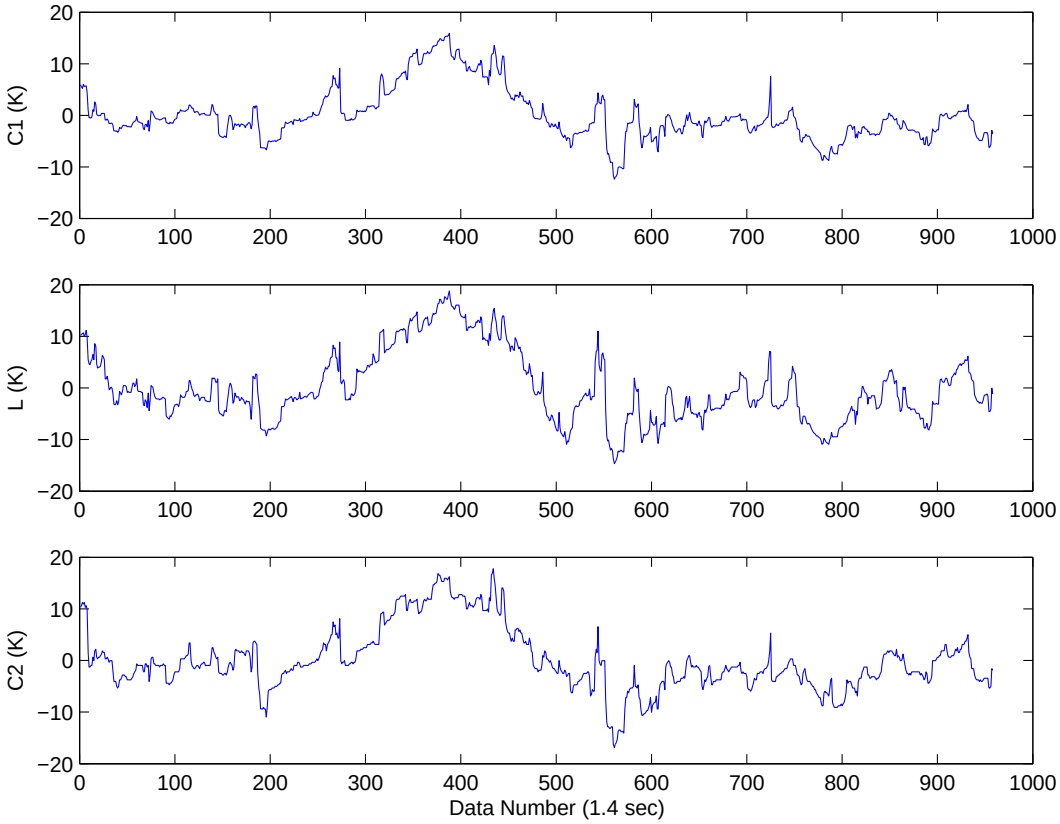

Figure 6.9 WVR observation taken under a bad weather condition.

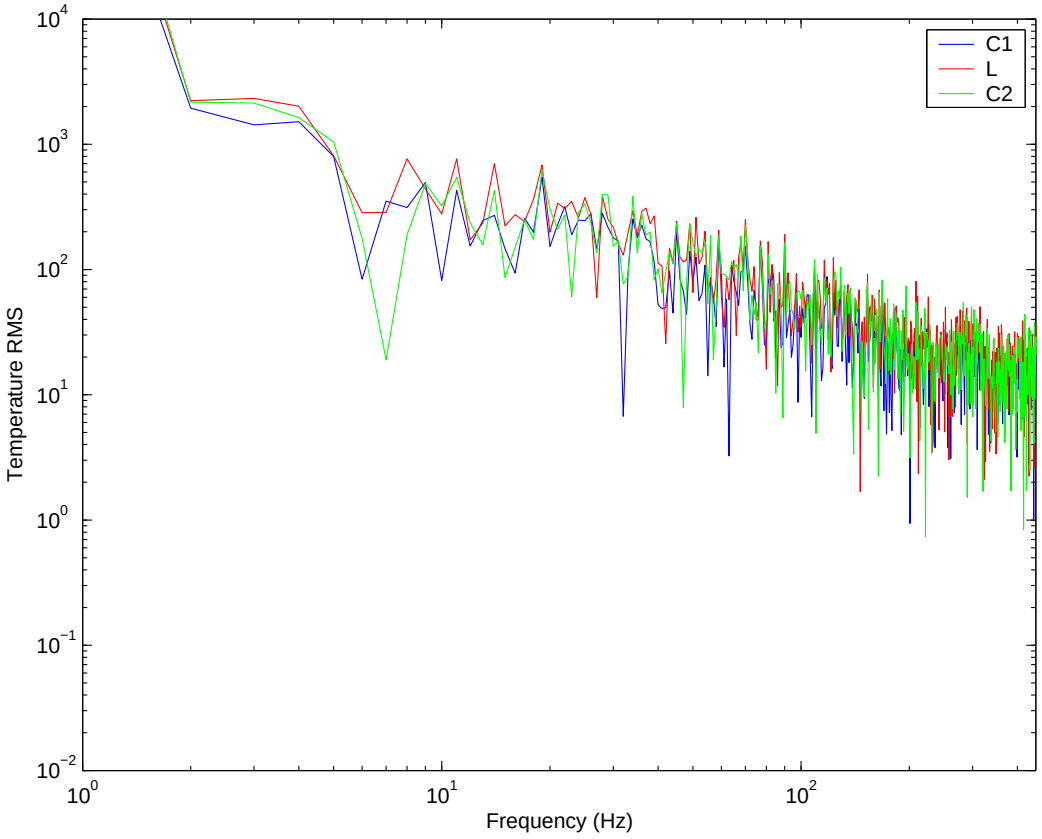

Figure 6.10 The spectrum of WVR observation in Figure 6.9.

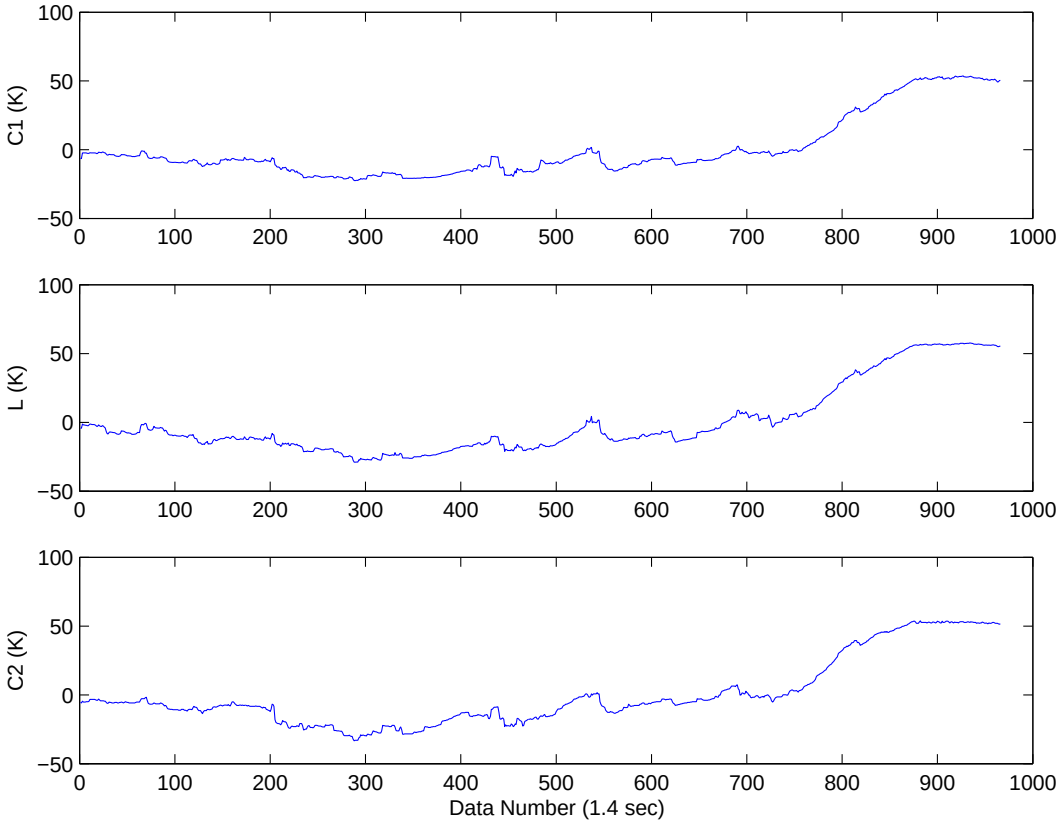

Figure 6.11 Additional WVR observation taken under a bad weather condition.

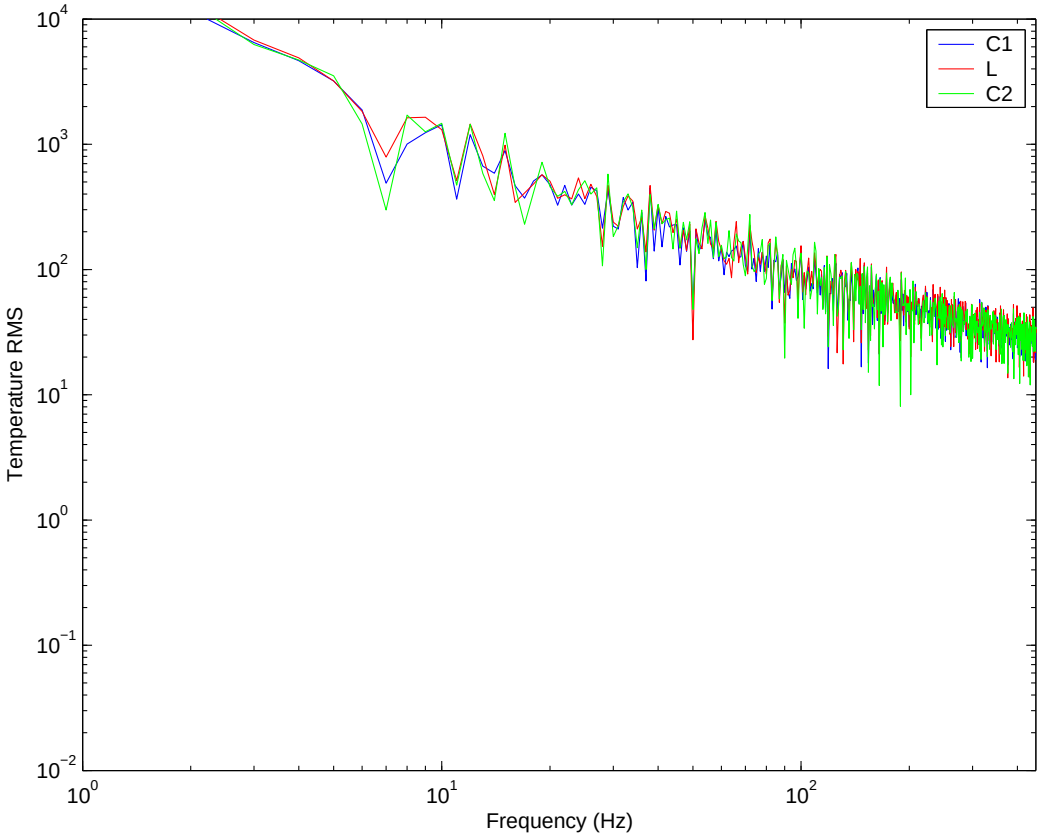

Figure 6.12 The spectrum of WVR observation in Figure 6.11.

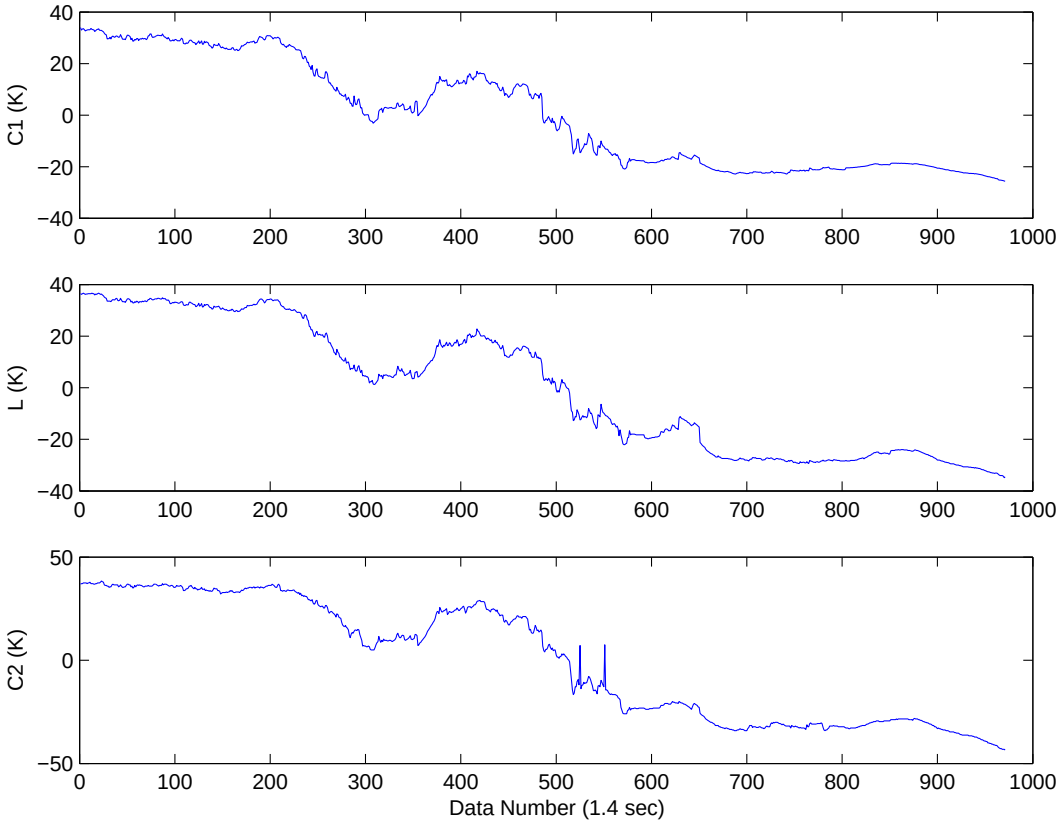

Figure 6.13 Additional WVR observation taken under a bad weather condition.

From those spectra above, the sky temperature fluctuation fits the turbulence model (Frisch 1995, p.89). The sky temperature fluctuation is undoubtedly turbulence. However, instrumental 1/f noise, including gain and system temperature, are like turbulence noise as well. The instrumental noise should be relatively stable within 12 minutes. If we assume the contributions of the instrumental noise is the same no matter what the weather condition is, we can roughly know the magnitude of the instrumental noise from good weather data. Therefore, we can conclude that the atmosphere contributes most of variations in the WVR data. This is an important estimate for the WVR project. We need to clarify the noise sources so we can further investigate the system performance and determine the major effect to the WVR data is from the atmosphere or the instrument itself.

We compare the data from the two WVRs to see if their data are correlated. Figure 6.21 and 6.22 are two typical tracks at the tests. The periodic drops in the data set were due to the reading and writing by the single board computers (SBCs) in the WVRs. The WVRs are very sensitive so they can pick up 1 μV power drops. Figure 6.21 and 6.22 were taken at the same day under very stable weather. In Figure 6.21, the sky temperatures of three channels show different trend, while in Figure 6.22, they show the similar

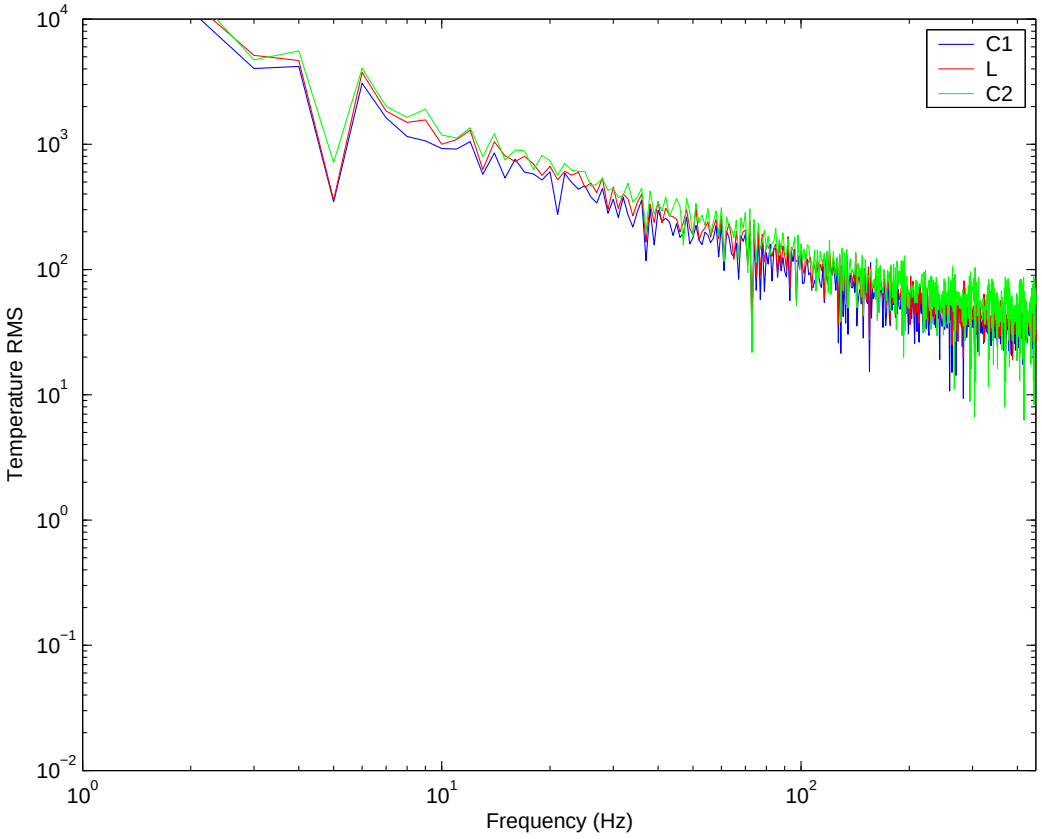

Figure 6.14 The spectrum of WVR observation in Figure 6.13.

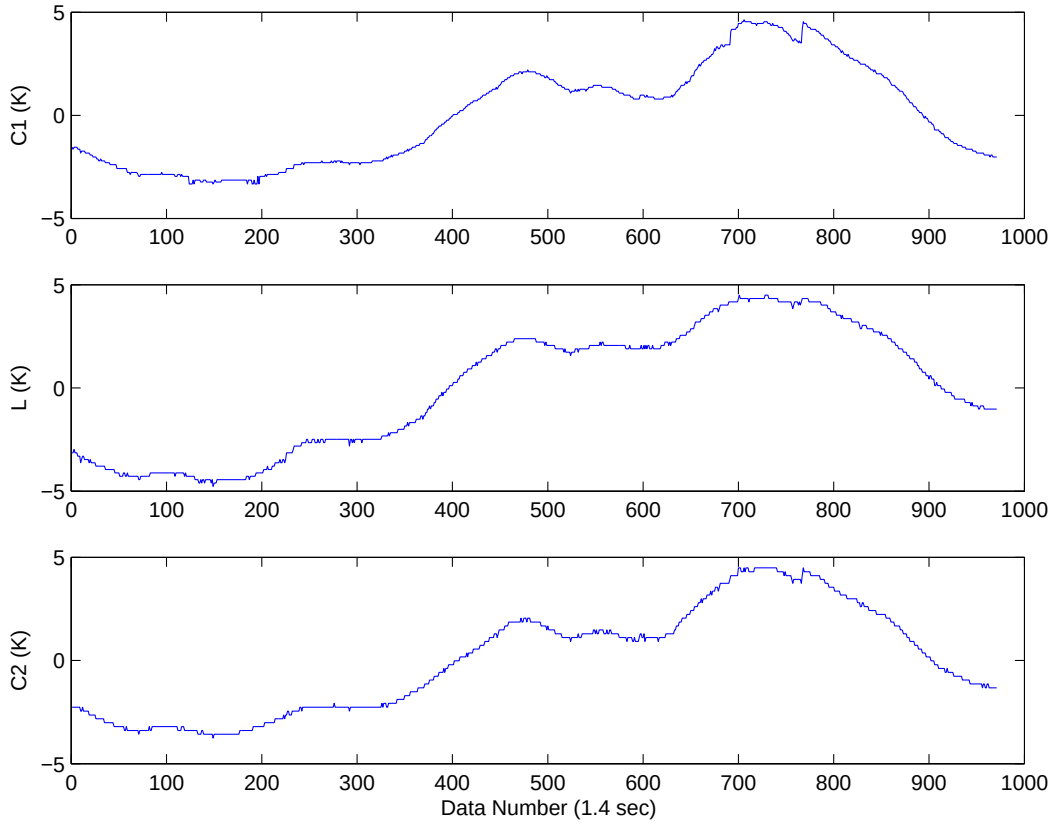

Figure 6.15 WVR observation under a good weather condition.

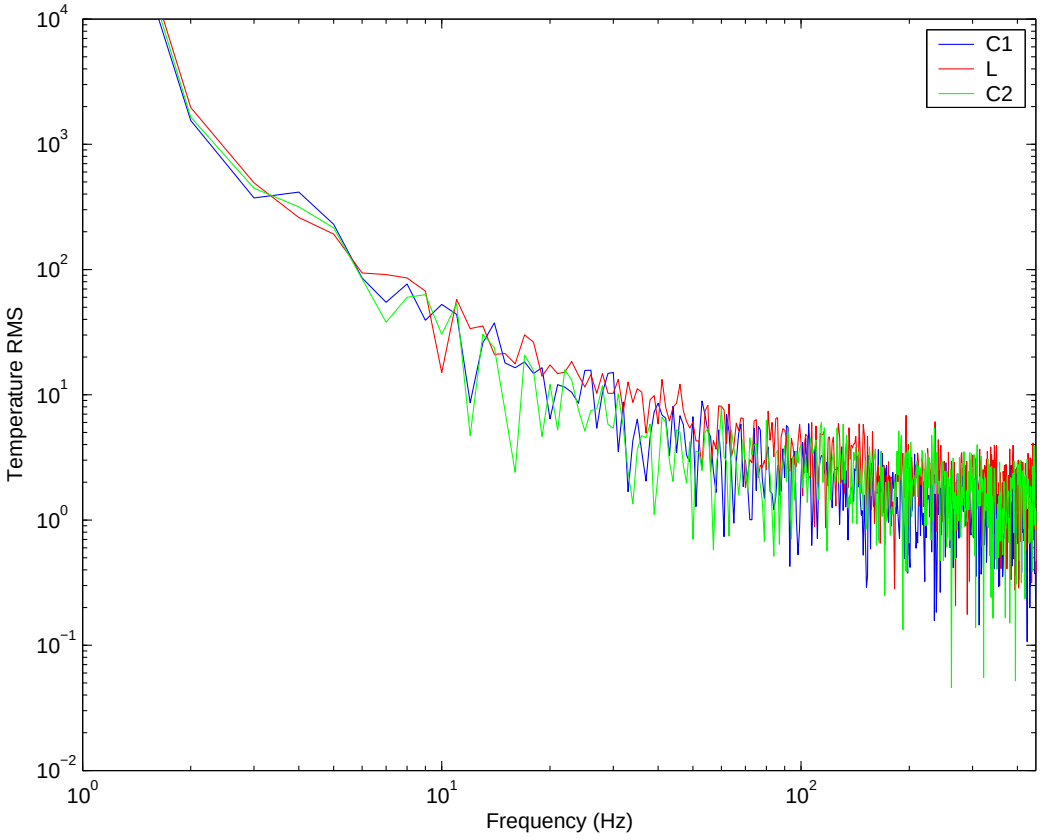

Figure 6.16 The spectrum of WVR observation in Figure 6.15.

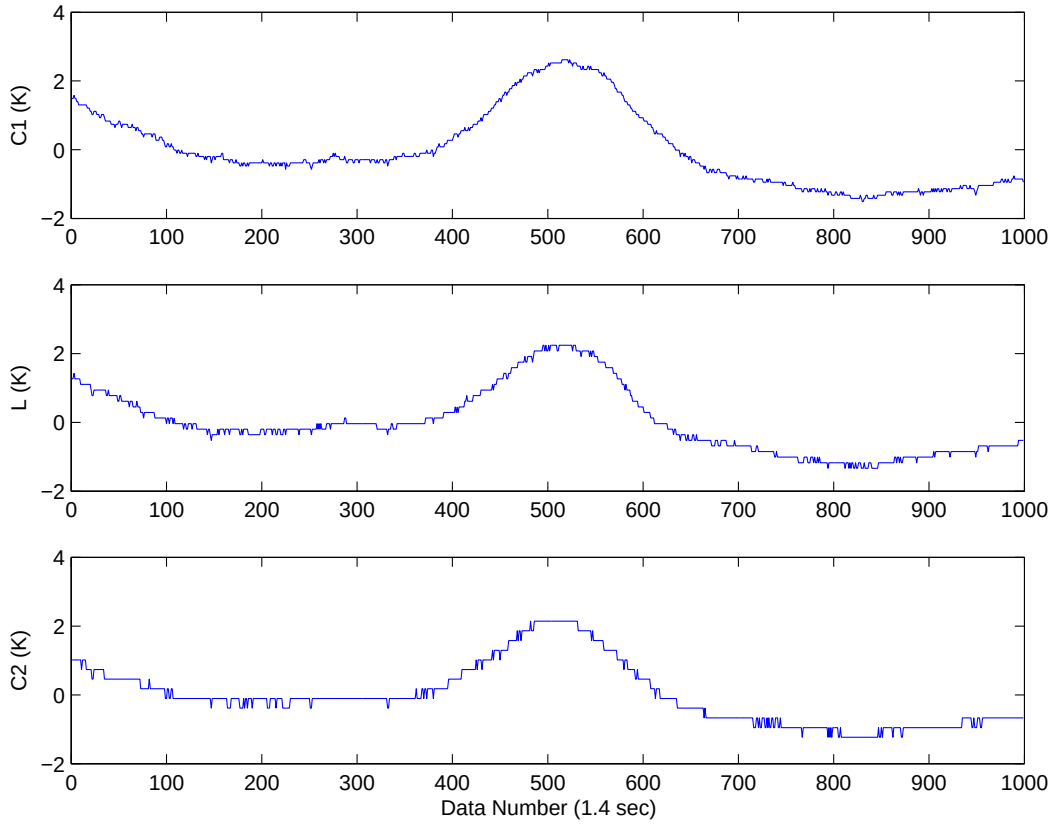

Figure 6.17 Additional WVR observation under a good weather condition.

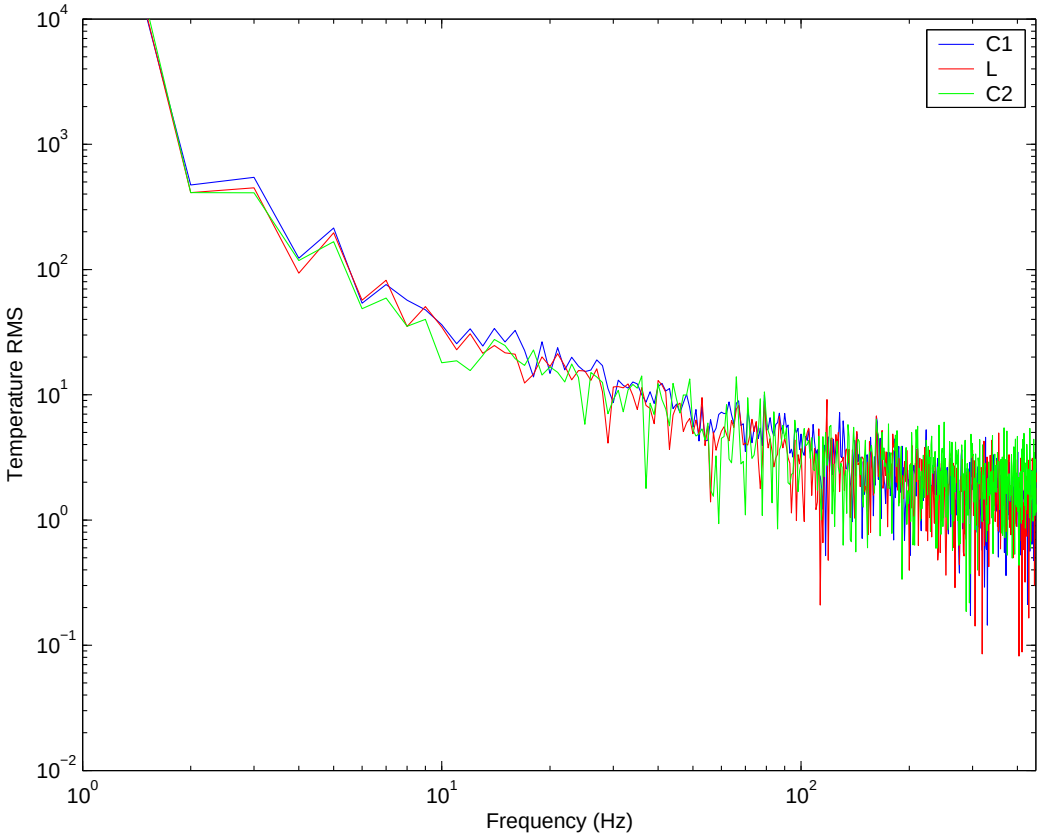

Figure 6.18 The spectrum of WVR observation in Figure 6.17.

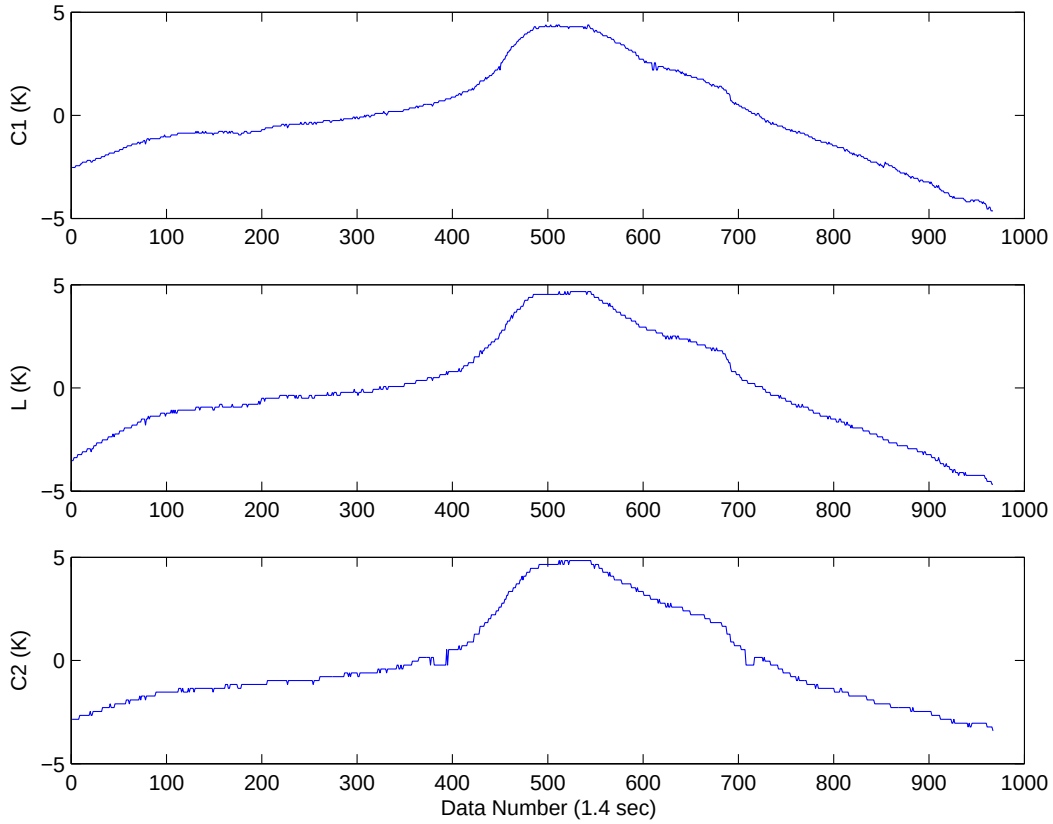

Figure 6.19 Additional WVR observation under a good weather condition.

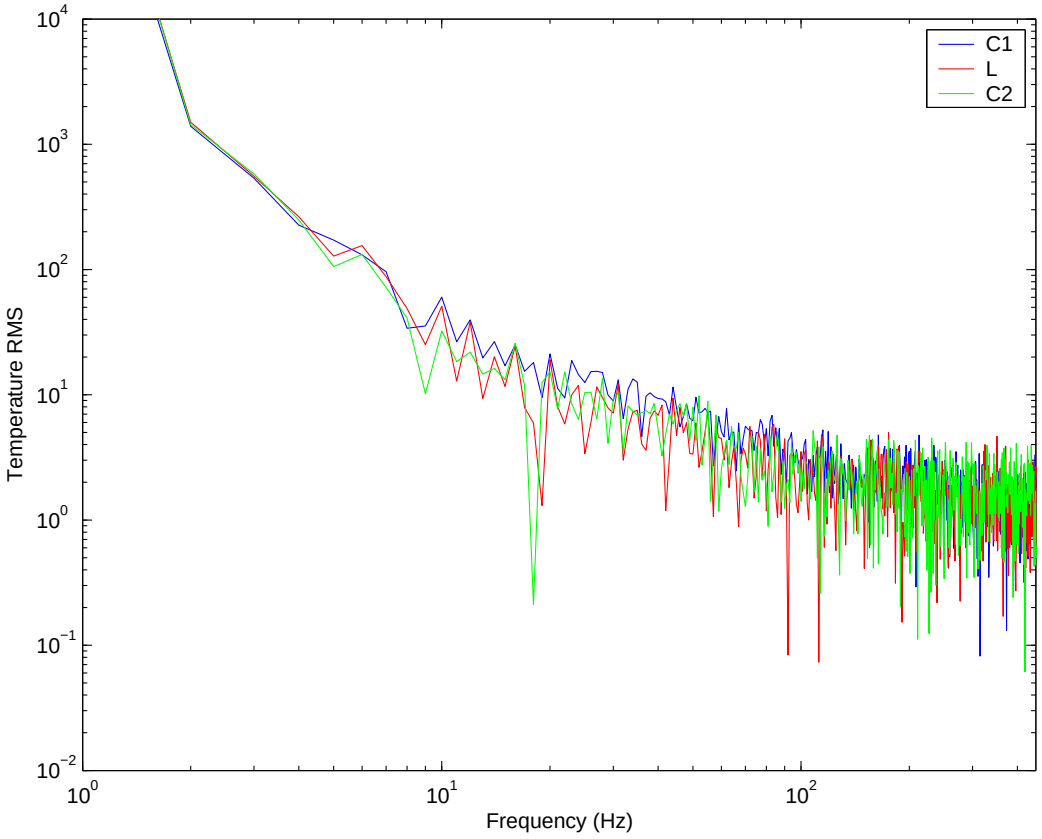

Figure 6.20 The spectrum of WVR observation in Figure 6.19.

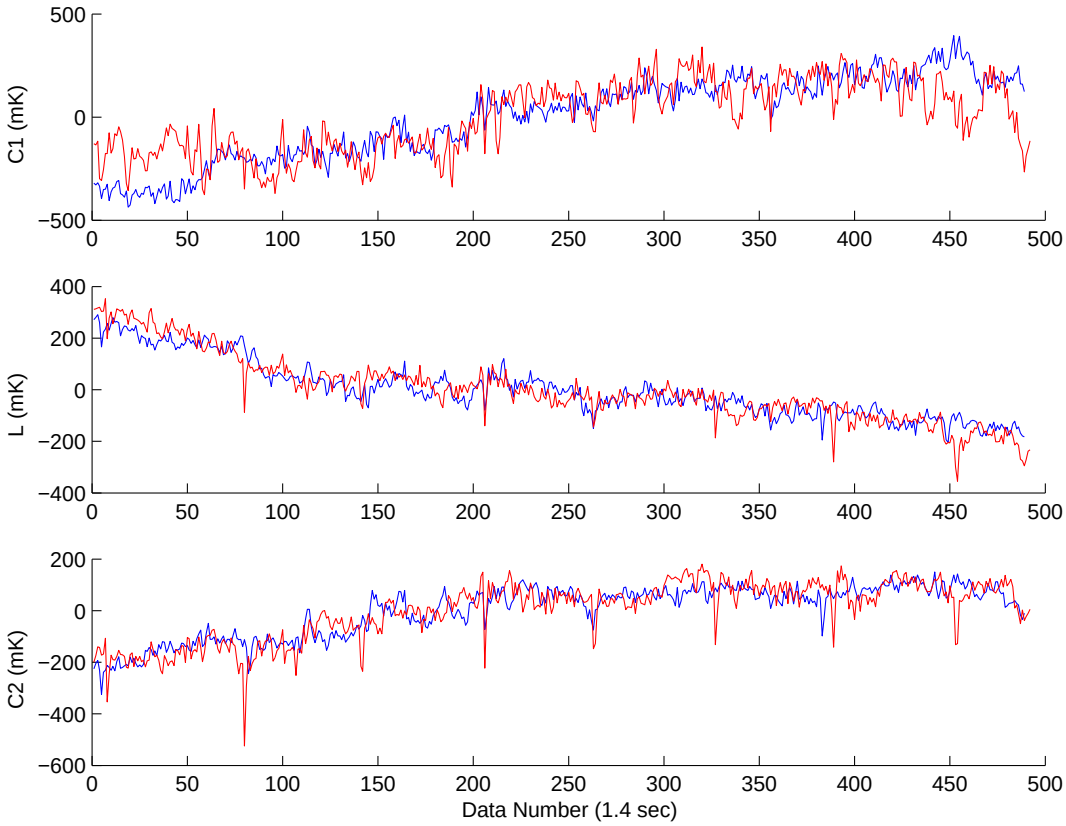

Figure 6.21 WVR data taken on Feb. 11th 2008. The weather was cloudy. Three channels show different trends in this 12 minute track. However, the two WVR data sets match at the three channels.

trend. The former may be reflect the water vapor emission. The two continuum channels, C1 and C2 have the same trend; only the line channel, L, is different from the others. In general, the three channel data of one WVR matched those of the other WVR. However, 10% of the time, they did not quite match. There were two possibilities when this happened. One is that the weather was very unstable and the other is that the weather was so stable that instrumental noise dominated the data when the WVR rms was less than 200 mK. Although we estimated the WVR sensitivity is about 30-50 mK in the laboratory, during the roof tests we only got 100-200 mK. If the sky temperature rms was lower than 100 mK, then we encountered difficulty to detect the water vapor signal.

The roof tests show the Illinois weather is unstable most of the time. In a 12 minute track, the sky temperature constantly changes on the scale of a few K. Moreover, wind affects the thermal regulation enormously. However, the calibration system can still properly calibrate three channel signals. Thus, we approximately determine the performance of our WVRs. To further test our WVRs with real time phase variation data, we proceed our WVR project at the CARMA site.

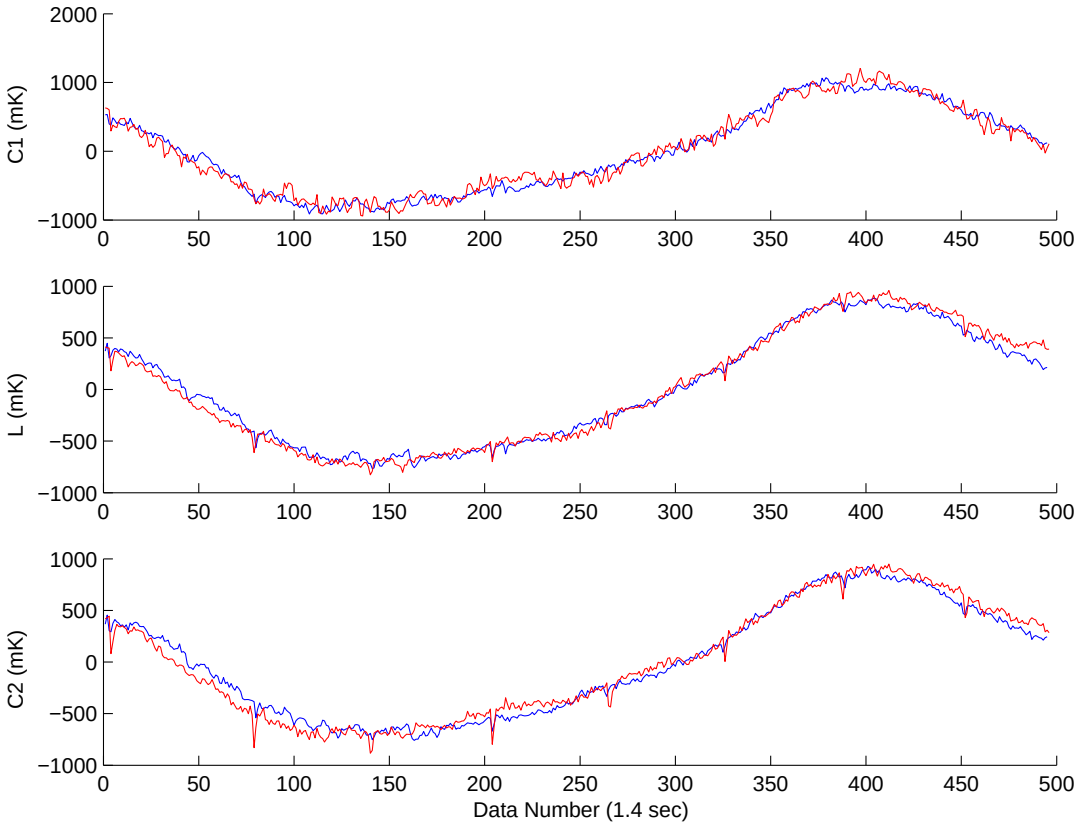

Figure 6.22 Another WVR data taken on Feb. 11th 2008 in the roof test. The weather was cloudy. Three channels show similar trends in this 12 minute track.

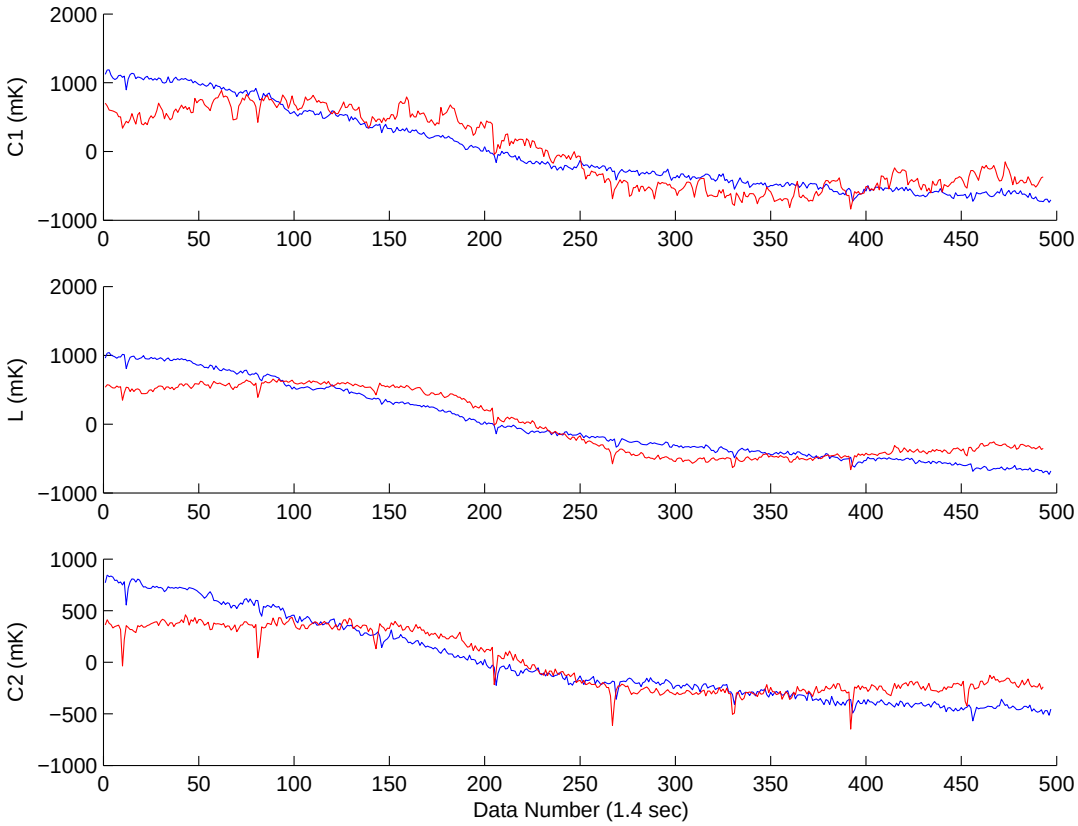

Figure 6.23 WVR observation on Feb. 18 2008 at the side-by-side tests.

6.3 CARMA Site Tests

In 2008 spring, we shipped the WVRs to the CARMA site for further testing of the water vapor vapor phase correction. The CARMA site is at Cedar Flat in California. The height of the site is about 7200 feet. The site is dry and the weather should be stable most of the time.

First we set up two WVRs in a side-by-side test near the CARMA antennas. The test was a sanity check on the WVRs to see if they reproduced the same results as the roof tests. Figure 6.23, 6.24 and 6.25 are the side-by-side test results. Unlike the roof tests in Illinois, the side-by-side tests showed that most of the time the trends of two WVR data did not match. Figure 6.23 was the typical case that two WVRs show slight similarity in their data. However, many tracks like Figure 6.24 and 6.25 occurred at the test. There seemed some sort of interference at the site. One WVR often showed strong sources in tracks as shown in Figure 6.25.

We continued to install the WVRs near the phase monitor dishes at the CARMA site. The phase monitor measured the phase rms for the CARMA observers to determine $\lambda = 1$ mm or 3 mm weather. The principle

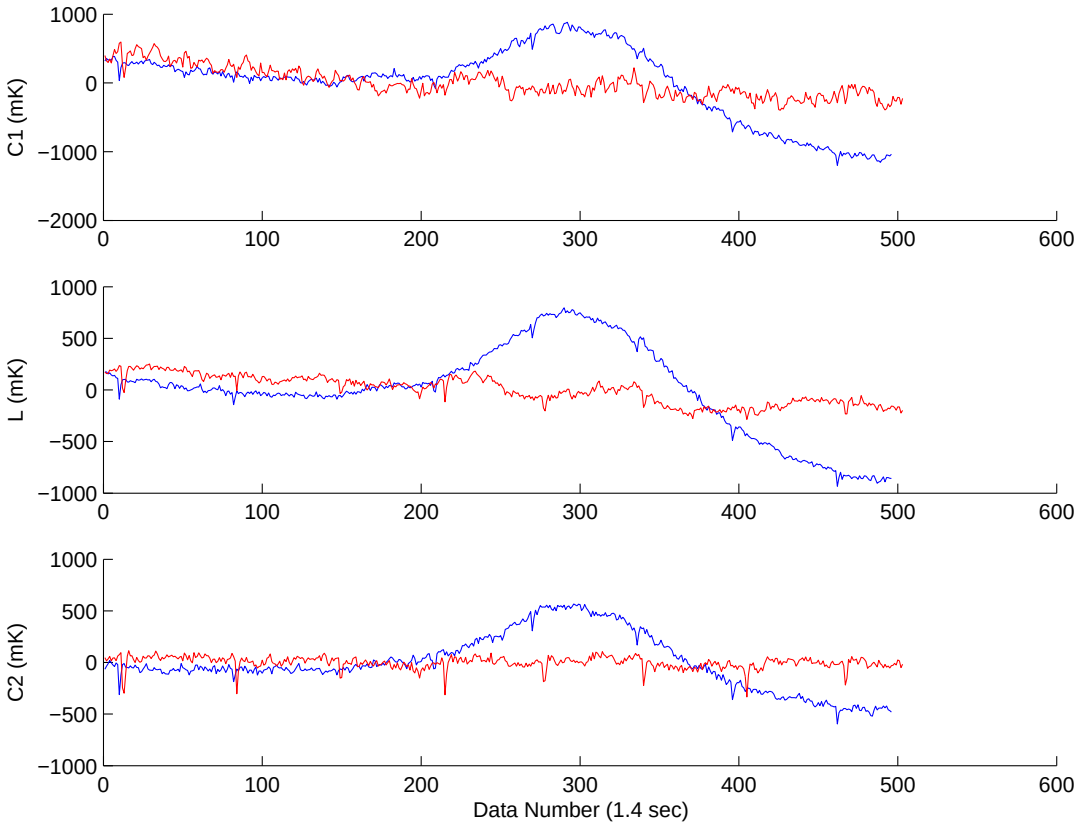

Figure 6.24 Additional WVR side-by-side observation at the site.

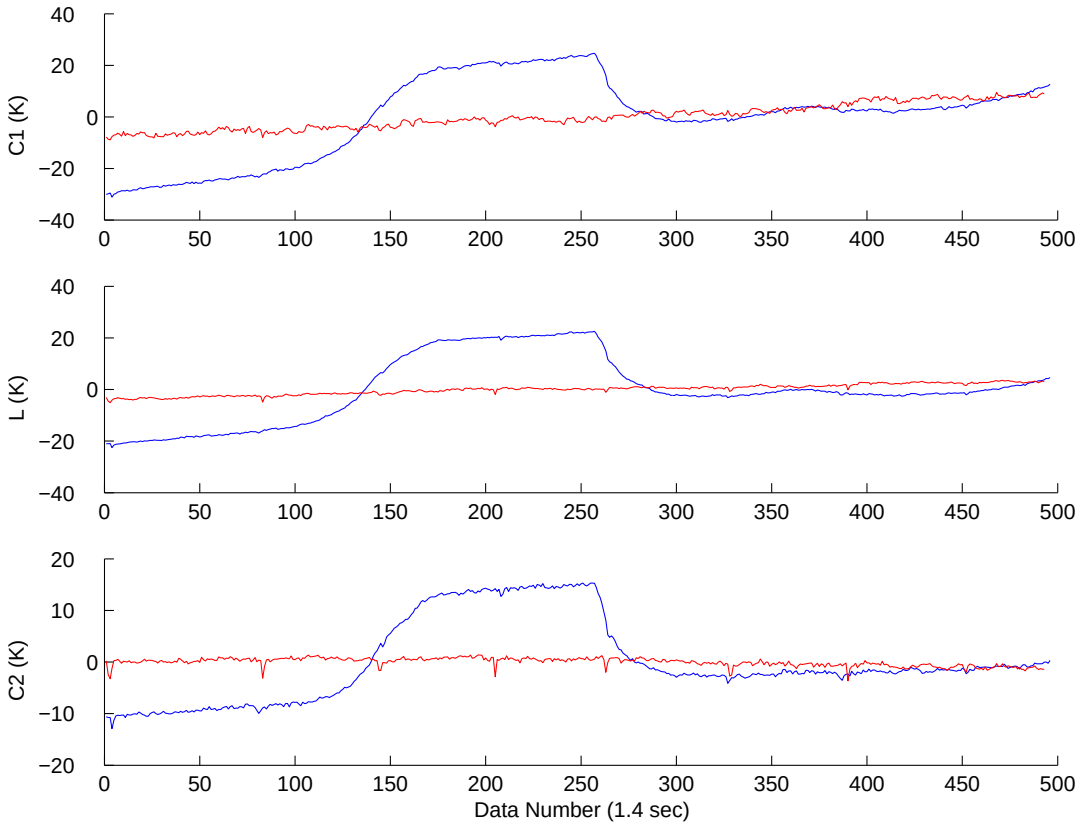

Figure 6.25 Additional WVR side-by-side observation at the site. The RF interference occurred on one WVR.

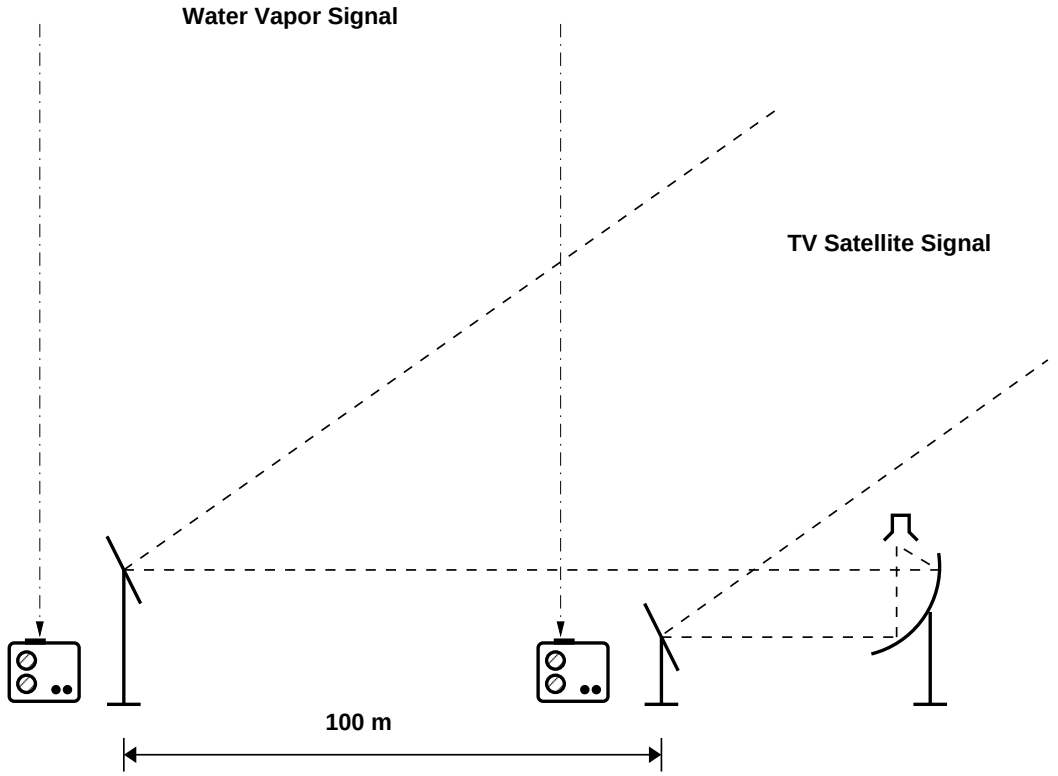

Figure 6.26 Site test setup: the two WVRs were installed near the phase monitor mirrors. The baseline was 100 m. The WVRs did not point to the TV satellite because the TV signal may cause problems to the WVRs.

of the phase monitor was to use TV satellite signal as astronomical signal to indicate the atmospheric phase fluctuation with two different paths as shown in Figure 6.26. Two phase monitor dishes were separated by 100 m. The resolution of the phase monitor was about 50 μm. Although we could not use the phase monitor to calibrate the absolute gains of the WVRs, we still can see the correlation by comparing the rms of the phase monitor data with the rms of the WVR data. Thus, we can quantify the correlation between the water vapor and phase fluctuation. Figure 6.27 and 6.28 show the WVRs sitting near the phase monitor dishes.

Figure 6.29 shows the comparison of the phase monitor and the WVR data. The correlation is clear. However, the scale factor of the 22 GHz water vapor line varies from 6 to 20 as other WVR projects suggest (Marvel & Woody 1998; Chandler et al. 2004; Wiedner et al. 2001). We discarded 60% of the tracks suffering from interference or showing abnormal phenomena when we reduced the data. The sensitivity of the WVRs at the roof tests is about 100-200 mK, while it is 30-50 mK in the laboratory. When the atmospheric rms is less than 1000 μm more than or 100 mK, the WVRs fail to accurately determine the water vapor emission.

Figure 6.27 A WVR was set up near a phase monitor dish.

Figure 6.28 The other WVR was set up near the other phase monitor dish.

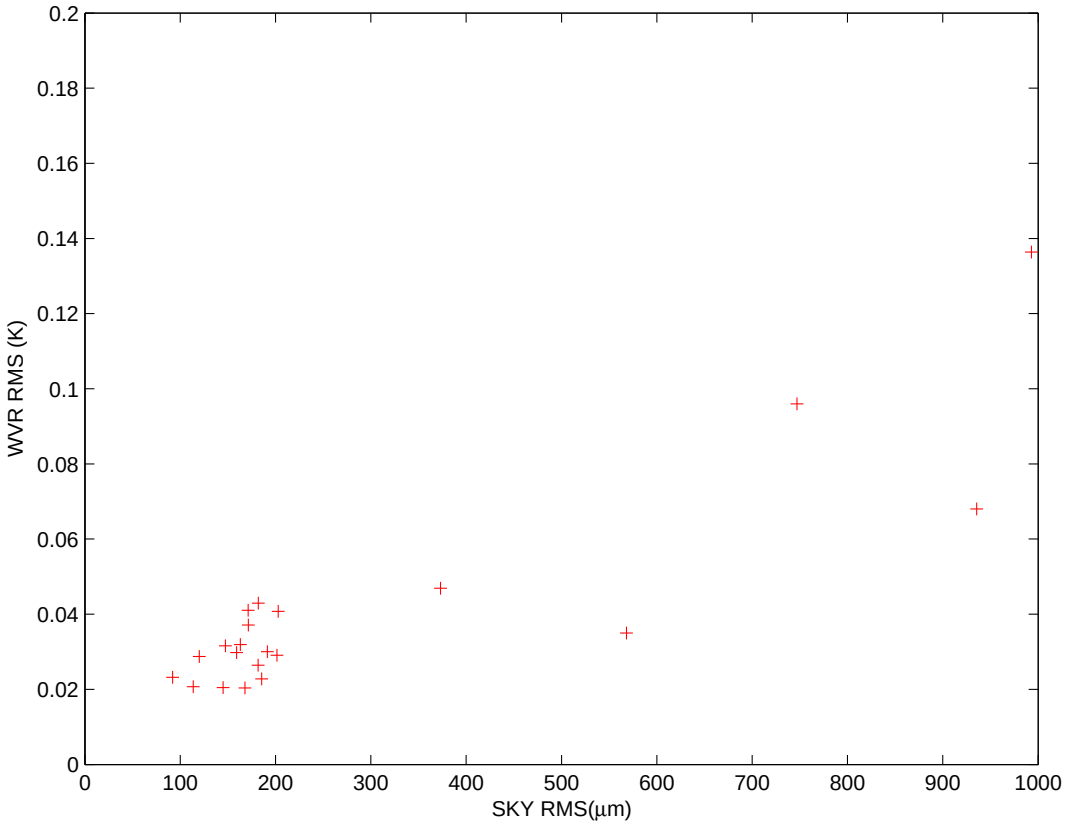

Figure 6.29 Phase monitor data rms v.s. WVR data rms.

6.4 Discussion

6.4.1 Background Emission

At the roof and site tests, we discovered that the sky temperature varied rapidly and greatly. This severely challenged the dynamical range of the WVRs. In normal cases, the sky temperature could change 2-5 K in 12 minutes, which suggested that clouds, and hot or cold air in the atmosphere played a critical role in water vapor detection. They were bright background emitters. Thus, based on our tests, it is certain that monitoring the continuum band at 220-250 GHz by WVRs is unlikely to convert the WVR data to path delays. The background emission may dominate the sky temperature at that band. Despite that the sky temperature varied on a large scale, the phase monitor data did not show such a large amount of phase change at the site tests. Therefore, the continuum temperature is not sufficient to derive path delays.

Initially we wanted to minimize such background emission effects by subtracting the continuum (C1+C2)/2 from the L channel. With the rapid change of the sky temperature, we doubted that the subtraction could effectively distinguish the water vapor line from the background emission due to the limited dynamical range, which may distort the water vapor line feature already. During data reduction, we had to use low order polynomial fitting to subtract the background emission. We assumed that the low frequency WVR data fluctuation was mainly the background emission, which did not affect the path delays, while the high order fluctuations of the WVR data is due to water vapor emission. However, the background emission fluctuation is enormous so that the high order fluctuation, which is water vapor emission, is severely interfered.

6.4.2 RF Interference

The radio interference seemed more serous at the site, which may be due to the nearby 1 and 3 mm receivers on the CARMA antennas that produced radio frequency leakage to the WVRs. One of the channels sometimes showed a huge spike when others did not. The beam size of the WVRs was large (49°) and they may also pick up signals from those other than the sky.

At the roof test, the two WVRs show common trends most of time, while at the site test, they occurred considerably less. The reason is still unknown and it may need further investigation in the future.

6.4.3 Detection Efficiency

Beside the WVRs and the atmosphere, we have demonstrated the impact of the water vapor detection efficiency on the conversion of water vapor line emission to path delay. In addition to building WVRs, we may need to develop instruments that can determine water vapor cloud height and size. At this point,

we do not know if it is possible to have such devices or technology. However, if water vapor turbulence indeed frequently consists of scattered clouds in various sizes, it is critical to obtain the water vapor cloud information.

6.4.4 Instrument or the Atmosphere?

The question about the reliability issue of the water vapor phase correction is that: is it due to simply the turbulent atmosphere or the poor performance of instruments? Or even both? To answer this question, a systematic approach to uncover any potential problem is a necessity. Based on our WVR tests, we conclude that the volatile atmosphere and noisy background overwhelm the WVR design that is solely based on a fairly quiescent model. The water vapor detection efficiency, the sky background emission, the physical temperature variation, the RF interference and severe weather are not fully considered or are underestimated when designing WVRs. We have exploited our WVRs to uncover these problems with extensive testing.

To actually detect the water vapor lines and convert to path delays, the system requirement of WVRs are certainly higher than formerly expected. New WVRs need to significantly improve their dynamic range, avoid RF interference, stabilize temperature, and compensate for the non-perfect detection efficiency. The trade-off between the observational efficiency of an interferometer and the effort of developing such high quality WVRs becomes unclear.

6.4.5 Future Work

We have carried out the wall test to determine the sensitivity of the WVRs. Then, we test our WVRs on the roof to examine their performance under real weather conditions. Finally, our tests were extended to the CARMA site and further investigated the correlation of the atmospheric phase variation and the 22 GHz water vapor line. We realize that the sky temperature fluctuation can be enormous even at a dry site. More considerations need to be taken and further refinement of the WVR system should be done to increase the WVR sensitivity and dynamical range.

Diode Detector

Because the magnitude of the sky temperature fluctuation is beyond our expectation, we need to further consider the nonlinearity of the WVRs. The bottle neck of the nonlinearity of radiometers are diode detectors. To increase the dynamical range, the diode detector model needs to be established so we can compensate the nonlinearity to reconstruct the water vapor emission.

Beam Size

The beam size of the WVRs is about 49°, which is extremely large and easily pick up unwanted signal. To downsize the beam, we can put a large mirror in front of the antenna horn window of the WVR. The alignment of the mirror can be done by a base and mount structure that supports both the mirror and the WVR.

Thermal Regulation System

Although the WVRs can detect the sky temperature fluctuation, the relationship between the frontend temperature and the WVR data is still uncertain. To minimize the physical temperature effect, a better thermal regulation system still can be useful in the WVR system. We suggest to use more stages to insulate the frontend and regulate the heat flows from inner parts to outers. To prevent the wind changing the thermal conductivity, one needs to design a device to regulate the air flow over the heat sink on the WVR box.

Chapter 7

Conclusions

Rotational transitions of molecules are mostly in the radio frequency region, which is an observable window for ground-based telescopes. Astronomers have used such transitions to detect over 127 molecules in the interstellar medium (ISM). While the rotational transitions reveal not only the molecular species but also their physical conditions, understanding rotational spectroscopy becomes a necessity for radio astronomers. Through molecular detections, the physical information about many astronomical objects can be unlocked. For example, CO, the second most abundant molecule in space, has been used as a tracer to explore galactic and extragalactic star forming regions. The bright molecular transitions can be analyzed to image the complex dynamics of molecular clouds in three dimensions, including velocity space. In this thesis, we have introduced basic rotational spectroscopy and addressed the importance of the electric dipole moment and the angular moments of inertia. The former governs the Einstein A coefficient of a spontaneous emission, which corresponds to a transition rate or line intensity. The latter decides spectral patterns and frequencies, which is critical to identify molecular species.

While simple molecules, like CO, can be powerful probes to examine astronomical objects, numerous molecules in the ISM generate very different types of chemistry. The ISM contains a variety of physical environments for molecules. Molecular clouds can be cold or hot, dense or diffuse. The most molecule abundant regions in the ISM are hot molecular cores. Many molecules, including organic molecules, have been detected in hot molecular cores. Such hot cores are high-mass star forming region at the early stage. They have energetic sources from shocks, gravitational collapses and protostars. As stars form, different time scales provide temperature and density differentiation for molecular formation. The chemical evolution of hot cores is still uncertain but large molecule observations have already uncovered interesting chemical phenomena. First, with simple gas phase models, observed large molecules seem to be much more abundant than predicted. Second, toward some hot core regions, oxygen and nitrogen chemical differentiation appears considerably. Third, if organic molecules can be formed in hot cores, what about the biological molecules or even the origin of life? The answers may be in the time-scales of the hot core physical and chemical conditions. Grain surface reactions have been suggested to enhance the abundances of large molecules. With proper

timing of temperature, gas phase molecules may form mantles on dust grains and further chemically react to generate new large molecules. Finally they evaporate from the surfaces by high energy photons from protostars or increased temperature. Thus, high-mass hot cores become large molecule abundant. The O/N chemical differentiation may be due to the the ages of hot cores and the initial chemical conditions. However, to date, the hot core chemical models are still difficult to be confirmed and remain uncertain.

Acetic acid (CH_3COOH) is a biologically important molecule due to its association with glycine, which is the building block of protein. It is also of interest that CH_3COOH seems to be related to the O and N-rich chemistry. All CH_3COOH sources contain both large O and N-bearing species while some molecule-rich hot cores lack comparable CH_3COOH detections. To obtain more observations to constrain the models, we have conducted an acetic acid survey with the Combined Array for Research in Millimeter-wave Astronomy (CARMA) toward three sources, G19.61-0.23, IRAS 16293-2422 and NGC 1333 IRAS 4A. Moreover, we observed methyl formate ($HCOOCH_3$) and ethyl cyanide (CH_3CH_2CN) to determine oxygen/nitrogen chemical differentiation in these sources. In our survey, we have detected a new acetic acid (CH_3COOH) source, G19.61-0.23, which is a high-mass ultracompact H II region. Following Sgr B2(N-LMH), W51e2 and G34.3+0.15, G19.61-0.23 is the fourth high-mass hot core source of CH_3COOH to date. The column density of CH_3COOH is 2.4×10^{16} cm^{-2} and the abundance ratio of CH_3COOH to methyl formate ($HCOOCH_3$) is 8.5×10^{-2}; both are comparable to the other CH_3COOH sources. The CH_3COOH emission is extremely compact ($<2''$), which implies that the high resolution observation is critical to CH_3COOH detections. However, we did not detect CH_3COOH in either IRAS 16293-2422 or NGC 1333 IRAS 4A. While G19.61-0.23 shows rich large O and N-bearing molecules, we did not detect large N-bearing molecules in IRAS 16293-2422 and NGC 1333 IRAS 4A. Thus, the O/N chemical differentiation is consistent with the detections. The rotational temperatures of IRAS 16293-2422 or NGC 1333 IRAS 4A are also considerably low, 80 and 36 K, respectively. If the O/N chemical differentiation reflects the time-scales of hot cores, IRAS 16293-2422 or NGC 1333 IRAS 4A may be still at the very early stage and their N-bearing molecules just start forming. In future acetic acid surveys, high resolution of interferometers and the detections of large O/N-bearing molecules are necessary to discover new acetic acid sources.

CARMA is a merger of the Berkeley-Illinois-Maryland Association (BIMA) array and the Owens Valley Radio Observatory (OVRO) millimeter-wavelength array. It is a newly upgraded ground-based radio interferometer, which can be used to explore various astronomical objects, such as star forming regions, molecular clouds and galaxies. However, for ground-based interferometers, the atmosphere has a great impact on observational quality. With a turbulent atmosphere, CARMA cannot efficiently produce high quality data for competitive scientific goals.

Atmospheric turbulence causes the most amplitude and phase variation of interferometric data. The phase variation, which is also known as path delay variation, is the most critical. To suppress the variations and increase the efficiency, many correction or calibration schemes have been used in interferometric observations. Observing flux and gain calibrators along with scientific sources is one of common methods to minimize the atmospheric effect. However, the improvement is still limited.

Water vapor is the main component that causes the path delay variation. Thus, monitoring tropospheric water vapor along the lines of sight of antennas with radiometers may create a better phase correction technique for radio interferometers. However, many previous water vapor radiometer projects fail to give satisfactory results for phase correction and the water vapor phase correction technique is simply unreliable to date. The reasons why it is less useful are still unclear, so we decided to systematically re-examine this phase correction technique for CARMA and attempt to locate the problems. In the beginning of the CARMA water vapor radiometer (WVR) project, we have tested the OVRO water line monitors (WLMs) in a laboratory and concluded several tasks that can be improved by the latest technology, including the backend, calibration and thermal regulation systems. The investigation of the WVR phase correction can be proceeded by building new prototypes with careful performance evalution during the process. Then, we may finally implement such novel technique for CARMA and obtain much better observational efficiency.

In this thesis, we first demonstrated that how the phase variation rms affects the data quality by quantitatively comparing the coherence factor with the phase rms. The coherence factor is defined as the receiving power ratio of partially coherent waves to perfectly coherent waves. Based on the simulation, when the phase rms is higher than 50°, the received signal power is less than 50%. If the rms is 75°, the received power is only 10%. This result highlights the importance of phase correction and the potential of water vapor radiometers.

Second, we used the MIRIAD `ATM` code to simulate the atmospheric emission under various CARMA site condition, 2-5 mm PWV (precipitable water vapor) at 50% of the time. While the 183 GHz water vapor line saturates and its wings can only be used to indicate path delays with a complicated model, we discovered that the 22 GHz line is more suitable at the CARMA site. The atmospheric emission simulation shows that a scale factor can simply convert the water vapor emission at 22 GHz to the path delays, which has been suggested and used by many other WVR projects. Therefore, we decided to build 22 GHz water vapor radiometers to further investigate the WVR phase correction.

Beside building the WVR prototypes, we also evaluate the impact of finite-size water vapor clouds on the 22 GHz scale factor. We have conducted two dimensional simulations to calculate the difference between the water vapor emission and the antenna temperature in the near and far-field regions. The deviation,

which is called the detection efficiency in this thesis, is defined as the ratio of the antenna temperature to the corresponding water vapor brightness temperature. The simulations show that the detection efficiency is generally less than 100% due to the finite water vapor cloud sizes. Therefore, the scale factor is usually higher than predicted. In addition, the difference between the water vapor column and the antenna beam pattern may sometimes cause a negative scale factor, which has been observed by other WVR projects.

While we design our WVR prototypes, the requirements of the WVR system need to be addressed first. The sensitivity of the WVRs are 10 and 30 mK at $\lambda = 1$ and 3 mm, where the scale factor is assumed to be 10. With an integration time of 0.5-20 seconds, an uncooled 22 GHz receiver with normally 1000-2000 K system temperature is adequate. While cryostat systems are costly, the uncooled receivers can let us afford to immensely improve the rest of the WVRs with the newest devices. The stability of the WVR system temperature and gain is one of the greatest challenges. Both are affected by the WVR physical temperature. We take extra precaution designing the thermal regulation system for the frontend, which is the most thermally sensitive. The fluctuated gain will be corrected by applying an ambient load as a calibrator to the WVR. Finally, the dynamical range will be extended to virtually 60 dB by adopting a new calibration scheme with adaptive digitizers.

We have built two WVR prototypes and examined their performance in a laboratory. The WVR mainly includes the frontend, backend, thermal regulation and calibration systems. The lab results showed that the calibration system indeed corrected the gain deviation and the sensitivity was measured to be 30-50 mK, depending on channels. The lower frequency channels had higher sensitivity. The wall test confirmed that the two WVRs monitored an external source consistently. The backend system and control computers also functioned properly. During the roof test on campus, the WVR continuously monitored the tropospheric water vapor for several months. A variety of weather conditions revealed that the thermal regulation system could not stabilize the frontend temperature when the outside temperature changed too fast. The insulation and heater could only suppress the temperature variation on shorter time-scales, a few minutes to tens of minutes. Thus, we set the calibration cycle, which is also the data track length, as 12-15 minutes. The roof test data also showed consistent results on the three channels of the WVRs. As the weather was unstable and cloudy, the channel data showed irregular and sharp patterns. When the weather became stable, the data showed smooth and consistent patterns. By assuming that the atmospheric turbulence contributed the most WVR data fluctuations, when the weather was extremely stable, we determined the WVR sensitivity to be 100-200 mK. Compared with the lab test, the sensitivity was lower by a factor of 4. The extra noise may be caused by the test environments or failure to thermal regulate the frontend temperature. Nevertheless, we continued our tests at the CARMA site. The phase monitor at the CARMA site may give an answer to

the problem. Moreover, the phase monitor actually measured the atmospheric phase variations, which can be compared with the WVR observation, the site test was carried out for a few days in a winter. The phase rms versus WVR rms plot clearly showed a correlation between two data set. However, the scale factor of the 22 GHz water vapor line varied, 6-12, and when the the phase rms is lower than 200 μm or 40 mK, the correlation was weak, where may be due to the upper limit of the WVR sensitivity.

The WVR tests have shown that when the WVR physical temperatures are stable, the sensitivity is about 30-50 mK, which is reasonable compared with the site test. A lower sensitivity shown by the roof test may be due to the noisy environment. The roof and site tests both indicate that the background emission fluctuations are severe. The reason that we use a water vapor line instead of a continuum band is to avoid the background emission. However, if the fluctuations are too strong, with the limited dynamical range of the WVRs, the background emission still seriously affects the WVR data. The dynamical range depends on the system linearity and sensitivity. To extend the dynamical range, we need to precisely measure the nonlinearity of the diode detectors, which are the bottlenecks of the WVR dynamical range. The measurement can be used to establish numerical models of the detectors and then to correct the nonlinear distortion, Although the thermal regulation system can not stabilize the frontend temperature on a long time-scale, we have increased the calibration frequency to diminish this problem. However, we need to quantitatively address this issue. A further investigation and improvement may be useful to a better thermal regulation system for the WVRs. The beam size of the WVRs is 49°, which is too large to avoid most of RF (radio frequency) interference in an outdoor environment. To overcome this problem, we only need to install large mirrors in front of the WVRs. The large mirrors will form smaller beams for the WVRs.

In this thesis, we have confirmed a few answers for the WVR phase correction. First, the detection efficiency simulation indicates that the scale factor of the 22 GHz water vapor line can vary depending on the tropospheric water vapor condition. Second, the continuum band is not appropriate for the WVR due to the strong background emission. Third, WVRs using water vapor lines, either the 22 or 183 GHz lines, should commonly suffer from the effect of the background emission. Fourth, the WVRs are total power receivers that are sensitive to any thermal sources. Small beams and noise-free environments are required to measure tropospheric water vapor accurately. However, it may be a problem at a radio telescope site. At this point, WVRs with a high dynamical range and better thermal regulation are key for a feasible water vapor phase correction system.

References

Adams, W. S. 1941, ApJ, 93, 11

Balanis, C. A. 1996, "Antenna Theory Analysis and Design" (Wiley-Interscience), 2nd Editon

Bernstein, M. P., Sandford, S. A., & Allamandola, L. J. 1999, Sci. Am., 281, 42

Blake, G. A., Sutton, E. C., Masson, C. R., & Phillips, T. G. 1987, ApJ, 315, 621

Blake, G. A., Sandell, G., van Dishoeck, E. F., Groesbeck, T. D., Mundy, L. G., & Aspin, C. 1995, ApJ, 441, 689

Bottinelli, S., Ceccarelli, C, Neri, R., Williams, J. P., Caux, E., Cazaux, S., Lefloch, B., Maret, S., & Tielens, A. G. G. M. 2004a, ApJ, 617, L69

Bottinelli, S., Ceccarelli, C., Williams, J. P., Castets, A., Caux, E. Cazaux, S., Maret, S., Parise, B., & Tielens, A. G. G. M. 2004b, ApJ, 615, 354

Bottinelli, S., Ceccarelli, C., Williams, J. P. & Lefloch, B. 2007, A&A, 463, 610B

Bremer, M, Guilloteau, S., & Lucas R. 1995, ESO-IRAM-NFRA-Onsala Workshop on Science with Large Millietre Arrays

Burke, B. F, & Graham-Smith, F. 2002, "An Introduction to Radio Astronomy" (Cambridge Univ. Press), 2nd Edition

Cazaux, S., Tielens, A. G. G. M., Ceccarelli, C., Castets, A., & Wakelam, V. 2003, ApJ, 593, L51

Ceccarelli, C., Casterts, A., Caux, E., Hollenbach, D., Loinard, L., Molinari, S., & Tielens, A. G. G. M. 2000a, A&A, 355, 1129

Ceccarelli, C., Loinard, L., Casterts, A., Faure, A., & Lefloch, B. 2000b, A&A, 362, 1122

Ceccarelli, C., Loinard, L., Casterts, A., Tielens, A. G. G. M., & Caux, E. 2000, A&A, 362, 1122

Chandler, C. J., Brisken, W. F., Bulter, B. J., & Hayward, R. H. 2004, WVLA Memo, 73

Chandler, C. J., Brogan, C. L., Shirley, Y. L., & Loinard, L. 2005, ApJ, 632, 317

Cheung, A. C., Rank, D. M., Townes, C. H., Thornton, D. D., & Welch, W. J. 1968, Phys. Rev. Lett., 21, 1701

Cheung, A. C., Rank, D. M., Townes, C. H., Thornton, D. D., & Welch, W. J. 1969, Nature, 221, 626

Di Francesco, J., Myers, P. C., Wilner, D. J., Ohashi, N., & Mardones, D. 2001, ApJ, 562, 770

Dicke, R. H., Peebles, P. J. E., Roll, P. G., & Wilkinson, D. T. 1965, ApJ, 142, 414

Friedel, D. N., Snyder, L. E., Turner, B. E., & Remijan A. 2004, ApJ, 600, 234

Friedel, D. N., Snyder, L. E., Remijan, A. J., & Turner, B. E. 2005, ApJ, 632, L95

Friedel, D. N. & Snyder L. E. 2008, ApJ, 672, 962

Frisch, U. 1995, "Turbulence: the legacy of A. N. Kolmogorov" (Cambridge Univ. Press)

Furuya, R. S., Cesaroni, R., Takahashi, S. Momose, M. Testi, L. Shinnaga, H., & Codella, C. 2005, ApJ, 624, 827

Garay, G., Moran, J. M., Rodriguez, L. F., & Reid, M. J., 1998, ApJ, 492, 635

Garay, G., Reid, M. J., & Moran, J. M. 1985, ApJ, 289, 681

Garrod, R. T., & Herbst, E. 2006, A&A, 457, 927

Garrod, R. T., Widicus Weaver, S. L., & Herbst, E. 2008, ApJ, 682, 283

Gawronski, W. 2007, IEEE Trans. on Control Systems Technology vol. 15, 2, 276

Genzel, R., & Downes, D. 1977, A&AS, 30, 145

Goldsmith, P.F., & Langer, W. D., 1999, ApJ, 517, 209

Harris, A. I. 2000, BIMA Memo, 80

Hasegawa, T. I., Herbst, E., & Leung, C. M. 1992, ApJS, 82, 167

Hawkins, D. W., Woody, D. P., Wiitala, B., Fredsti J., & Rauch, K. P. 2004, Proc. SPIE, 5498, 567

Herbst, E. 1999, Millimeter-wave Astronomy: Molecular Chemistry & Physics in Space, Wall, W. F. et al. eds., Kluwer Acad. Pub.

Hewish, A., Bell, S. J., Pilkington, J. D. H., Scoot, P. F., & Collins, R. A. N Nature, 217, 709

Hills, R., & Richer, J. 2000, ALMA Memo, 303

Hofner, P., & Churchwell, E. 1996, A&AS, 120, 283

Hofner, P., Wyrowski, F., Walmsley, C. M., & Churchwell, E. 2000, ApJ, 536, 393

Hollis, J. M., Vogel, S. N., Snyder, L. E., Jewell, P. R., & Lovas, F. J. 2001, ApJ, 554, L81

Ilyushin, V., Kleiner, I., & Lovas, F. J. 2008, J. Phys. Chem. Ref. Data, 37, 1, 97

Kalenskii, S. V., Berulis, I. I., Val'tts, I. E., Dzura, A. M., Slysh, V. I., & Vasil'kov, V. I. 1994, AZh, 71, 51

Kroto, H. W. 1992, Molecular Rotation Spectra (Dover Pub.)

Kuan, Y.-J., Huang, H.-C., Charnley, S. B., Hirano, N., Takakuwa, S., Wilner, D. J., Liu, S.-Y., Ohashi, N., Bourke, T. L., Qi, C., & Zhang, Q. 2004, ApJ, 616, L27

Kurtz, S., Cesaroni, R., Churchwell, E., Hofner, P., & Walmsley, C. M. 2000, in Protostars and Planets IV, ed. V. Manning, A.P. Boss, & S. Russell (Tucson: Univ. Arizona Press), 299

Larionov, G. M., Val'tts, I. E., Winnberg, A., Johansson, L. E. B., Booth, R. S., & Golubev, V. V. 1999, A&AS, 139, 257

Li, Z. Y., & Shu, F. H. 1996, ApJ, 472, 211

Lin, C. C., & Swalen, J. D. 1959, Rev. of Mod. Phys., 31, 841

Loinard, L., Chandler, C. J., Rodriguez, L. F., D'Alessio, P., Brogan, C. L., Wilner, D. J., & Ho, P. T. P. 2007, ApJ, 670, 1353

Looney, L. W., Mundy, L. G., & Welch, W. J. 2000, ApJ, 529, 477

Lovas, F. J. 1982, Phys. Chem. Ref. Data, 11, 251

Lovas, F. J., & Snyder, L. E. 2008, CRC Handbook of Chemistry and Physics, Lide, D. R., ed. 88th Edition (Internet Version 2008), (CRC, Boca Raton, FL), Sect. 14, 6

Marvel, K. B., & Woody, D. P. 1998, Proc. SPIE 3357, 442

Matthews, H. E., Goss, W. M., Winnberg, A., & Habing, H. J. 1977, A&A, 61, 261

McKellar, A. 1940, PASP, 52, 187

McKellar, A. 1941, Publ. Dom. Astrophys. Obs. Victoria, 7, 251

Mehringer, D. M., & Snyder, L. E. 1996, ApJ, 471, 897

Mehringer, D. M., Snyder, L. E., Miao, Y., & Lovas, F. J. 1997, ApJ, 480, L71

Miao, Y., & Snyder, L. E. 1997, ApJ, 480, L67

Miao, Y., Mehringer, D. M., Kuan, Y.-J., & Snyder, L. E. 1995, ApJ, 445, L59

Oesterling, L. C., Sieghard, A., de Lucia, F. C., Sastry, K. V. L. N., & Herbst, E. 1999, ApJ, 521, 255

Pardo, J. R., Cernicharo, J., & Serabyn, E. 2001, IEEE Trans. on Antennas and Propagation, 49, 12, 1683

Penzias, A. A., & Wilson, R. W. 1965, ApJ, 142, 419

Reipurth, B., Rodriguez, F. L., Anglada, G., & Bally, J. 2002, ApJ, 124, 1045

Remijan, A., Liu, S.-Y., Snyder, L. E., Mehringer, D. M., & Kuan, Y. J. 2002, ApJ, 576, 264

Remijan, A., Snyder, L. E., Friedel, D. N., Liu, S.-Y., & Shah, R. Y. 2003, ApJ, 590, 314

Remijan, A., Shiao, Y.-S., Friedel, D. N., Meier, D. S., & Snyder, L. E. 2003, ApJ, 617, 384

Remijan, A. J., & Hollis, J. M. 2006, ApJ, 640, 840

Rodgers, S. D., & Charnley, S. B. 2001, ApJ, 546, 324

Rodgers, S. D., & Charnley, S. B. 2003, ApJ, 585, 355

Rohlfs, K., & Wilson, T. L. 2006, "Tools of Radio Astronomy" (Springer), 4th Edition

Sakurai, J. J., & Tuan, S. F. 1994, "Modern Quantum Mechanics" (Addison-Wesley Pub.)

Sault, R. J., Teuben, P. J., & Wright, M. C. H., in ASP conf. Ser. 77, Astronomical Data Analysis Software and Systems IV, ed. Shaw, R. A., Payne, H. E., & Hayes, J. J. E. 1995, (San Francisco: ASP), 433

Schöier, F. L., Jørgensen, J. K., van Dishoeck, E. F., & Blake, G. A. 2002, A&A, 617, 384

Shiao, Y.-S., Looney, L. W., Woody, D. P., Plambeck, R. L., & Bolatto, A. D. 2006, Millimeter and Sub millimeter Detectors and Instrumentation for Astronomy III, J. Zmuidzinas, W. S., Holland, S. W. & Duncan, W. D., eds., Proc. SPIE, 6275, 6275Y

Shiao, Y.-S., Looney, L. W., & Sutton, E. C. 2008, CARMA Memo 42

Shiao, Y.-S., & Looney, L. W. 2008, Millimeter and Submillimeter Detectors and Instrumentation for Astronomy IV, ed. Duncan, D. W., Holland, W. S., Withington, S., & Zmuidzinas, J., Proc. SPIE, 7020, 7020F

Shirley, Y. L., Evans, N. J., Young, K. E., Knez, C., & Jaffe, D. T. 2003, ApJS, 149, 375

Shu, F. H. 1977, ApJ, 214, 488

Shull, J. M., & Beckwith, S. 1982, ARA&A, 20, 163

Snyder, L. E., Buhl, D., Zuckerman, B., & Palmer, P. 1969, Phys. Rev. Lett. 22, 679

Snyder, L. E., Hollis, J. M., Lovas, F. J., & Ulich, B. L. 1976, ApJ, 209, 67

Snyder, L. E. 2006, PNAS, 103, 33

Staguhn, J., Harris, A. I., Plambeck, R. L., & Welch, W. J. 1998, BIMA Memo 67

Stirling, A., Richer, J., Hills, R., & Lock, A. 2005, ALMA Memo, 517, 2005

Sutton, E. C., Peng, R., Danchi, W. C., Jaminet, P. A., Sandell, G., & Russell, A. P. G. 1995, ApJS, 97, 455

Swings, P., & Rosenfeld, L. 1937, ApJ, 86, 483

Thompson, A. R., Moran, J. M., & Swenson, G. W. 2001, "Interferometry and Synthesis in Radio Astronomy" (Wiley-Interscience), 2nd Edition.

Townes, C. H., & Schawlow, A. L. 1955, "Microwave Spectroscopy" (New York:McGraw-Hill)

Waters, J. W. 1976, "Methods of experimental physics: Astrophysics Part B: Radio Telescopes" (Academic Press), 122

Weinreb, S., Barret, A. H., Meeks, M. L., & Henry, J. C. 1963, Nature, 200, 829

Welch, W. J. 1994, PASP, 59, 1

Wiedner, M. C., Hills, R. E., Carlstrom, J. E., & Lay, O. P. 2001, ApJ, 553, 1036

Widom, B. 2002 "Statistical Mechanics: A Concise Introduction for Chemists", Cambridge Univ. Press

Woody, D. P., Beasley, A. J., Bolatto, A. D., Carlstrom, J. E., Harris, A., Hawkins, D. W., Lamb, J., Looney, L., Mundy, L. G., Plambeck, R. L., Scoot, S., & Wright, M. 2004, Proc. SPIE, 5498, 30

Wootten A. 1989, ApJ, 337, 858

Wright, M. C. H. 1996, BIMA Memo, 44

Wright, M. C. H. 2000, BIMA Memo, 78

Wu, J., & Evans, N. J. 2003, ApJ, 592, L79

Zivanovic, S. S. 1992, Ph.D. thesis, Univ. of California, Berkeley, 54-07, B, 3784

Zivanovic, S. S., Forster, J. R., & Welch, W. J. 1995, Radio Science, 30, 4, 877

Vita